The Flux Divergence Method Applied to Nitrogen Emissions in The Netherlands

Thesis Report

Charlotte Anna Bryan

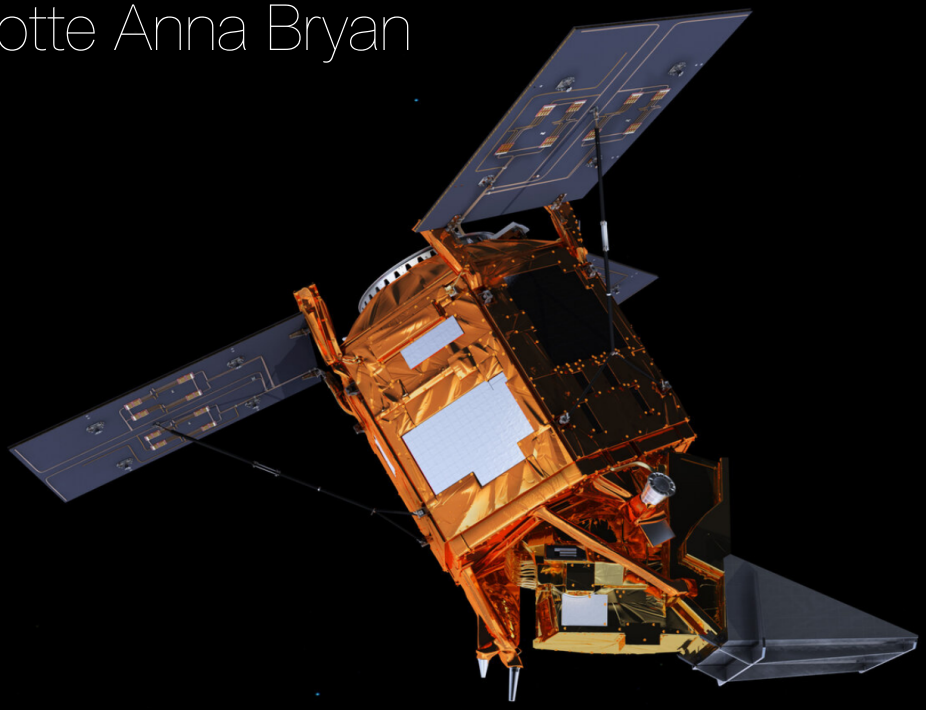

Koninklijk Nederlands Meteorologisch Instituut
Ministerie van Infrastructuur en Milieu

TU Delft Delft University of Technology

The Flux Divergence Method Applied to Nitrogen Emissions in The Netherlands

Thesis Report

by

Charlotte Anna Bryan

Daily Supervisor:	Arnold Heemink
Supervisor KNMI:	Henk Eskes
Comittee Member :	Neil Budko
Institution:	Koninklijk Nederlands Meteorologisch Instituut
Project Duration:	February, 2022 - December, 2022

Koninklijk Nederlands
Meteorologisch Instituut
Ministerie van Infrastructuur en Waterstaat

TU Delft Delft University of Technology

Acknowledgements

My gratitude goes out to all the people at the RDSW department of the KNMI. They were very welcoming during my stay at the KNMI, and made me feel a part of team. I greatly enjoyed the running workouts during the lunch breaks, and the vrijmibo's, discovering the city centre of Utrecht. Juliette, Benjamin, Victor, Serena, Yutao, Yang, Lev, Tim and everyone else, hope to see you all for a drink in the future! I would also like to thank Ronald and Jieying, for their help with with ammonia data, and Mirjam and Mengyao for their help with my presentation at the KNMI.

I am very grateful for everyone who helped me in writing this thesis. Juliette, Karen, Laura and Lucy, thank you for your thorough and thoughtful feedback. Daan, thank you for the multiple iterations you read for me, and for all the food you made me when I was too busy working (or just too lazy). And of course to my parents, who not only helped me by reading this entire thesis, but are also the main reason I was able to study at all.

Thank you to Neil for being a part of my thesis committee. Thank you to Arnold, for pointing me in the right direction to find a thesis subject I thoroughly enjoyed, helping me form this thesis to a thesis within applied mathematics, and being extremely flexible is planning last-minute green-light meetings. And finally, many thanks to Henk, for making me feel welcome at the KNMI, helping me get to know the fascinating world of remote sensing, and taking the time out of your busy schedule to help bring out the best in this thesis.

Charlotte Anna Bryan
Delft, December 2022

Abstract

In the Netherlands, reactive nitrogen emission (nitrogen oxides and ammonia) from anthropogenic activity puts pressure on vulnerable ecosystems. Effective policies to curb the emission of reactive nitrogen require reliable emission and deposition maps. The atmospheric vertical column density of these molecules can be measured using remote sensing instruments on satellites. In the case of nitrogen dioxide, this is done using TROPOMI, and in the case of ammonia, this is done using CrIS. The Flux-Divergence method is able to transform a vertical column density map to an emission map, allowing for the locating of sources and retrieval of emission rates.

The Flux-Divergence method assumes that all divergence in the flux of the trace gas is caused by its emission and its sinks. Finding an emission map using the Flux-Divergence method thus requires the computation of a flux-divergence map and the estimation of a sink term. The method was first introduced by Beirle et al., and implemented at the KNMI by Henk Eskes [1] [2]. This research focuses on improving emission estimates using the Flux-Divergence method applied to nitrogen dioxide, using data from TROPOMI. All steps in the implementation of the Flux-Divergence method were individually checked to examine their influence on the method. It was also checked if the induced noise from each step can be reduced to improve the resulting emissions.

A first focus of the research is on the improvement of the flux-divergence map for nitrogen dioxide. A large noise reduction was achieved by first computing the divergence on TROPOMI data, and then interpolating to a regular grid to allow for temporal averaging. A second improvement is made by implementing an algorithm that reduces divergence from the wind data set. This enhances emission hot spots along the coast, but also shows that the flux-divergence map is less effective at capturing emission from cargo ships, which are moving targets. The estimation of emission from these sources rely more on an adequate estimation of the sink term.

The research also examines the result of using a different finite difference method in the computation of the divergence, using a different vertical profile a-priori for the TROPOMI data, spatially averaging data on a fine grid, changing the grid resolution and choosing a different wind estimation metric. None of these adaptations lead to significant noise reductions compared to the original implementation. However, it is shown that the retrieved flux-divergence maps are very sensitive to the used a-priori profile. The flux-divergence maps are also moderately sensitive to the used finite difference method, the grid resolution and using spatial averaging. Using a different metric in the computation of a wind map has very little influence on the final flux-divergence map.

A second focus of the research is on estimating the sink term of NO_2. Two approaches lead to satisfactory emission maps. The first optimizes the lifetime of NO_2 to reduce emissions in emission-free regions. The second approach uses NO_2 lifetimes from the DECSO model currently being developed at the KNMI [3].

Finally, this thesis shows that the flux-divergence map contains high amounts of noise when applied to ammonia data from CrIS. Where nitrogen dioxide is mostly emitted from fixed point sources, ammonia is emitted across spread-out agricultural regions. This is not detected in the flux-divergence term. Therefore, the estimation of ammonia emission using the Flux-Divergence method relies strongly on the estimation of a sink term.

Contents

Acknowledgements i

Abstract ii

1 Introduction 1

2 Theoretical Background 5

2.1 Reactive Nitrogen Compounds . . . 5

2.1.1 Nitrogen oxides . . . 6

2.1.2 Ammonia . . . 7

2.1.3 Impact on the environment and human health . . . 7

2.2 Measuring Nitrogen using Satellite Observation . . . 9

2.2.1 Measuring Nitrogen Dioxide (TROPOMI) . . . 10

2.2.2 Measuring Ammonia (CrIS) . . . 12

2.3 Emission retrieval . . . 14

2.3.1 CAMS-REG emission inventory . . . 15

2.3.2 DECSO Method . . . 16

2.3.3 Flux-Divergence Method . . . 17

2.4 Computing Flux - Wind Input . . . 19

2.5 Computing Divergence - Finite Difference Methods . . . 20

2.6 Computing Sink Terms - Estimating lifetimes . . . 23

3 Methodology 24

3.1 Satellite Data Filtering and Domain Settings . . . 24

3.1.1 Domain Settings . . . 24

3.1.2 Filtering TROPOMI data . . . 25

3.1.3 Filtering CrIS data . . . 26

3.2 Flux-Divergence Method . . . 26

3.3 Finite Difference Computation of Divergence . . . 27

3.4 Wind Data Sets . . . 29

3.4.1 Removing Divergence for Wind Data Sets . . . 29

3.5 Spatial averaging . . . 33

3.6 Using TROPOMI grid cells . . . 33

3.6.1 Wind Rotation . . . 34

3.6.2 Computing the Divergence . . . 37

3.7 A-priori Information . . . 39

3.8 Estimating Emissions - Sink Term . . . 39
3.8.1 Constant values . . . 40
3.8.2 Optimized constant values . . . 40
3.8.3 Using DECSO lifetimes . . . 40
3.9 Metrics to Quantify Results Flux-Divergence Maps . . . 41
3.9.1 Total emissions . . . 41
3.9.2 Standard deviation . . . 41
3.9.3 Scatterplots . . . 41
3.10 Validating Results for Emission Maps . . . 42
3.11 Adaptations Flux-Divergence Method for Ammonia . . . 44
3.11.1 Computing Divergence . . . 44

4 Results **48**
4.1 Baseline Method . . . 51
4.2 Finite difference method . . . 52
4.2.1 Second Order Nearest neighbors (DIVSON) . . . 52
4.2.2 Fourth Order Finite Difference (DIVFON) . . . 52
4.3 Wind Dataset . . . 53
4.3.1 WINDDIV . . . 53
4.3.2 WINDMEAN . . . 54
4.4 Spatial Averaging . . . 54
4.5 TROPOMI grid . . . 55
4.6 A-priori Information . . . 56
4.7 Emission Estimation . . . 56
4.7.1 EMISB . . . 57
4.7.2 EMISO . . . 57
4.7.3 EMISD . . . 58
4.8 Flux-Divergence Maps Ammonia . . . 58
4.8.1 NH3TIME*x* . . . 59
4.8.2 NH3MONTHAVG and NH3YEARAVG . . . 59

5 Conclusion and Discussion **61**

References **73**

A Maps of Results **74**
A.1 Baseline Method - Averaging Time . . . 74
A.2 Finite Difference method . . . 75
A.3 WINDDIV . . . 77
A.4 WINDMEAN . . . 78
A.5 SAVG . . . 79
A.6 TROPOMI Grid . . . 80

A.7 DAP 83
A.8 Emissions 84
A.9 Ammonia - NH3TIMEx 85
A.10 Ammonia - NH3MONTHAVG 87
A.11 Ammonia - NH3YEARAVG 88

B Tables **89**

C Used Notation and Abbreviations **91**

1

Introduction

The maintenance of biodiversity is an important cornerstone in sustainable development [4]. For this reason, the member states of the European Union started developing a network of regions in 1992, called the Natura2000 regions. In these regions, special attention is paid to vulnerable ecosystems, the conservation of threatened plant and animal species and promotion of biodiversity. This network now covers 18% of the EU's land territory, and 8% of its waters [5]. These regions are not nature reserves, and therefore human activity is not excluded from these regions. However, harmful human activity within and around these regions, such as agriculture and construction works, must adhere to strict guidelines, to minimize the pressure put on them [6].

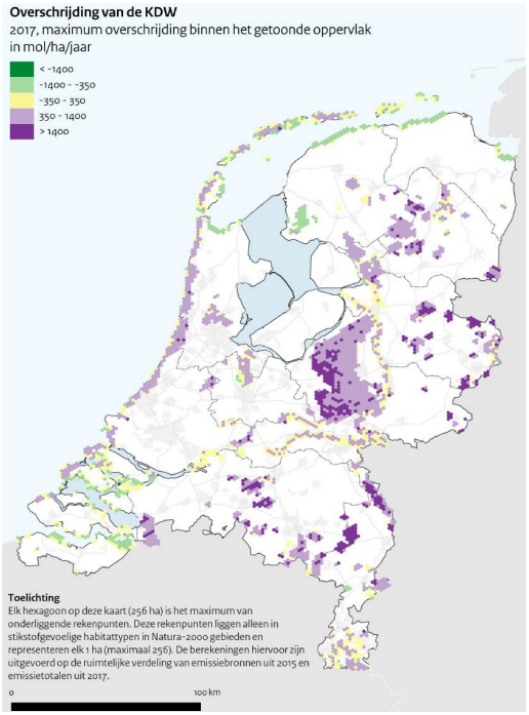

Figure 1.1: Ecologists commissioned by the Ministry of Agriculture, Nature and Food Quality have determined a critical deposition value (KDW) for nitrogen in vulnerable ecosystems: an amount of deposited particles which should not be surpassed. This map shows by how much the KDW is surpassed (or undercut). [7]

In the Netherlands, vulnerable Natura2000 regions are in close proximity to regions with intense anthropogenic activity. One of the largest issues with this proximity is that much of this activity emits the reactive nitrogen compounds nitrogen oxides (NO_x) and ammonia (NH_3). This has detrimental effects on nature as it raises the acidity level and thereby also the structure of the ecosystem. This can lead to loss of biodiversity. Figure 1.1 shows a map of all Natura2000 regions in the Netherlands, and where the nitrogen deposition exceeds levels set to ensure the conservation of vulnerable ecosystems (the so called critical deposition values, or KDW). It can be seen that for many regions, this level is surpassed.

To regulate the emission of nitrogen oxides and ammonia, the Dutch government passed the *Programma Aanpak Stikstof* (PAS) in 2015. The PAS is a legal bill which has been used to grant or reject building permits, based on their nitrogen emission. In 2019, it was ruled by the Council of State that the PAS contradicts European legislation, as it was being used to grant building permits based on future emission reductions [8]. The bill was discarded, and the licenses for thousands of projects, from the building of roads and housing to the fertilization of farming grounds, were retracted and the projects were forced to a stop. As this occurred simultaneous to a growing housing shortage, it led to a crisis, the so called nitrogen crisis or *stikstofcrisis*. As a proposed solution, a new law was passed in 2021, called the *Wet stikstofreductie en natuurverbetering*, or *Stik-*

stofwet for short [9]. Further stringent rules for farmers and plans for buying them out and halving the livestock in the Netherlands, led to fierce protest from the agricultural community. This included the blocking of highways and distribution centers [10]. The validity of the nitrogen models used for the legislation was also publicly doubted by the farmers.

Nitrogen emission is thus a divisive topic in the Netherlands. Something that is often overlooked in the public discourse in the Netherlands, is the fact that atmospheric nitrogen oxides are also detrimental for human health, furthering the need for effective policies [11]. Moreover, the most sources of reactive nitrogen area also sources of greenhouse gases such as carbon dioxide (CO_2) and methane (CH_4). Accurate maps for nitrogen emission and deposition are needed to help draft government policies. The way in which these are derived need to be transparent to foster trust between government and the people affected by its policies.

The Dutch government is supported in the development of measures by the National Institute for Public Health and the Environment (RIVM), who in turn uses data sets made available by the Royal Netherlands Meteorological Institute (KNMI), amongst others. The KNMI delivers concentration, emission and deposition maps for both NH_3 and NO_x. These help to quantify the nitrogen burden on the most vulnerable Natura2000 regions of the Netherlands, and help identify the regions where nitrogen measures are most effective.

One tool that has recently gained importance is the use of satellite data to measure concentrations of trace gases in the atmosphere. A trace gas is a gas that makes up only a fraction (less than 1%) of the atmosphere. For the Earth, the only gases in the atmosphere that are not trace gases, are O_2 and N_2. Using spectrometers for infrared radiance (in the case of NO_x) and ultraviolet radiance (in the case of NH_3), different instruments have been able to create daily concentration maps for these gases, giving a previously unobtainable level of detail and global coverage [12] [13]. Examples of instruments used are the TROPOspheric Monitoring Instrument (TROPOMI, used for NO_2) and the Cross-track Infrared Sounder (CrIS, used for NH_3).

However, a concentration map is not the end product that is needed for policy making. Most trace gases have a background concentration caused by natural sources, and have a certain lifetime in the atmosphere, during which they are transported by wind. Therefore, an important step in using satellite data is converting concentration maps to emission maps and deposition maps. One technique first introduced by Beirle et al. is referred to as the Flux-Divergence method [1]. This method is based on the steady state continuity equation, and states that all divergence of the flux of a trace gas is caused by the sum of its sinks and its sources. In other words, all concentration of a trace gas that can not be explained by its transportation from neighboring regions caused by winds, must be caused by either:

- emission of this trace gas into the atmosphere (in case of a surplus),
- deposition of this trace gas onto the Earth's surface (in case of a deficit),
- being removed by chemical reactions before it reaches the Earth's surface (in case of a deficit)

The equation governing the model is:

$$\nabla \cdot \mathbf{f} = E - S, \tag{1.1}$$

where ∇ denotes the divergence operator, **f** denotes the flux of the trace gas, E represents emission of the trace gas, and S denotes its removal from the atmosphere.

Applications of this method to NO_2 concentration maps have already given promising results in the past, also in collaboration with researchers from the KNMI [14] [2] [15]. This thesis contributes by providing a research that further improves the implementation of this method at the KNMI, and that uses different tools to create flux-divergence maps with less noise, and more distinct emission sources of NO_2 in the Netherlands. The sensitivities of the implementation to different choices in the implementation are also examined. The current KNMI implementation of the method is used as a baseline, to which the different modifications are compared. The research will also focus on different ways to estimate a sink term for NO_2, in order to construct an emission map. One of the implementations uses the input from another emission map model being developed at the KNMI: the Daily Emission estimations Constrained by Satellite Observations method, or the DECSO method [3]. A second goal is to create a

flux-divergence map for ammonia measurements, something that to the best knowledge of the author has not been done before.

This leads to the following research questions and subquestions:

Research Question 1: In which ways is it possible to improve the current KNMI implementation of the Flux-Divergence method when applied to NO_2 TROPOMI satellite data above the Netherlands?

1. *Subquestion 1a: How do different choices in the following factors influence the flux-divergence map:*
   - *grid resolution,*
   - *grid on which divergence is computed,*
   - *finite difference method,*
   - *wind data and*
   - *a priori distribution.*
2. *Subquestion 1b: How can the NO_2 sink term better be estimated by optimizing the NO_2 lifetime or using DECSO estimates for the lifetime?*

Research Question 2: What is the result of a flux-divergence map for NH_3 concentrations from satellite data above the Netherlands?

Chapter 2 first focuses on the theoretical background of this research. All used data sets and methods are discussed. After reading this chapter, the reader should be able to understand the terms used in the research questions. Chapter 3 focuses on the implementation of the experiments done for this research. It is shown how the Flux-Divergence method was first implemented at the KNMI, in order to gain more understanding for how the different choices introduced in the previous chapter can specifically be included in the implementation. Chapter 4 gives the results obtained by the different experiments, which are then discussed and concluded in Chapter 5. Figure 1.2 shows the set-up of this thesis report, and shows how different sections are linked to each research question.

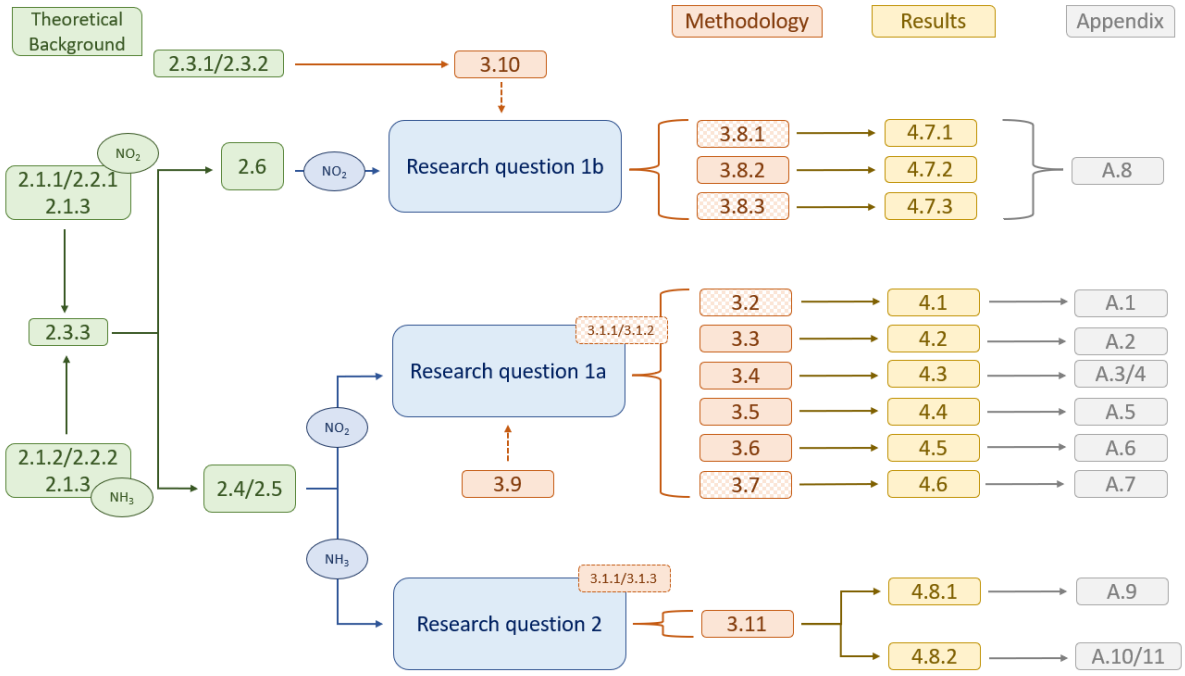

Figure 1.2: A flowchart showing the set-up of the report. A dashed arrow indicates that a section is used to explain the validation techniques used for a certain research question. A checkered methodology section indicates that it is based on code that was implemented prior to this thesis research.

2

Theoretical Background

The goal of this chapter is to give the reader a good understanding of the theoretical background of this research. First, we will discuss the impact of nitrogen compounds on public health and the environment in Section 2.1. The focus lies on nitrogen oxides (NO_x) and ammonia (NH_3), as these are the most prolific nitrogen compounds in the Netherlands. Then, Section 2.2 describes how the atmospheric concentration of both compounds is measured using satellite-based observations. We focus specifically on TROPOMI (for NO_2 concentrations) and CrIS (for NH_3 concentrations). Next, Section 2.3 gives an insight into how the retrieved atmospheric concentration maps can be converted into emission maps, using several different techniques. The main focus of the research is the Flux-Divergence method, which will be thoroughly described in this section. Three aspects of the Flux-Divergence method are further discussed: the computation of the flux (Section 2.4), the computation of the divergence (Section 2.5) and the computation of the sink term (Section 2.6).

2.1. Reactive Nitrogen Compounds

Nitrogen (N) is the most common chemical element in Earth's atmosphere, making up 78% of it, in the form of N_2. This molecule is very stable. However, nitrogen can become harmful when it is transformed into reactive nitrogen, N_r. In this form, the chemical reacts with other molecules present in the atmosphere, to form harmful trace gases. This research focuses on two atmospheric trace gases that consist of reactive nitrogen compounds: nitrogen oxides (NO_x) and ammonia (NH_3). NO_x is a collective term used for molecules consisting of a nitrogen atom reacted with a certain amount of oxygen atoms. In the context of this research, and most literature, it indicates the two most relevant nitrogen oxides contributing to air pollution: nitric oxide (NO) and nitrogen dioxide (NO_2).

Together, NO_x and NH_3 have garnered attention in the Netherlands as focal point of the *stikstofcrisis*, or the nitrogen crisis [16]. More information on this can be found in the introduction of this thesis. This chapter will first focus on NO_x, and then on NH_3.

For atmospheric trace gas concentrations, two terms are important: the source and the sink. A source is any factor that adds the trace gas to the atmosphere. This is usually an emission source on the Earth's surface. A sink is any factor that removes the trace gas from the atmosphere. This is usually a chemical reaction, or deposition onto the Earth's surface. A sink does not mean that the element is not harmful anymore. The reactant or the impact on the surface often leads to the most detrimental consequences of the trace gas. However, after being deposed on the Earth's surface, the trace gas is outside of the scope of satellite measurements. For both NO_x and NH_3, we will discuss its sources (both anthropogenic and natural) and sinks, and its emission trends. A third section focuses on the impact on public health and the environment.

2.1.1. Nitrogen oxides

The main anthropogenic sources of nitrogen oxides are heavy industry and transport (both road and sea). Agriculture also produces some NO_x [16]. Nitrogen oxides are formed when the usually stable N_2 and oxygen (O_2) react with each other under high temperatures, and form nitric oxide:

$$N_2 + O_2 \longrightarrow 2NO \tag{2.1}$$

Nitrogen dioxide is then formed as there is a fast conversion of nitrogen dioxide and nitric oxide into one another, with ozone (O_3) as an additional reactant. Under the influence of light ($h\nu$), NO_2 is converted to NO. In its turn, ozone reacts with NO to form NO_2. This rapid exchange is in balance, also called a "null cycle". This interaction is summarized in the following reactions [17]:

$$NO_2 + h\nu \longrightarrow NO + O \tag{2.2}$$
$$O + O_2 \longrightarrow O_3 \tag{2.3}$$
$$NO + O_3 \longrightarrow NO_2 + O_2 \tag{2.4}$$

The anthropogenic sources of nitrogen oxide emissions are divided over different sectors. These are shown in Figure 2.1, for the Netherlands. As can be seen, the last 30 years have shown a general decline in NO_x emissions. Especially the road transport sector has reduced its emissions greatly as European standards for new vehicles have become more stringent [18]. On the other hand, the shipping sector has not seen a reduction in emissions. There have been some efforts in this industry to attempt to reduce NO_x emissions, such as reducing the speed of the ships (called "slow steaming") [19]. However, the size of the global commercial shipping fleet is increasing yearly, so its emissions have not declined along with the improved cleanliness of the individual ships [20]. Slow steaming is also mostly an economical consideration. In 2021, a Nitrogen Emission Control Area (NECA) was introduced in the North Sea. This measure aims to curb nitrogen emission from cargo ships, especially near the coast [21].

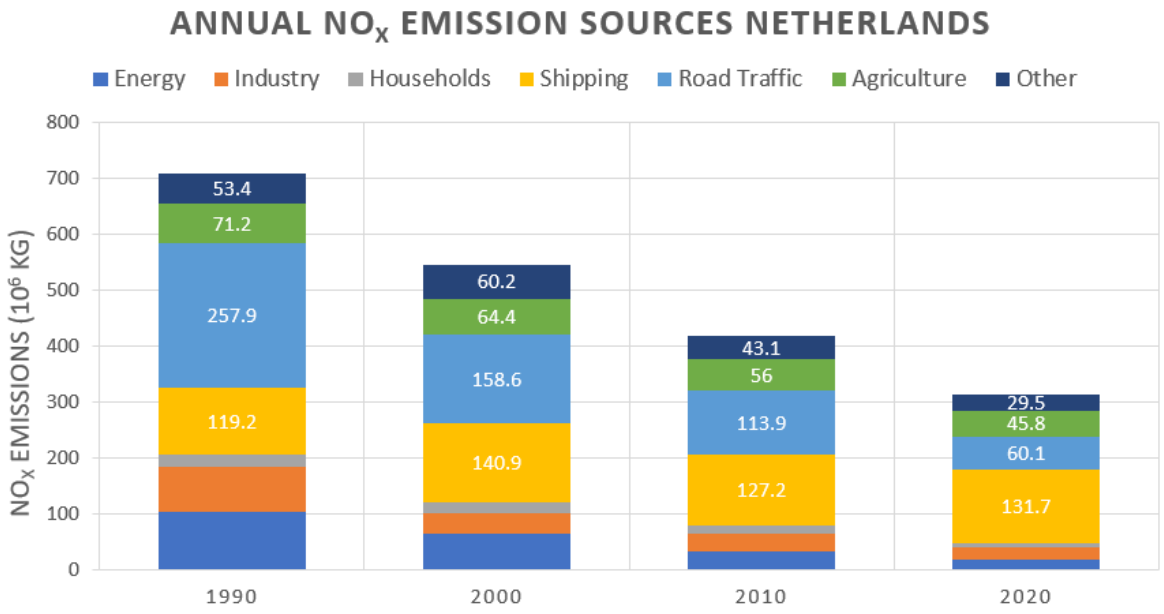

Figure 2.1: Annual NO_x emissions in the Netherlands, separated by source. This chart only includes anthropogenic sources. [22]

There are also some natural sources of NO_x. A main natural source of NO_x is lightning. The rapid energy discharge and subsequent heating of gases forms NO particles. In the case of the Netherlands, this is not an important contributor as lightning is not as common as in other regions. Forest fires are a

similar source of NO_x. However, this does not fully qualify as a natural source, given that a part of these are due to human activity. Another natural source of NO_x are aerobic and anaerobic bacteria in soils. These bacteria are part of a complex nitrogen cycle, which consists of nitrification (where ammonium is converted in nitrate) and denitrification (where nitrate is converted into N_2) processes. NO_x is a natural byproduct of these processes [23]. It is estimated that globally, NO_x emissions originate for 65% from anthropogenic sources [24].

NO_x has a few different sinks. Most NO_x is removed from the atmosphere through chemical reactions. Both NO and NO_2 react with atmospheric OH to form HNO_3. This is the main sink of NO_x. It is mainly agreed that these reactions contribute to around 60% of worldwide NO_x sinks. Another sink of NO_x is its deposition onto the Earth's surface. This deposition can be both wet and dry. In the case of wet deposition, NO_x mixes with moisture in the air, which is deposed onto the Earth via rain, snow or fog. This is also known as acid rain. In the case of dry deposition, NO_x reaches the Earth's surface in gas form, where it is taken up by the surface or inhaled. Deposition is estimated to form around 20% of global sinks. There is quite some uncertainty paired with these estimations, as described by T. Stavrakou et al. [25].

2.1.2. Ammonia

Where nitrogen oxides are mainly formed during combustion processes in heavy industries and transport, anthropogenic ammonia emissions in the Netherlands can be ascribed almost exclusively to agriculture [22]. The largest sources are the use of fertilizer in soil, and the production of animal manure. Surface ammonia is transported to the atmosphere when the surface concentration of ammonia is much higher than the atmospheric concentration in the local air layer above. The amount of emission depends on many factors, including the type of livestock, their feed, how efficiently the nitrogen in their feed is converted to eggs, dairy and other products, and the density of livestock. The air turbulence above the manure also plays a role, as the supply of "fresh" air with lower ammonia concentrations again increases the difference in ammonia concentration between soil and overlying air. As air turbulence is often hard to characterize, it is not evident to quantify the amount of ammonia emissions [26].

The largest natural source of ammonia is the ocean. Ammonia can enter the ocean naturally through air deposition and nitrogen fixation. A similar equilibrium exists to the previously described equilibrium between surface and atmospheric NH_3. When the concentration of NH_3 in the ocean exceeds that of the air layer above, NH_3 is emitted to the atmosphere. Though this reaction is bidirectional, studies show that the oceans are net emitters [27]. It is important to note that ammonia from anthropogenic sources also enters the ocean, for example in the form of run-off water from agricultural lands. These raised levels in ammonia concentration also lead to more ammonia emissions from the ocean. For this reason, oceanic ammonia emissions are not entirely natural.

Figure 2.2 shows NH_3 emissions in the Netherlands from human sources. These have reduced significantly since 1990, but still the agricultural sector remains the main source of emission. The largest reductions in NH_3 emission were made by using different application techniques of manure in the soil, using less fertilizer, reducing the livestock, and transferring to low-emissions stables. However, the main effect of these measures was achieved between 1990 and 2000. Since then, the emissions reductions have stagnated [16].

2.1.3. Impact on the environment and human health

The emission of NO_2 and NH_3 has several detrimental consequences, both on human health and the natural environment.

A first impact on the natural environment, is their contribution to global warming. NO_2 and NO are not greenhouse gases: they do not trap radiated heat from the Earth's surface in the atmosphere. However, they do contribute to the formation of greenhouse gases, most notably ozone (O_3). Some studies even show that local heightened NO_x concentrations can double the amount of ozone present near the ground and in the troposphere [28]. A surplus of NH_3 also leads to a heightened concentration of N_2O (nitrous oxide), a greenhouse gas 300 times more powerful than carbon dioxide. Therefore, reactive

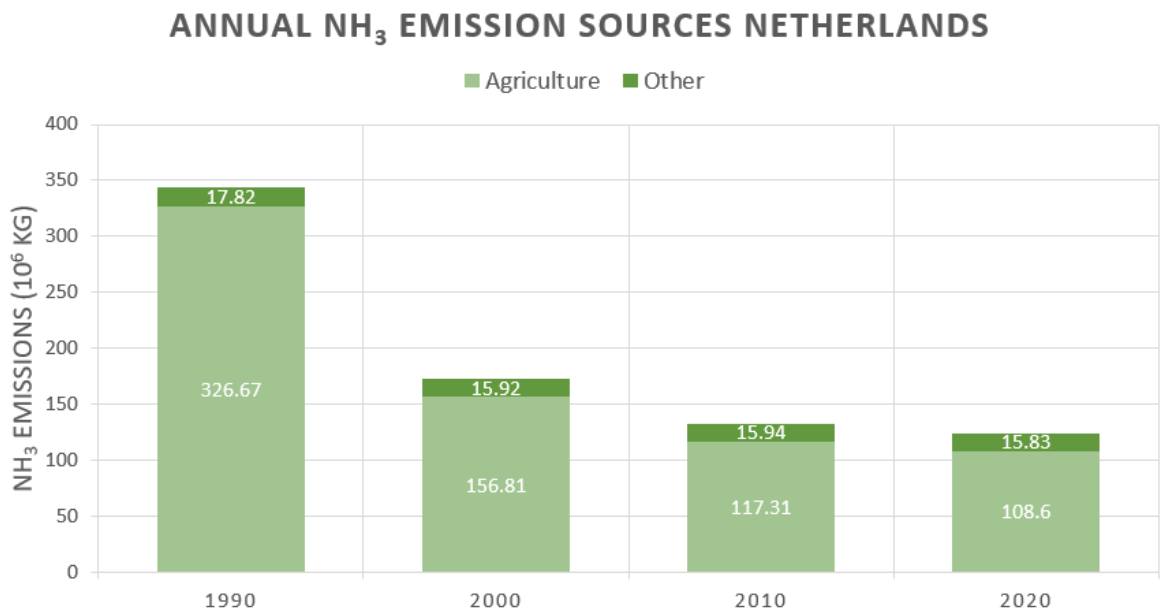

Figure 2.2: Annual NH_3 emissions in the Netherlands, separated by source. This chart only includes anthropogenic sources. [22]

nitrogen indirectly contributes to climate change.

Another facet of the environmental impact of NO_x, is its contribution to surface acidification. NO_x reacts with ozone and SO_2, to form acidic aerosol droplets, which are black in color, and are therefore also referred to as ”acid smut”. NO_2 also reacts with OH to form HNO_3. When deposed on the Earth’s surface, both through dry and wet deposition, this contributes to the rise in acidity in oceans, lakes, forests and soil. Due to the change in acidity, ecosystems start favoring species that prefer an acidic environment, such as brambles and nettles. A large part of species that are not accustomed to these circumstances, decline and may become extinct [29]. Animal species dependent on these plants also decline. NO_x is thus a contributor to loss of biodiversity.

Another important effect of a surplus of nitrogen is eutrophication in coastal waters and lakes, resulting in harmful algal blooms. Nutrients such as nitrogen, but also phosphorus, are food sources for algae. The surplus of these nutrients leads to an exponential bloom of these species which prevents light from penetrating the water. This means that species who depend on their vision, such as pikes, decline. Another harmful effect of a surplus of algae is that they require oxygen to decompose. When the amount of algae is too high, they take up to much oxygen in their decomposition. This leads to an oxygen deficit and the decline of fish and shellfish populations [16]. It also has an adverse impact on the quality of drinking water, and its use for agricultural and recreational purposes, as these algae are potentially poisonous [30]. Another important and harmful effect to the environment is the increased release of methane from eutrophic lakes. Methane can be up to 34 times more effective than CO_2 as a greenhouse gas [31].

NO_x has a direct impact on human health, most prominently on the respiratory system. Different case studies have shown a direct link between heightened concentrations of NO_x, and an increase in mortality cases and hospitalization linked to respiratory diseases such as bronchitis and asthma exacerbation [32] [11].

There are also indirect effects to human health. As mentioned above, a byproduct of the disrupted nitrogen cycle is an increased amount of ozone, which contributes to smog formation. This leads to problems for the respiratory system, as well as irritations to the eyes, ears and nose. Aerosols formed by reactive nitrogen lead to complications in the blood circulation and lungs. [16]
It is clear from this section that a surplus of reactive nitrogen and its byproducts has dire consequences for the environment and human health. Curbing its emission in industry (in the case of nitrogen oxides)

and agriculture (in the case of ammonia) is thus important. For this, we need reliable measurements of atmospheric concentrations of both molecules. One way this can be done is using satellite measurements. This will be further explored in the next section.

2.2. Measuring Nitrogen using Satellite Observation

In order to measure the amount of trace gases in the atmosphere, several methods have been used throughout history. One method is a network of remote installations on the ground which measure concentrations on the ground. For ammonia, this network contains 300 measuring stations, and for nitrogen oxides 73 measuring points are available. Additional instruments are available that focus specifically on wet and dry deposition of nitrogen [16]. The advantage of such a method is that it doesn't depend on weather conditions or other external factors to make its measurements, and therefore gives a coherent time series, with updates at set intervals. A big disadvantage is that the spatial coverage of this method depends on the number of measuring devices, and the measurements are thus limited to these locations.

Since the 1970s, the use of satellites to monitor the Earth has started, and now a large fleet of satellites measure a wide range of indicators. One of the applications of such satellites is measuring the concentration of trace gases in the atmosphere, including NO_x and NH_3. A large advantage of using satellite instruments is that the data procured by one instrument contains measurements covering a large part of the Earth, including remote regions where placing measuring stations is infeasible. Some instruments even have global coverage.

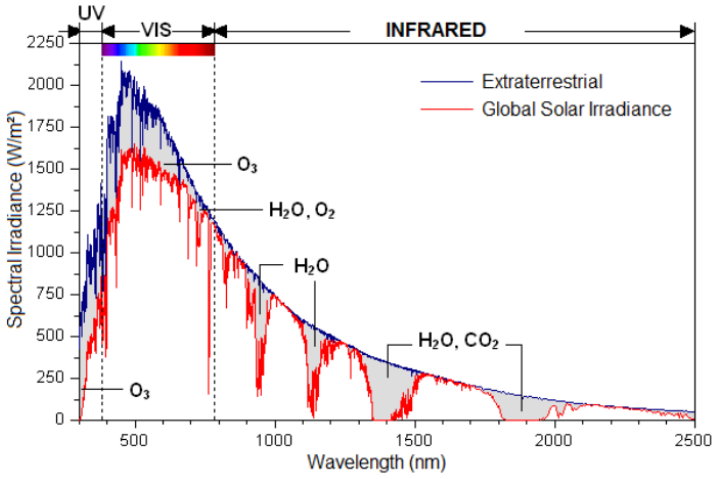

Figure 2.3: This figure shows the solar radiation spectrum. The blue line shows the solar irradiance before passing through the atmosphere, and the red line shows the solar irradiance after passing through the Earth's atmosphere. The absorption spectra of different molecules are also indicated [33].

The instruments that are discussed in this research use back-scattered solar radiation to measure the concentrations of different trace gases in the atmosphere. The sun emits radiation, that is partially reflected by the Earth. In doing so, it passes through the atmosphere, where the present molecules absorb a part of the radiation, depending on their respective absorption spectra. Figure 2.3 shows this process. The blue line shows solar radiance before passing through the atmosphere, and the red line shows solar radiance after passing through the atmosphere and being reflected by the Earth's surface. The red line is what is then measured by satellites. Any discrepancy between the two lines is caused by the absorption of energy on the Earth's surface, or by molecules in the atmosphere. If the absorption spectrum of a molecule is known, a discrepancy between the red and blue line in this location can show the presence of this molecule in the atmosphere. Of course, the reflectivity of the Earth must also be taken into account, with each surface type having different reflective properties. The conversion of an irradiance spectrum measured by a remote instrument to an atmospheric concentration is an interesting subject, but not one that is covered by this research.

Many instruments focus on measuring a part of the radiation spectrum, and therefore are only able to measure atmospheric concentrations of certain molecules. SCHIAMACHY was the first instrument to focus on measuring the entire radiation spectrum, from ultraviolet (UV) to infrared (IR), including the visible spectrum (VIS) [34].

The added value of satellite measurements can not be underestimated. It gives insight into emissions from countries with unavailable or unreliable emission data. It is also useful to track emissions from unpredictable sources, such as gas leaks. An example of this use is shown by Pandey et al., who

found that accidental methane leakage from a gas well in Ohio had a projected emission budget equal to one quarter of the reported annual emission of the entire state [35]. Such methane leaks would be impossible to spot using in situ measuring techniques, as their locations are unpredictable and often remote.

Using satellites to measure atmospheric trace gas concentrations also has certain disadvantages. For instance, the quality of the measurement depends heavily on the atmospheric and surface conditions. Most trace gases are measured using the spectral radiance of light that reflects from the Earth and travels back to the satellite through the atmosphere. If this light is hindered by cloud cover, the data for that measurement is deemed untrustworthy, and can not be used [36]. Elevated surface albedo (or the reflectance of the Earth's surface) also deteriorates the quality of measurements of some trace gases. Elevation of surface albedo can be caused by for example snow and ice-cover. Aerosols also influence the light path in the atmosphere [37].

Another obstacle when measuring trace gases in the atmosphere, is that using reflected radiation spectra gives the complete atmospheric column concentration, and not only the concentration of a trace gas near the surface. There are different methods available to translate the atmospheric column concentration, such as the use of an averaging kernel. However, this requires much research and prior knowledge for each specific trace gas that is being measured [38]. More information about the instruments monitoring NO_2 and NH_3 specifically will be given further on in the report.

Notwithstanding the obstacles that come with using atmospheric satellite data, this method is a great asset to environmental monitoring and calculation. For NO_2 measurements, the KNMI uses data from the TROPOspheric Monitoring Instrument (TROPOMI). For NH_3, data from the Cross-track Infrared Sounder (CrIS) is used. The following section will elaborate on these instruments.

2.2.1. Measuring Nitrogen Dioxide (TROPOMI)

The absorption spectrum of nitrogen dioxide falls in the ultraviolet and visible light region. The majority of the absorption occurs for wavelengths between 300 and 600 nanometers, with a peak at 400 nanometers [39].

Different instruments are available to measure nitrogen dioxide from space. The first satellite measurements of nitrogen dioxide were provided by the Global Ozone Monitoring Experiment (GOME), an instrument aboard the ERS Satellite, which was launched in April of 1995. The resolution of this instrument was 40x320 km and required three days to provide global coverage [40]. This instrument provided measurements until 2011.

The previously mentioned SCHIAMACHY instrument improved on this resolution, with pixels of 30x60 km [34]. Its spectral range contains both the UV spectrum as well as the IR spectrum, something that was not previously attained. The instrument provided measurements until 2012.

A notable improvement to resolution and coverage was made by the Ozone Monitoring Instrument (OMI), flying on NASA's satellite Aura, launched in 2004 [41]. OMI was built in the Netherlands in cooperation with Finnish institutions. The KNMI is the principal investigator of this instrument. The instrument provides near-daily global coverage, and has a resolution of 13 km x 24 km ad nadir (vertically underneath the instrument). It measures spectral radiance in the UV and VIS regions, with a spectral resolution of 0.5 nm [37]. Its improved resolution allowed for emission detection on an urban scale, something that was not possible with previous instruments.

OMI remained the standard in resolution and data quality until the 13th of October, 2017. On this day, the European Space Agency Sentinel 5-Precursor (S5P) satellite was launched, containing the TROPOspheric Monitoring Instrument, TROPOMI for short. The instrument has three spectrometers. It measures spectral radiance in both the UV and VIS spectrum (270-500nm), but also contains two spectrometers in the IR spectrum: one in the near infra-red spectrum (NIR: 675-775nm) and one in the short-wave infrared spectrum (SWIR: 2305-2385 nm). This allows the instrument to measure a great range of pollutants, ranging from ozone (O_3, with an absorption spectrum beginning around 300 nm) to carbon monoxide (CO, with an absorption range until 2400). Figure 2.4 shows the three different spectral ranges measured by TROPOMI, and the atmospheric trace gases measured within each of these ranges with their respective absorption spectra.

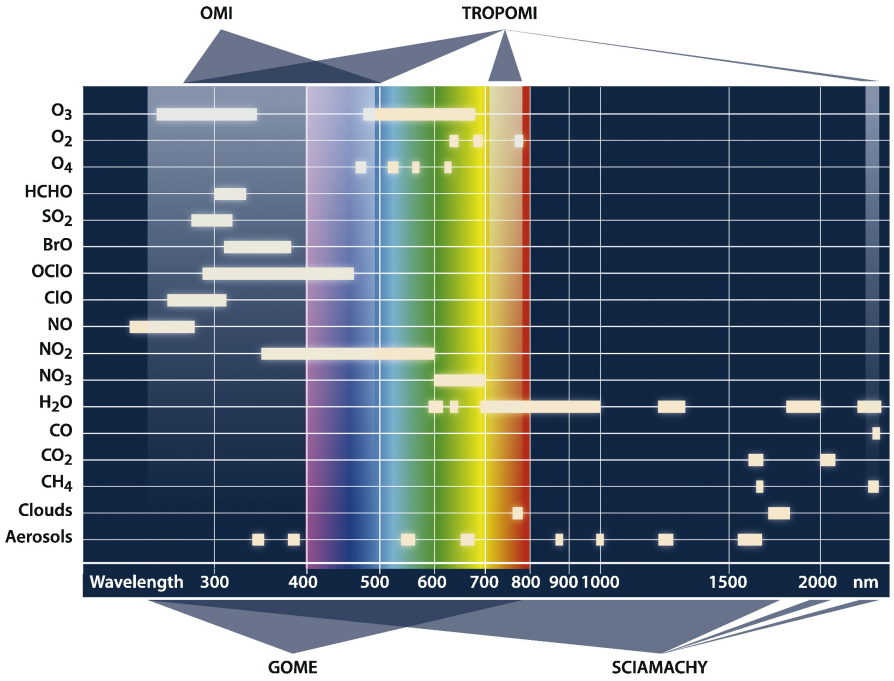

Figure 2.4: This figure shows the spectral range of TROPOMI, including the different pollutants it is able to measure and their respective absorption spectra. It also shows the spectral ranges of the heritage instruments preceding TROPOMI. [12]

The S5P satellite flies in an ascending sun-synchronous polar orbit, at a height of 824 km [12]. A satellite in a polar orbit flies in a North-South direction, passing over the poles on each orbit. A sun-synchronous orbit is an orbit where the instrument always has the same position relative to the sun. The advantage of this route, is that the instrument always has the same pass-over time for each location. For TROPOMI the local equatorial pass-over time is 13:30 PM. This fixed pass-over time makes it easier to compare time series. An ascending orbit means the instrument flies from South to North during the daytime overpass, and from North to South in the nighttime overpass. As it is not possible to measure radiance during the nighttime, all descending observations can be discarded.

The measurement swath of TROPOMI is 2600 km. A swath of a satellite is the surface area that is covered by one fly-over. Upon launch, it started a new measurement every second, in which time it has advanced 7 km. This gives a pixel resolution of 7km in the along-track direction (the orbiting direction of the satellite). On the 6th of August 2019, the along-track distance was improved to a resolution of 5.5 km. The resolution in across-track direction (perpendicular to the orbiting direction) is 3.5 km at the center of the measurement swath [42]. As the viewing angle of the instrument increases, so does the across-track pixel size. Towards the edges, the pixel resolution borders 15 km, although some correction is applied, leading to an irregularity in the across-pixel distance. This is shown in Figure 2.5a. TROPOMI crosses the poles 14 times each day. Combined with the width of the measuring swath, this gives daily near-global coverage. Figure 2.5b shows an example of a daily path of the TROPOMI instrument. This image was created for promotional purposes, and missing data due to cloud cover or other factors has been filled in.

Atmospheric concentraions of a trace gas is also referred to as its column density. TROPOMI directly measures slant column densities (SCD), or the amount of molecules present in the optical path from the Sun to the Earth's surface to the satellite. However, we are interested in knowing the tropospheric vertical column density (VCD), or the amount of molecules of a trace gas present in the troposphere column directly above a ground pixel. To convert a SCD to a VCD, the SCD N_s should first be decomposed into its stratospheric and tropospheric component N_s^{strat} and N_s^{trop}. These can then be converted to VCDs N_v^{strat} and N_v^{trop} [42].

Th conversion from SCDs to VCDs is done using air mass factors M, or the ratio between a SCD and VCD. These are available for both the troposphere (M^{trop}) and the stratosphere (M^{strat}) in look-up tables. However, the first step in these computations is converting N_s to N_v^{strat}. This is done using a

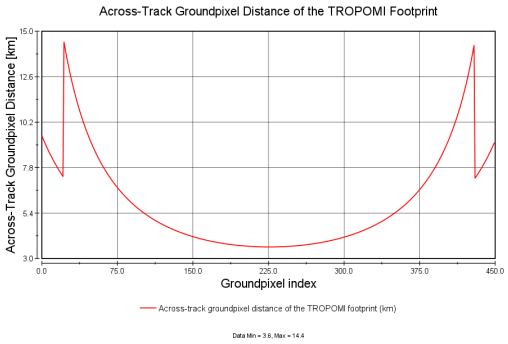

(a) The across-pixel distance along the measurement swath of the TROPOMI instrument. [42]

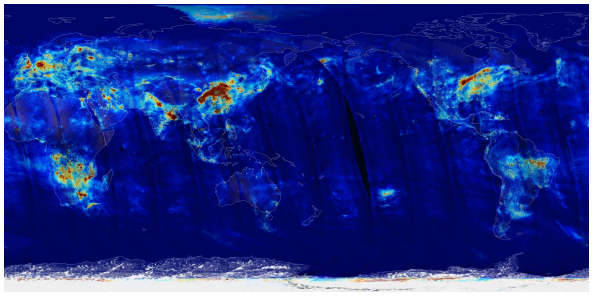

(b) Near-world coverage from the TROPOMI instrument. [43]

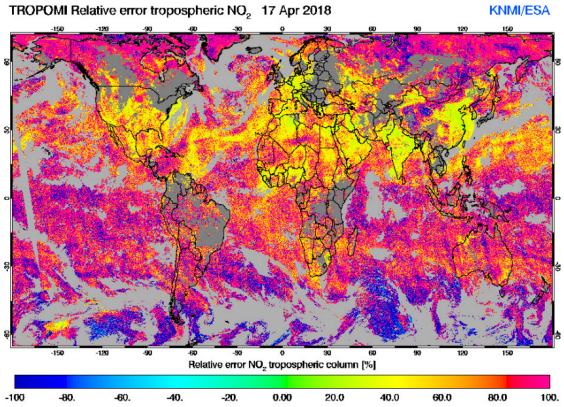

(c) The relative error for NO_2 measurements. [42]

Figure 2.5: The across-pixel distance, the coverage of a single day of measurements, and the relative error of TROPOMI.

data assimilation technique and a-priori vertical NO_2 profiles. Using M^{strat}, N_s^{strat} can be computed ($N_s^{strat} = N_v^{strat} \cdot M^{strat}$. Then, $N_s^{trop} = N_s - N_s^{strat}$, which is then divided by M^{trop} to find N_v^{trop}, or the VCD we are interested in.

In the first versions of the product, this system used an a-priori vertical NO_2 profile information from a chemical transport model named TM5-MP [44]. However, using this a-priori tended to slightly overestimate relatively small NO_2 columns. A higher resolution chemical transport model from the Copernicus Atmosphere Modelling Service (CAMS) was used in 2020, and gave more accurate results when compared to ground-based measurements [45].

The error of the vertical column density of NO_2 is made up of the error in measuring N_s, the error in separating N_s^{trop} from N_s and the error in M^{trop}, which is used to compute N_v^{trop}. These errors depend on many different factors, and therefore differ per pixel. For low values of N_s, the error is dominated by fitting errors, while for large values of N_s, the error is more often caused by uncertainties in the air-mass factor. Figure 2.5c shows the relative measurement error. In remote regions where NO_2 concentrations are generally low and the uncertainty is dominated by measurement error, the error is relatively high, around 100%. For regions with higher NO_2 concentrations, the uncertainty is relatively lower, usually between 20-40%. [42]

2.2.2. Measuring Ammonia (CrIS)

Ammonia (NH_3) has an absorption spectrum in the IR spectral range between 8.3 μm and 13.3 μm, with peak absorption around 10.5 μm. It is therefore outside of the spectral range of TROPOMI. NASA provided the first instrument capable of measuring NH_3 in 2004, the Tropospheric Emission Spectrometer (TES) on the EOS Aura satellite [46]. This was soon followed by an ESA counterpart in 2006, the Infrared Atmospheric Sounder Interferometer (IASI). This contains multiple instruments aboard the METOP series of satellites [47]. In 2011, the Suomi NPP satellite was launched by NASA and NOAA,

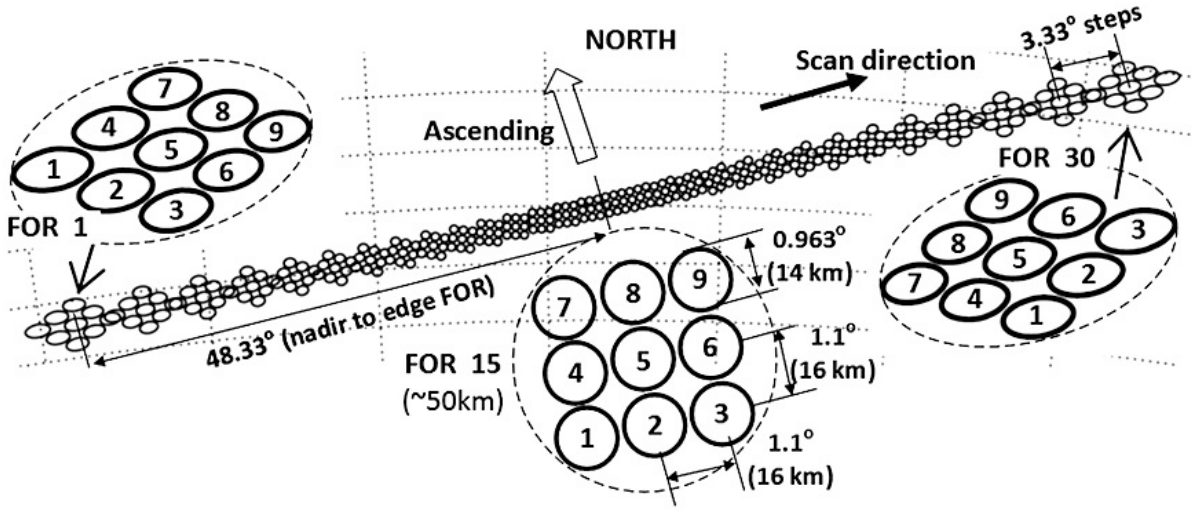

Figure 2.6: The footprint of CrIS, with circular pixels. [49]

containing the Cross-track Infrared Sounder (CrIS). This instrument provides the data for ammonia used in this research. Since then, multiple satellites have been launched that carry CrIS, including the Joint Polar Satellite System (JPSS). The rest of the section will focus on the specifics of CrIS. As this research focuses mainly on NO_2, this instrument is discussed in less depth than TROPOMI.

A sounder is an instrument capable of measuring vertical profiles, or the value of a variable at different heights. The application of CrIS is much broader than just ammonia measurements. CrIS measures vertical profiles of temperatures, moisture and pressure, and is thus used in daily weather forecasts. It also measures cloud top height, and the height of the Planetary Boundary Layer (PBL). Its vertical profiles range from 1013 hPa (the Earth's surface) to 500 (around 5500 meters above the Earth's surface). CrIS measures in three spectral bands, one in shortwave IR, one in midwave IR and one in longwave IR. The longwave IR spectral band (9.13-15.40 μm) is of interest for ammonia measurements [48].

CrIS has a measuring swath of 2200 km, and provides near-global coverage. The footprint is made up of arrays of circular pixels, in a 3x3 set-up. The nadir pixels have a diameter of 14 km, and the centers of the pixels are 16 km apart. At a larger viewing angle, the circles become ellipsoids, and the 3x3 groups are rotated slightly. This is clarified in Figure 2.6.

An important term in the retrieval of atmospheric ammonia vertical profiles, is the averaging kernel, represented as a matrix A. This kernel describes "the sensitivity of the retrieval to the true state" [48]. If $\mathbf{x}$ contains the vector of the true vertical column density, and $\hat{\mathbf{x}}$ contains the measured vertical column density, the averaging kernel is given by:

$$A = \frac{\partial \mathbf{x}}{\partial \hat{\mathbf{x}}} \tag{2.5}$$

In other words, CrIS retrieves a value for the ammonia concentration at different vertical heights. In case of a perfect instrument, A would be the identity matrix, as each measurement would be exactly the true ammonia concentration at that height. However, this is not the case in practice. The measurement for each height contains information about the column density at different heights. The averaging kernel shows for each measurement, how much information is contained for each vertical layer. [50]

Figure 2.7 shows an example of such an averaging kernel for CrIS. The legend shows to which measurement height each averaging kernel pertains. It can be seen that most measurements are most sensitive to ammonia present between a height of 900 hPa and 800 hPa [48]. To conclude, an averaging kernel is needed to create vertical profiles. This technique is not needed for TROPOMI VCD retrieval, as TROPOMI is not a sounder and therefore does not give vertical profiles. However, TROPOMI does require a-priori vertical profiles, as discussed previously, to be able to separate stratospheric concentration from tropospheric concentration.

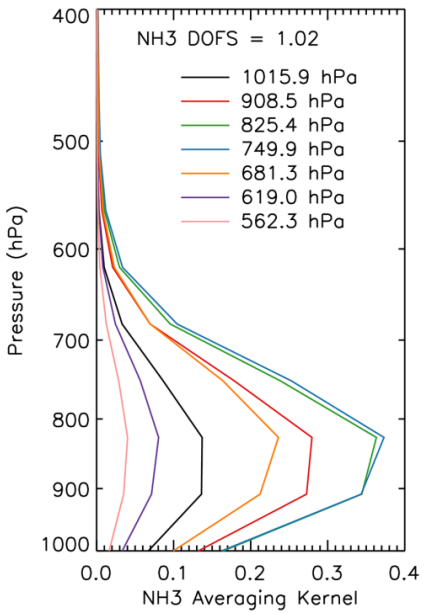

Figure 2.7: The averaging kernel from a measurement taken by CrIS above the San Joaquin Valley in California on the 28th of January, 2013. [48]

Another interesting measure is the area of an averaging kernel. The area is a summation over all averaging kernels for each model level. This gives an indication of the overall sensitivity of the instrument to atmospheric ammonia at different heights. [50]

The determination of the averging kernel is a large field of research withing the remote sensing community, and how it is done for CrIS exactly, is outside the scope of this research.

Another important factor in using ammonia measurements, is the thermal contrast. This is the difference in temperature between the surface and the air layer above (planetary boundary layer). If this difference is too small, CrIS is not able to perform an accurate measurement. For this reason, nighttime measurements are often not included in analysis, as their error margin is too large. The Suomi NPP satellite flies in a sun-synchronous orbit, with a local overpass time of 13:30 PM on the ascending node (when flying from South to North). This overpass time is beneficial for the performance of the sounder, as the thermal contrast is usually at its highest. [48]

The total error of CrIS is made up of two components: the measurement error and the smoothing error. The smoothing error is related to the fact that the vertical resolution is rather coarse, and thus requires some interpolation, which introduces an error. The vertical resolution is the number of layers for which a measurement is obtained. The coarser the vertical resolution is, the greater the smoothing error. The measurement error of CrIS is lower than all its predecessors, allowing it to take measurements at lower thermals contrasts than previously possible. The relative error is larger for low values (<0.5 ppbv, or parts per billion per volume) than for high values (>2.5 ppbv). The measurement error ranges between 10% to 15% for the total column density. When the smoothing error is included, it is 30%. When examining ammonia concentrations at individual heights, the measurement error is around 10% for high values and 30% for low values. Including the smoothing error leads to a relative error between 60% and 100%. [51]

This section gave more insight in how remote sensing instruments can yield concentration maps (or vertical column density maps) for nitrogen oxides (using TROPOMI) and ammonia (using CrIS). The following section gives an overview of how such concentration maps can be used to create emission maps.

2.3. Emission retrieval

Using satellite data, it is possible to get a picture of the vertical column density of NO_2 and NH_3, amongst others. However, it is important to not only find the concentration of a certain trace gas, but also to know what the source of the emission is. Some gases, such as methane, have a certain background concentration caused by natural emission sources. This can make it hard to find the exact location of sources. Wind and turbulence can also hinder finding the location of an emission source.

There are different methods available to retrieve spatial emissions. The focus of this research is the Flux-Divergence method, which was first introduced by Beirle et al. [1]. The KNMI has successfully used this method to create emission maps for NO_2. An in-depth explanation of this method can be found in this next section.

Apart from this method, there are also other available methods, which will be used as validation for the retrieved emission values of the Flux-Divergence method. The first method that will be discussed is the regional bottom-up emissions retrieval inventory from the Copernicus Atmosphere Modelling Service (CAMS-REG). Then, the DECSO method, previously mentioned in the introduction, will be discussed. Finally, the Flux-Divergence method is descirbed.

Figure 2.8: NO_x emissions from the CAMS-REG inventory for 2017. The total for all sectors is shown. Shipping routes, road networks and large industrial centers are clearly visible. [52]

2.3.1. CAMS-REG emission inventory

A first data set that is used to compare the results of this research to, is the Copernicus Atmosphere Modelling Service regional inventory (CAMS-REG). This emission inventory is shown in Figure 2.8 for 2017. This inventory provides annual emission maps for the main air pollutants (NO_x, SO_2 and NH_3 amongst others), on a high resolution (0.05x0.1 degree). The domain of this inventory covers all European countries, including Turkey and a part of Russia. The grid borders are defined by 30°W to 60° E, and 30 to 72°N. This also includes parts of Northern Africa and the Middle East. The data set also divides emissions into different industrial sectors. [52]

The largest part of the data is acquired from national emission inventories. These emission inventories are usually acquired by using a bottom-up approach. Such an approach does not depend on satellite data. Instead, it uses the known emission sources of a certain trace gas, and measured emission rates for source. These are then spatially located on the CAMS grid. For countries where the provided emissions were insufficiently accurate, or incomplete, the emissions were supplemented by the Greenhouse gas Air pollution Interaction and Synergies (GAINS) model. This model has been used to support previous European policies [53] [54].

For emissions from shipping, a separate model is used, called STEAM [55]. This is needed because combining shipping inventories from different countries leads to inconsistencies, and international shipping is not included at all.

Similarly, emissions from agricultural waste burning are treated separately. As this activity is forbidden in the EU, reporting on these emissions is less accurate and hardly available. Therefore, satellite data from different instruments on fire radiative power are combined to create emission estimates. This system is called the CAMS Global Fire Assimilation System [56].

It is hard to quantify the uncertainty of the reported emissions of the CAMS-REG inventory, as the inventory combines many different methods and data sources, each with a different level of uncertainty (if reported at all). Notwithstanding, the CAMS-REG inventory provides an excellent source of data to validate results of European-focused researches, such as this thesis.

2.3.2. DECSO Method

Another emission retrieval method that is interesting to validate results is currently being developed at the KNMI. It is called Daily Emissions estimations Constrained by Satellite Observations, or DECSO for short. The first results were obtained in 2012 by van der A and Mijling [3]. This article used NO_2 emission data made available by the OMI and GNOME measuring instruments (TROPOMI was not yet launched at that time). The research modelled NO_x emissions above Eastern China, a region where, due to the fast growing economy, bottom-up inventories were quickly outdated. The DECSO algorithm uses a chemical transport model to simulate the transport of emitted particles, taking a recent emission inventory as a starting point (for the previously mentioned study, the INTEX-B campaign was selected [57]). A Kalman filter is then used to update the emission inventory, incorporating measured satellite VCDs in the model inversion step.

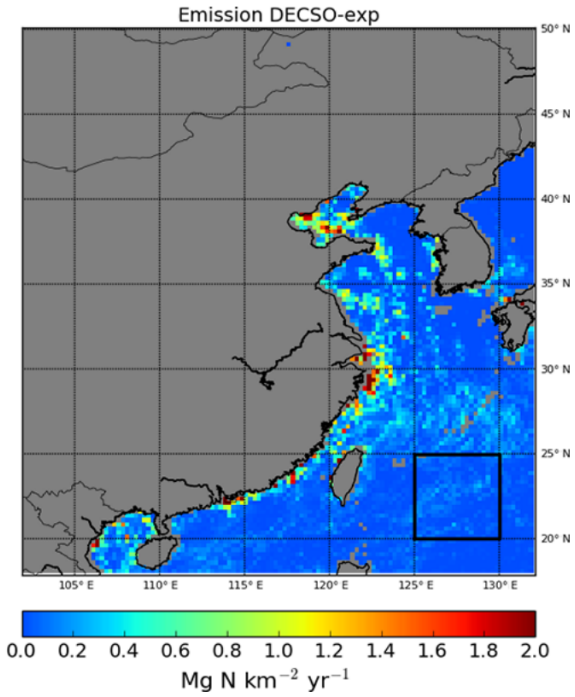

Figure 2.9: NO_x emissions form the DECSO model above the East China Sea, after improvements made by Ding et al. [58].

The convergence rate of this method was sufficiently fast that it allowed for detection of monthly emission trends, specifically the decline in NO_2 emissions caused by government policies implemented around the 2008 Beijing Olympics. New emission sources, such as new power plants, that were not yet included in the a-priori emission inventory, also emerged using this model. It was also able to pick up on mobile sources from shipping traffic. As satellite data is available on a daily temporal resolution, this model uses daily emission updates. A drawback of this, is that the satellite retrieval noise leads to more model noise. Choosing higher emission uncertainties in the model reduces runtime, but adds more noise as well. Choosing a lower uncertainty increases the runtime.

Additions were made to the algorithm by Ding et al. Using a more recent version of the chemical transport model, and filtering out outlying satellite retrieval values further improved the monthly resolution on which DECSO shows emission trends [59]. Better characterization of the sensitivity of the NO_2 observations to NO_x emissions led to a factor ten reduction in the background noise. This revealed low emission sources that were previously indistinguishable from background noise. Moreover, a constraint was set on the emission update, that prohibited unrealistic fluctuations in daily emissions [58]. The results emission map in shown in Figure 2.9.

This model is of special interest to this research for different reasons. On the one hand, it is an emission computation approach with similar advantages to the Flux-Divergence method: it uses satellite data and can thus be updated to the latest emission trends, unlike bottom-up emission inventories. Both models are efficient enough in their computations that they can include daily satellite measurements. Moreover, the DECSO algorithm can find sources not included in the chosen a-priori emission estimate, and the Flux-Divergence method does not require an a-priori emission estimate.

This research also uses the DECSO algorithm as it contains the lifetime of NO_x as an output. As part of the algorithm, the NO_x lifetime is estimated such that the difference between the computed NO_x concentrations and the concentrations simulated by the chemical transport model is minimized [3]. Given that the Flux-Divergence method also requires a lifetime for NO_x to estimate the sink term, it is interesting to analyse the impact of using the DECSO NO_x lifetimes. It must be noted that little research has been done on the validity of these lifetimes.

2.3.3. Flux-Divergence Method

The previous section has described two different methods that can be used to find emission rates of pollutants. This section will zoom in on the Flux-Divergence method, the focal point of this research. This method is based on the steady state continuity equation. Despite its simplicity, it has successfully been used in different research papers, which will also be touched upon in this section. First, the reasoning of the Flux-Divergence method is explained.

The Flux-Divergence method focuses on the transport of an atmospheric pollutant P, also called the flux **f** of P. We describe the flux as a 2-dimensional flow, meaning we can define the flux as:

$$\mathbf{f} = \begin{pmatrix} f^u \\ f^v \end{pmatrix}. \tag{2.6}$$

u denotes the East-West direction, and v the North-South direction.

We model the horizontal transport of P using the wind velocity. This is a reasonable assumption, as wind is the main mode of transport of trace gases through the atmosphere. This means that the flux of P is simply the product of the wind velocity (**w**) and the vertical column density of P (V_P):

$$\mathbf{f} = V_P \cdot \mathbf{w} = V_P \cdot \begin{pmatrix} w^u \\ w^v \end{pmatrix} \tag{2.7}$$

Should there be no sources or sinks for P, this assumption dictates that the flow of P is the same as the flow of wind. However, if there is a source of P in a certain, the heightened concentration leads to an expansion in the flux field, or a net outflow for the surrounding region. Conversely, a sink of P in a region leads to a contraction of the flux field, or a net inflow for that region. The expansion or contraction of the flux field is also called the divergence of the flux, noted as $\nabla \cdot \mathbf{f}$.The divergence of a flux field is given by:

$$\nabla \cdot \mathbf{f} = \frac{\partial f^u}{\partial u} + \frac{\partial f^v}{\partial v}. \tag{2.8}$$

A net outflow of the flux field gives positive divergence, while a net inflow of the flux field gives negative divergence. The assumption made in the Flux-Divergence method is that any divergence in the flux is caused by either an emission source of P (E, in the case of positive divergence) or a sink of P (S, in the case of negative divergence). Summarized, this gives:

$$\nabla \cdot \mathbf{f} = E - S \tag{2.9}$$

To give more insight into this statement, imagine a grid cell with positive divergence of the flux of P. This means that the flux of P in upwind direction is smaller than the flux in downwind direction. In other words, more P exits this grid cell than enters it and we have net outflow. Assuming that the wind did not significantly increase in speed within this grid cell (which is plausible, given the fine dimensions of the grid cells used in this research), it can be supposed that this is caused by P emissions in this grid cell. Conversely, if a grid cell has negative divergence, it means that the flux in upwind direction is smaller than the flux in downwind direction. This means that more P enters a grid cell than exits it, meaning that we have net inflow and there must be some sort of sink within this grid cell. Figure 2.10 also illustrates this.

Equation 2.9 is the crux of the Flux-Divergence method. When one has a satisfactory map of the flux-divergence of P for a certain region, estimating the sink term for P will give an emission map, which helps to detect and quantify emission rates from different sources. Conversely, estimating an emissions term will also give a deposition map for P, something that has a great added value in the protection of vulnerable ecosystems.

A large advantage of using this method, is the fact that we average over the flux of P, instead of over its vertical column density. Down-wind plumes present in the VCD maps, lead to smearing around an emission source when they are averaged temporally. This is avoided when using the divergence of

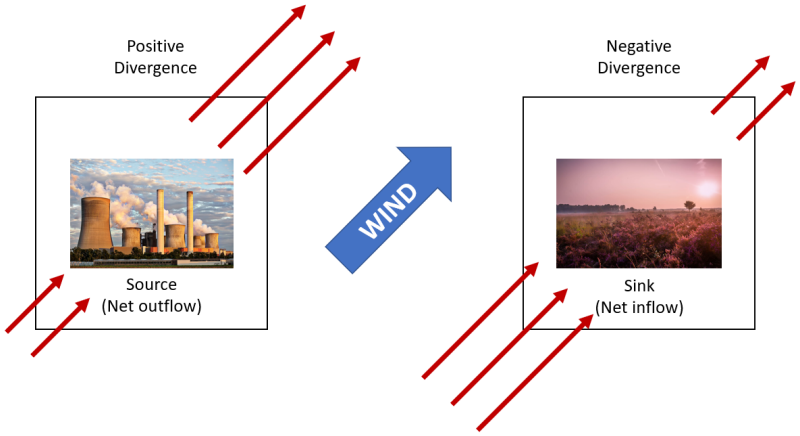

Figure 2.10: An illustration of the positive divergence of a grid cell with a source (left), as opposed to the negative divergence of a grid cell with a sink (right). The wind is shown in blue, and the pollutant flux is shown in red.

flux, because this only peaks at the source of an emission source. Therefore, emission sources are preserved during temporal averaging.

This is illustrated in Figure 2.11. In Figure 2.11a, the results of averaging the VCD of NO_2 over Riyadh over a year is shown. This leads to a large background concentration, with hardly discernable emission sources. However, in Figure 2.11, the flux-divergence is averaged over a year. In this case, we still clearly see all the emission sources. Figure 2.11c shows the effect for a one-dimensional down-wind plume, with no loss of the trace gas. Both the concentration and the flux remain high in downwind direction from the source. The divergence of the flux is only heightened around the emission source.

The TROPOMI instrument gives VCD maps for NO_2 that are highly suitable for the application of this method, as first shown by Stefan Beirle et al [1]. They first used this method in 2019 to map point emission sources near Riyadh, Saudi Arabia. Riyadh has favourable circumstances for satellite measurements, due to low cloud cover and high surface albedo. In the same paper, the method was successfully applied on emissions sources in Germany and South Africa, where these factors are less favourable. The method still performed well, though the uncertainties were higher. This shows that the method is robust under less ideal circumstances, and is not highly susceptible for noisy data. Statistical tools was also used to separate point sources from background concentrations. This will not be further focused on for this research.

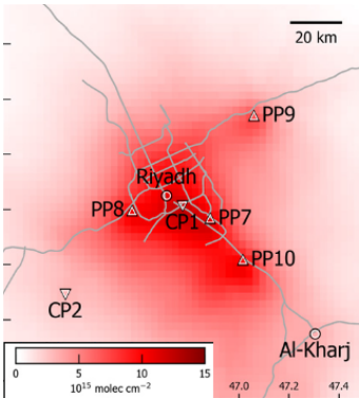

(a) Temporal averaging of the VCD of NO_2 around Riyadh. Data is averaged over a year [1].

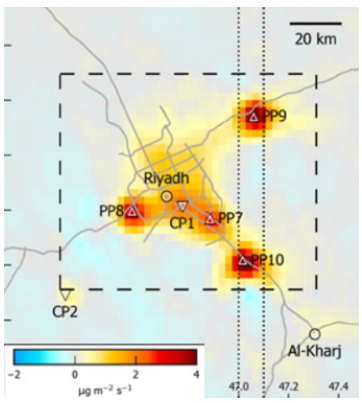

(b) Temporal averaging of the flux-divergence of NO_2 around Riyadh. Data is averaged over a year [1].

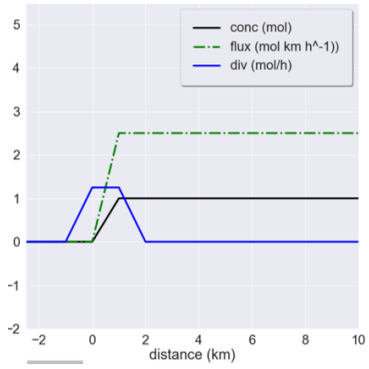

(c) A one-dimensional representation of flux-divergence around an emission source [60].

Figure 2.11: These figures illustrate how a flux-divergence map maintains emission sources when temporally averaged (centre), as opposed to temporally averaging the VCD (left). It is also shown how the flux-divergence is only high around an emission source, and not for the rest of the downwind plume (right).

After the proven efficacy of the method, the Flux-Divergence method was later used to create a global inventory of NO_2 point sources, again using TROPOMI data [2]. Researchers of the KNMI were involved in this paper. The research found that the largest difficulties for the method are linked to gaps in the V_{NO_2} data set. Complex wind fluxes caused by mountainous regions also lead to difficulties, as well as background pollution leading to noise for the computation of divergence. The method was also applied to NO_x emission from oil and gas basins in the United States of America [15]. This paper showed a good agreement between reported emissions from the Flux-Divergence method and different inventories. It also focused on different methods to estimate NO_x lifetimes.

Liu et al. used the method to pinpoint methane (CH_4) emissions, showing that the method is not only suitable for NO_2 measurements. Sensitivity testing showed that the method is robust. [14]

2.4. Computing Flux - Wind Input

As described in the previous section, the Flux-Divergence method is governed by a steady state continuity equation (Equation 2.9). This section describes how the flux **f** (or the transportation) can be computed for NO_2. The flux is computed by multiplying the satellite trace gas concentration data and a wind field, in accordance to previous studies [1] [2]. This section provides more information on which data set is chosen, and how this is interpolated to the grid on which the Flux-Divergence method is run.

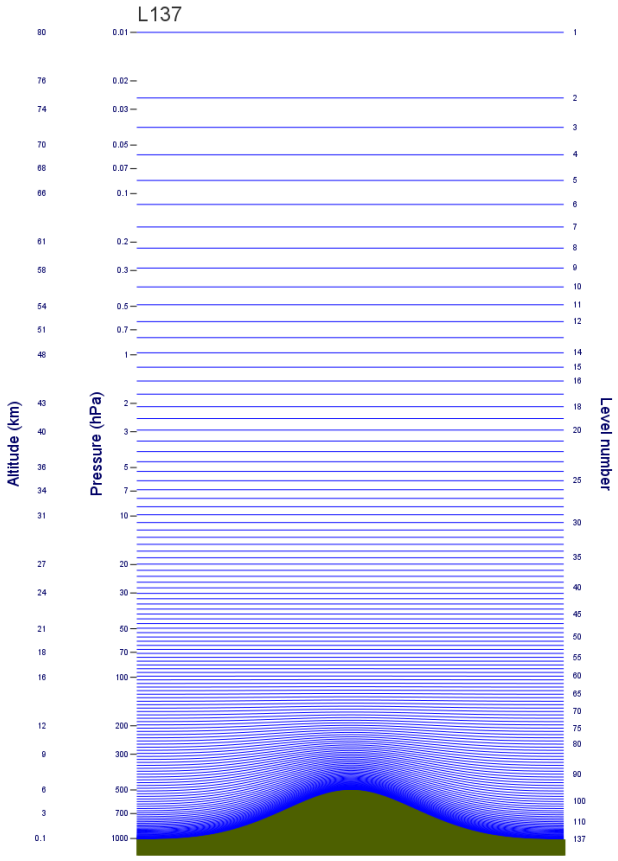

Figure 2.12: The 137 model levels of the ECMWF data sets [61].

The wind data is taken from the data sets from the European Center for Medium-Range Weather Forecasts (ECMWF). The ECMWF is an intergovernmental organization that produces high-quality meteorological data, including horizontal wind velocity data sets. This data set was chosen because research from the World Meteorological Organization (WMO) Lead centers shows that the ECWMF provides the most accurate data. [62] The ERA5 reanalysis of ECMWF historical data is used.

The ERA5 reanalysis uses a 4DVar data assimilation model, with 10 ensemble members. The computations are done on 137 non-equidistant model levels, defined by the pressure layers dividing the levels [63]. Level 1 corresponds with the top of the Earth's atmosphere, where the atmospheric pressure is zero. Level 137 corresponds to the Earth's surface, where the pressure is equal to the surface pressure ($\pm$ 1013 hPa). Figure 2.12 shows the distribution of the model levels. The data is provided in hourly intervals, on 37 pressure levels, and on a regular latitude-longitude grid with a resolution of 0.25x0.25 degrees (around 30 km). The data runs from 1959 until present day [64].

The ensemble spread and mean are also included in the data set. The ensemble spread shows that the uncertainty in wind velocity estimates declines with time, as available wind velocity measurements become more accurate. For the time frame of interest, the ensemble spread ranges between 0.5 m/s

(at the surface) and 1.0 m/s (at the top of the atmosphere). [65]

The wind data set provided by the ECMWF needs to be interpolated in three dimensions before it is suitable to use in the Flux-Divergence method: spatially (both horizontally and vertically) and temporally. Temporal and horizontal interpolation is done linearly. In other words, for each TROPOMI orbit, the local overpass time is chosen (13:30 PM, see Section 2.2), and the closest available hourly data sets are interpolated linearly. Horizontally, the center of each grid cell is chosen, and the four closest ERA5 grid cells are selected, and again interpolated linearly.

The vertical interpolation poses the largest challenge, as choosing a representative height at which to take the wind is not straightforward. Wind has different characteristics at different height layers. The layer closest to the Earth's surface is referred to as the Planetary Boundary Layer (PBL). This is the layer in which wind flow is affected directly by the surface's topographic features, such as mountain ranges and coastal lines. The depth of this layer is usually not more than 1000 meters, but it contracts and expands due to the cooling or heating of air respectively. This effect is seasonal (winter vs. summer), but also daily (night vs. day). Above the PBL, the wind speed is a lot stronger and more uniform, as it encounters less friction from the Earth's surface. The abrupt change in wind velocity often prevents the majority of trace gases to escape the PBL. [66]

To capture the effects of wind on trace gas emission sources, a representative wind velocity of airflow within the PBL is thus needed. In past research, Beirle et al. chose to take the wind at a constant height of 450 m [1]. Choosing different altitudes (730 and 250m) as part of a sensitivity analysis changed the emission results by 10%. In later research, a lower altitude was chosen (300m), to better capture the effects of wind transportation closer to the emission source [2].

Section 3.4 will continue on how the wind data was used in the implementation of the Flux-Divergence method for this research.

2.5. Computing Divergence - Finite Difference Methods

In Section 2.3.3, it was shown how the divergence of the flux of NO_2 can be used to compute emission maps, given that information is available on the sinks of NO_2. However, the information available on the NO_2 flux is not continuous. Both the TROPOMI pixels and the wind velocity data is interpolated to a fixed regular grid, which allows for temporal averaging. This means that the divergence must also be computed on a two-dimensional grid. The formula for divergence is given in Equation 2.8. Two first order spatial derivatives of the pollutant concentration are required.

To compute this on a grid, numerical differentiation is needed. There are many different possibilities in choice for numerical differentiation formulas. This research mainly uses the central difference, both in second order form and fourth order form. Both these formula's are deducted in this section, and their error term is described. The theoretical basis for this section was taken from [67].

Second Order Central Difference

This section focuses on the second order central difference, which is used to find an approximation of the derivative of a function. The first derivative of a continuous and sufficiently smooth function $f(x)$ is noted as $f'(x)$. This can be approximated using the formula for the second order central difference, noted as $Q_{c,2}(h)$. This is found by averaging the formula for forward difference ($Q_f(h)$) and backward difference ($Q_b(h)$):

$$Q_{c,2}(h) = \frac{1}{2}(Q_f(h) + Q_b(h)) \tag{2.10}$$

$$= \frac{1}{2}(\frac{f(x+h) - f(x)}{h} + \frac{f(x) - f(x-h)}{h}) \tag{2.11}$$

$$= \frac{f(x+h) - f(x-h)}{2h}, \tag{2.12}$$

where h denotes the distance between grid cells. The truncation error,

$$R_{c,2}(h) = f'(x) - Q_{c,2}(h), \tag{2.13}$$

can be found by analysing the Taylor expansion of $f(x)$ around x in $x+h$ and $x-h$. Assume $f \in C^3[x-h, x+h]$. We know that there exists a $\xi_1 \in (x, x+h)$ and a $\xi_2 \in (x-h, x)$ such that

$$f(x+h) = f(x) + hf'(x) + \frac{h^2}{2}f''(x) + \frac{h^3}{6}f'''(\xi_1) \tag{2.14}$$

$$f(x-h) = f(x) - hf'(x) + \frac{h^2}{2}f''(x) - \frac{h^3}{6}f'''(\xi_2). \tag{2.15}$$

Substituting this into the truncation error term, we find:

$$R_{c,2}(h) = f'(x) - \frac{f(x) + hf'(x) + \frac{h^2}{2}f''(x) + \frac{h^3}{6}f'''(\xi_1) - (f(x) - hf'(x) + \frac{h^2}{2}f''(x) - \frac{h^3}{6}f'''(\xi_2))}{2h} \tag{2.16}$$

$$= f'(x) - f'(x) - \frac{h^2}{12}f'''(\xi_1) - \frac{h^2}{12}f'''(\xi_2) \tag{2.17}$$

$$= -\frac{h^2}{6}(\frac{f'''(\xi_1) + f'''(\xi_2)}{2}) \tag{2.18}$$

We know that:

$$f'''(\xi_1) \leqslant \frac{f'''(\xi_1) + f'''(\xi_2)}{2} \leqslant f'''(\xi_2) \tag{2.19}$$

Using the intermediate value theorem, we then know that there exists a $\xi \in (\xi_2, \xi_1) \in (x-h, x+h)$ such that:

$$f'''(\xi) = \frac{f'''(\xi_1) + f'''(\xi_2)}{2} \tag{2.20}$$

This gives us that the truncation error for central difference is given by:

$$R_{c,2}(h) = -\frac{h^2}{6}f'''(\xi) = \mathcal{O}(h^2), \tag{2.21}$$

which is an error of second order.

In the context of this research, it is also important to consider the influence of measurement and rounding errors. We note the measured vales for $f(x)$ as $\hat{f}(x)$. Assume the measurement error is at most ϵ, meaning $|f(x-h) - \hat{f}(x-h)|$ is at most ϵ, as well as $|f(x+h) - \hat{f}(x+h)|$.

We take $S_{c,2}(h)$ to be the combination of measurement error and rounding error of the central difference approximation of $f'(x)$. Using the triangle equality to find an upper bound on $S_{c,2}(h)$ gives:

$$S_{c,2}(h) = \left| \frac{f(x+h) - f(x-h)}{2h} - \frac{\hat{f}(x+h) - \hat{f}(x-h)}{2h} \right| \tag{2.22}$$

$$\leq \frac{\left|f(x-h) - \hat{f}(x-h)\right| + \left|f(x+h) - \hat{f}(x+h)\right|}{2h} \tag{2.23}$$

$$\leq \frac{\epsilon}{h} \tag{2.24}$$

The total error $E_{c,2}$ is now given by:

$$E_{c,2}(h) = \left|f'(x) - Q_{c,2}(h)\right| = \left|R_{c,2}(h)\right| + S_{c,2}(h) \leq \left|\frac{h^2}{6}f'''(\xi)\right| + \frac{\epsilon}{h} \tag{2.25}$$

Fourth order central difference

This research also uses a fourth order central difference approximation, as often the data availability of satellite data for NO_2 is high enough that more surrounding data can be included. For this reason, the fourth order central difference is used, as it has higher theoretical accuracy. This formula is noted as $Q_{c,4}(h)$.

Again we want to approximate $f'(x)$, the first derivative of continuous and sufficiently smooth function $f(x)$. First, we deduce the formula for $Q_{c,4}(h)$. As differentiation stencil, the two nearest neighboring data points in both directions are included, meaning the new difference method will have the following form:

$$Q_{c,4}(h) = \frac{k_{-2}f(x-2h) + k_{-1}f(x-h) + k_0 f(x) + k_1 f(x+h) + k_2 f(x+2h)}{h} \tag{2.26}$$

To find values for the constants k_i, the Taylor expansion of $f(x)$ around x is used, which is then evaluated in $x-2h$, $x-h$, x, $x+h$ and $x+2h$:

$$f(x-2h) = f(x) - 2hf'(x) + \frac{4h^2}{2}f''(x) - \frac{8h^3}{6}f'''(x) + \frac{16h^4}{24}f''''(x) + \mathcal{O}(h^5) \tag{2.27}$$

$$f(x-h) = f(x) - hf'(x) + \frac{h^2}{2}f''(x) - \frac{h^3}{6}f'''(x) + \frac{h^4}{24}f''''(x) + \mathcal{O}(h^5) \tag{2.28}$$

$$f(x) = f(x) \tag{2.29}$$

$$f(x+h) = f(x) + hf'(x) + \frac{h^2}{2}f''(x) + \frac{h^3}{6}f'''(x) + \frac{h^4}{24}f''''(x) + \mathcal{O}(h^5) \tag{2.30}$$

$$f(x+2h) = f(x) + 2hf'(x) + \frac{4h^2}{2}f''(x) + \frac{8h^3}{6}f'''(x) + \frac{16h^4}{24}f''''(x) + \mathcal{O}(h^5) \tag{2.31}$$

Substituting this in for $Q_{c,4}(h)$, and using that we want an approximation of $f'(x)$, gives the following set of equations for c_i:

$$f(x) = 0 \Rightarrow \frac{1}{h}(k_{-2} + k_1 + k_0 + k_1 + k_2) = 0 \tag{2.32}$$

$$f'(x) = 1 \Rightarrow -2k_{-2} - k_{-1} + k_1 + 2k_2 = 1 \tag{2.33}$$

$$f''(x) = 0 \Rightarrow h(2k_{-2} + \frac{1}{2}k_{-1} + \frac{1}{2}k_1 + 2k_2) = 0 \tag{2.34}$$

$$f'''(x) = 0 \Rightarrow h^2(\frac{-4}{3}k_{-2} - \frac{1}{6}k_{-1} + \frac{1}{6}k_1 + \frac{4}{3}k_2) = 0 \tag{2.35}$$

$$f''''(x) = 0 \Rightarrow h^3(\frac{2}{3}k_{-2} + \frac{1}{24}k_{-1} + \frac{1}{24} + \frac{2}{3}k_2) = 0 \tag{2.36}$$

Solving this equation gives the following values:

$$k_{-2} = \frac{1}{12} \qquad k_{-1} = \frac{-2}{3} \qquad k_0 = 0 \qquad k_1 = \frac{2}{3} \qquad k_2 = \frac{-1}{12}. \tag{2.37}$$

This leads to the following expression for the difference method:

$$Q_{c,4}(h) = \frac{f(x-2h) - 8f(x-h) + 8f(x+h) - f(x+2h)}{12h} \tag{2.38}$$

The truncation error of the method is given by $R_{c,4}(h) = f'(x) - Q_{c,4}(h)$. Substituting fifth order Taylor expansions into $Q_{c,4}(h)$, we find that

$$R_{c,4} = -\frac{h^4}{180}(-3f(\xi_{-2}) + f(\xi_{-1}) + f(\xi_1) - 3f(\xi_2)), \tag{2.39}$$

where $\xi_{-2} \in (x-2h, x), \xi_{-1} \in (x-h, x), \xi_1 \in (x, x+h)$ and $\xi_2 \in (x+2h)$. Therefore, this method is indeed a fourth order method in terms of h.

Again, we assume the error between the actual function f and the measured function $\hat{f}$ is at most ϵ. We denote this measurement error as $S_{c,4}(h)$. Using the triangle inequality, we can then find an upper

bound on $S_{c,4}(h)$:

$$S_{c,4}(h) = \left| \frac{f(x-2h) - 8f(x-h) + 8f(x+h) - f(x+2h)}{12h} \right. \tag{2.40}$$

$$\left. - \frac{\hat{f}(x-2h) - 8\hat{f}(x-h) + 8\hat{f}(x+h) - \hat{f}(x+2h)}{12h} \right| \tag{2.41}$$

$$\leq \frac{1}{12h}\big(\big|f(x-2h) - \hat{f}(x-2h)\big| + 8\big|f(x-h) - \hat{f}(x-h)\big| \tag{2.42}$$

$$+ 8\big|f(x+h) - \hat{f}(x+h)\big| + \big|f(x+2h) - \hat{f}(x+2h)\big|\big) \tag{2.43}$$

$$\leq \frac{3\epsilon}{2h} \tag{2.44}$$

The maximal measurement error for the fourth order central difference is thus slightly larger than the maximal measurement error for the second order central difference.

Given the fact that this research uses discrete satellite data, we do not know the exact shape of f. Therefore, choosing h such that it minimizes the total error can not be done in this setting. However, the total emission term shows that choosing h too large leads to the truncation error taking over. Conversely, taking h too small gives rise to a large upper bound for the measurement error, meaning noise on the data takes over. This effect is potentially larger when using $Q_{c,4}(h)$ instead of $Q_{c,2}(h)$. It should also be noted that f is not very smooth in this setting. This is also a problem for the accuracy of higher order methods.

Beirle et al. used a fourth order central finite difference scheme to compute the divergence [1]. Later, Liu et al. used a second order central finite difference scheme [14].

2.6. Computing Sink Terms - Estimating lifetimes

The left hand side of Equation 2.9 has already been discussed in Section 2.4 and 2.5. The last remaining term that is required to compute an emissions map for a trace gas is the sink term S. This term should give an estimation for the amount of trace gas that is removed from the atmosphere.

For NO_2, the largest sink during the local overpass time of TROPOMI is its reaction with OH to form gaseous nitric acid (HNO_3) [68]. On the one hand, the amount of NO_2 removed per grid cell depends on the concentration of NO_2 in that grid cell. A higher concentration of NO_2 in a grid cell also means more NO_2 is removed in that grid cell. On the other hand, the sink term depends on the duration of time we assume NO_2 remains in the atmosphere before reacting with OH or deposing onto the Earth's surface. This time is also referred to as the lifetime of NO_2, noted as τ. The higher we assume tau to be, the less NO_2 is removed from a certain grid cell. This leads to the following removal term:

$$S = \frac{V_{NO_2}}{\tau} \tag{2.45}$$

Beirle et al. used a constant average lifetime τ. They estimated the lifetime in a previous study, where downwind plumes of NO_2 were analysed, using OMI satellite data. The lifetime was estimated at around 4 hours, with a 95% confidence interval of 0.5 hours. [69] Gaussian fitting on a linear background was also included to separate peak emissions sources.

In a later study that aimed to catalog NO_x emission sources globally, using the Flux-Divergence method, the sink term was discarded. It was deemed that the divergence was more important for identifying point sources, as this map includes sharper peaks. Adding the sink term caused a smearing effect, making it harder to identify smaller sources. Also, there is no reliable measure for NO_2 lifetime that is representative on a global scale. Discarding this term lead to a 25% decrease in emission rates, thus showing that the Flux-Divergence method is sensitive to the used lifetime. If the method is used to locate emission sources, discarding the sink term helps, but if the method is used to quantify emission rates, much care must be put into the estimation of the sink term. [69]

Liu et al. also discarded the sink term in their study on methane emissions, as methane has a relatively long lifetime of 10 years. [14]

3

Methodology

The previous section introduced the Flux-Divergence method, a method that can be used to generate emission maps for air pollutants such as NO_2, using tropospheric vertical column density (VCD) maps available from satellite data. A baseline code was already implemented by Henk Eskes at the KNMI. This implementation is referred to as the baseline method throughout this paper. For this research, several modifications to the method are explored. The modifications and their implementation are discussed in this chapter.

Firstly, the used data sets are discussed in Section 3.1, including how this data is filtered. Secondly, the implementation of the Flux-Divergence method for NO_2 is described in Section 3.2. Afterwards, the finite difference methods that are applied are considered in Section 3.3. In Section 3.4, the use of wind data in the research, and the removing of divergence within these data sets, will be discussed. Subsequently, the spatial averaging of grid cells is described in Section 3.5. Then, Section 3.6 is dedicated to the use of the TROPOMI grid instead of the latitude-longitude grid, with special attention for wind rotation. Section 3.7 discuses the implementation of using a different vertical NO_2 profile. Next, the approach to estimating the emissions from a flux-divergence map is considered in Section 3.8. Section 3.9 is dedicated to the discussion on how to compare the results of the different flux-divergence maps, and Section 3.10 shows how we can compare different emission maps. Finally, Section 3.11 shows how the Flux-Divergence method is adapted to CrIS data.

3.1. Satellite Data Filtering and Domain Settings

Different data sets are used in this research, most importantly data sets from the TROPOMI and CrIS instruments containing VCDs for NO_2 and NH_3. This section first describes the domain on which we will use these data sets, and then the further filtering that is done to ensure the retrieved data has adequate quality for this research.

3.1.1. Domain Settings

Research question 1 focuses on NO_2 emissions in the Netherlands. The chosen research area is somewhat larger, and also includes Belgium, Luxembourg, Western Germany, North-Eastern France, and South-Eastern England. The advantage of choosing this larger domain as research area is that it includes some low-emissions regions (most notably the Ardennes, also extending into France). Including the Ardennes allows for a validation of the method, as the assumption for this region is that there is very little NO_2 activity here, and thus the flux-divergence and resulting emission here can mostly be interpreted as noise. A map of the research area is shown in Figure 3.1. The boundaries of the region are defined in maximal and minimal latitude and longitude values, which are given by:

$$lon_{min} = 0°30'E \qquad lon_{max} = 10°30'E \qquad lat_{min} = 48°N \qquad lat_{max} = 56°N$$

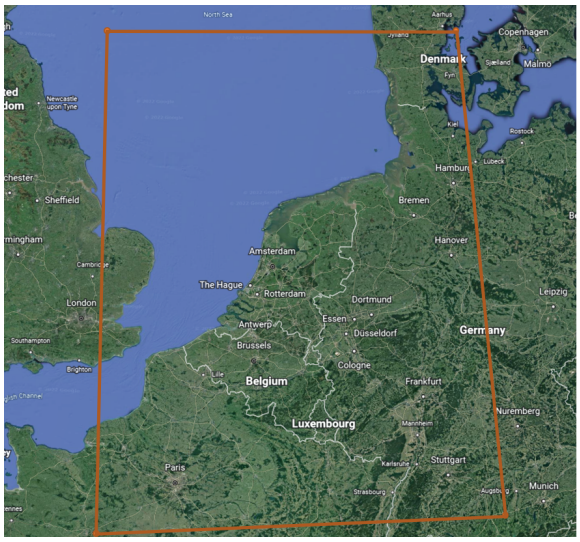

Figure 3.1: A map of the research area. The borders of the research area are marked in orange. (*Source: map created using Google Earth.*)

The TROPOMI instrument measures its data in pixels that differ in location between orbits. This means that it is not possible to directly average TROPOMI data over time on the TROPOMI pixel grid. Therefore, all calculations are done on a regular latitude-longitude grid. Regular means that the grid cells are oriented along the latitude and longitude lines. During calculations, TROPOMI data is first interpolated to this regular grid, and then used in the calculations. This interpolation is done based on the amount of overlap between a TROPOMI pixel and a grid cell. If a TROPOMI pixel completely covers a grid cell, this cell takes over the value of the pixel. However, it often occurs that a grid cell is covered by multiple pixels. In this case, an average is taken of these pixels.The average is weighted depending on the amount of overlap a certain grid cell has with each pixel.

Another advantage of using this regular grid, is the fact that the resolution of the grid can be freely selected. It is possible to chose grid cells that are close in size to TROPOMI pixels. However, given the temporal averaging that is done to combine different orbits, is also makes sense to choose smaller grid cells. This leads to more detailed maps. However, this approach introduces more noise in the map.

For this research, two grid resolutions were chosen for the computations. One lower resolution grid contains grid cells that are close to 5x5 km in North-South and East-West direction. A second higher resolution grid is chosen to be twice as detailed, with a resolution close to 2.5x2.5 km.

In the implementation, the grid size is determined by the constants d_{lat} and d_{lon}, which are defined by the formulas

$$d_{lat} = \frac{lat_{max} - lat_{min}}{n_{lat}} \qquad d_{lon} = \frac{lon_{max} - lon_{min}}{n_{lon}}, \tag{3.1}$$

where n_{lat} and n_{lon} denote the number of grid cells in latitudinal and longitudinal direction. The distance between two latitude degrees is 110 km. The distance between longitude degrees decreases with increasing latitude, but is on average 68 km for the research area. Knowledge of the boundaries of the research region allows for the computation of n_{lat}, n_{lon}, d_{lat} and d_{lon}:

$$\text{5x5 km resolution:} \quad n_{lat} = 176 \quad n_{lon} = 136 \quad d_{lat} = \frac{1}{22} \quad d_{lon} = \frac{5}{68} \tag{3.2}$$

$$\text{2.5x2.5 km resolution:} \quad n_{lat} = 352 \quad n_{lon} = 272 \quad d_{lat} = \frac{1}{44} \quad d_{lon} = \frac{5}{136} \tag{3.3}$$

3.1.2. Filtering TROPOMI data

The data set used for NO_2 VCDs is the TROPOMI product from the S5P satellite, measured in the time frame of June 1st 2019 until August 31st 2019. The summer period is characterized by a relatively low cloud cover, meaning that the data quality and availability is higher.

The data has now been spatially and temporally filtered. However, there are also other checks necessary to filter data based on the quality of the pixels. Most of these data requirements are summarized by the quality factor, a number between 0 and 1, where 0 indicates that the data can not be used and 1 indicates the data quality is high. The quality factor is included in the TROPOMI product. Different aspects influence this factor. These aspects are summarized in Table 3.1. The minimal quality factor is set to 0.75 for this research, excluding cloud-covered or snow/ice-covered pixels. This quality filtering is recommended for all applications of TROPOMI data [42].

Criterion	Quality Factor
Fatal error encountered	0.0
SAA measurement	0.95
Measurement was taken above South Atlantic Anomaly	
Sun Glint Warning	0.93
Interpolation Warning	0.90
Possible bias due to interpolation on partially missing data	
Solar Eclipse	0.20
Solar Zenith Angle (SZA) $> 81.2°$	0.30
SZA$> 84.5°$	0.10
No snow or ice, surface albedo > 0.3	0.20
No snow or ice, cloud radiance fraction > 0.5	0.74
Cloud-free snow or ice	0.73
Cloudy snow or ice	0.25

Table 3.1: Different factors and their influence on the quality factor of TROPOMI data. The final quality factor for a pixel is computed by multiplying the quality factors of the applicable criteria. If no criteria are applicable, the quality factor is 1. [42]

A final filter used is the exclusion of any descending pixels. As explained in the previous chapter, the rotation direction of the satellite ensures that descending measurements are taken during local night-time, and can therefore not be used.

3.1.3. Filtering CrIS data

Two satellite instrument data sets are used for ammonia. One of these is data from the CrIS instrument (see also Section 2.2.2). CrIS data is filtered temporally and spatially in the same way we filter TROPOMI data.

In the same way, there are some quality checks. A part of the CrIS output data is the quality flag. This is an integer ranging from 1 to 5 (-1 also exists, but these correspond to pixels for which the retrieval did not converge, and are thus excluded from the data set). Quality flag 5 is the highest available quality flag. It indicates that the retrieval algorithm converged, large outliers are removed, the signal-to-noise is larger than 1, the thermal contrast is larger than 0 and all data has a minimum degree-of-freedom for signal of 0.1. This filter is recommended for any data comparison, as the uncertainty is low and it only returns persistent VCDs. [70]

An extra filter is also used to remove cloudy pixels (any pixels with a cloud flag equal to 1 are removed). Pixels retrieved during the night are also removed. Finally, pixels above sea are not included. Data above oceans is sparse and ammonia concentrations above sea are usually very low, and therefore harder to retrieve [71].

As previously explained, the footprint of the CrIS instrument is circular, with a diameter of 7 km. In order to interpolate this to a regular grid, the inner square with diagonals of 7 km is determined and treated as a pixel, which is then interpolated to the regular grid.

3.2. Flux-Divergence Method

The theoretical background on the Flux-Divergence method has previously been described in Section 2.3.3, as well as the ways in which it has been used in other research. This section expands on how the method is implemented for this research. The main structure of the implementation of the method is summarized in a flowchart in Figure 3.2. Fortran90 was used as programming language, as the previous implementation of the method at the KNMI was already done in this language.

Two data sets are needed in this method: the vertical column density (VCD) of NO_2 from TROPOMI orbits (shown in grey) and wind velocity data sets from ECWMF (shown in yellow). Both data sets are interpolated to a regular grid, which in the case of TROPOMI data also leads to an array containing the data availability of the VCD. Before interpolating the wind velocity, it must also be processed to a two-dimensional data set, as the ECMWF provides the wind velocity at multiple heights. More on this

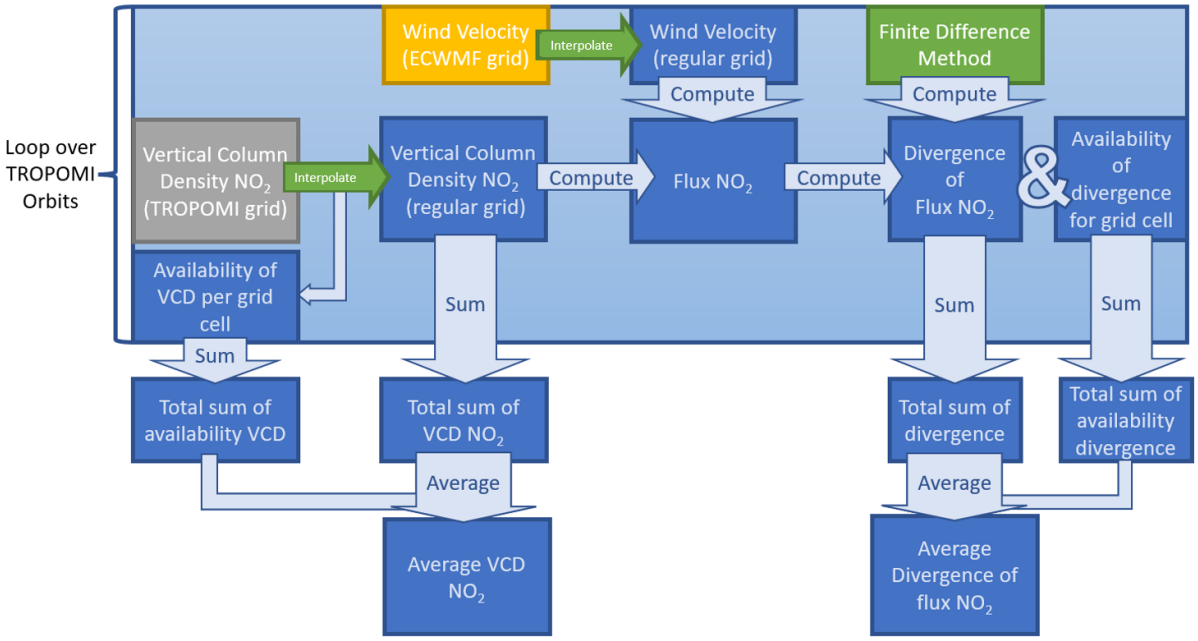

Figure 3.2: This image illustrates the implementation of the baseline Flux-Divergence method. Blue boxes indicate data sets that have been interpolated to the regular grid. Data sets on the TROPOMI grid and the ECWMF grid are shown in grey and yellow respectively. The flowchart should be read from the top left angle, where the wind and TROPOMI data are imported, to the bottom, where we arrive at the averaged vertical column density (VCD) of NO_2, and the averaged divergence of its flux.

is written in Section 3.4. Before importing the TROPOMI orbits, an a-priori distribution for the vertical NO_2 profile must also be chosen (see also Section 2.2.1). This is further explained in Section 3.7. Multiplying the VCD with the wind velocity gives the flux of NO_2.

A note on one of the intricacies of the implementation should be made, which is not shown in the flow chart. In the computation of the flux, we also compute the diagonal flux, in order to also compute the divergence using diagonal neighbors. To this end, the wind velocity on the ECMWF grid (a 3-dimensional grid) must not only be summarized into a 2-dimensional grid, it must also be rotated 45 degrees.

Having computed the flux of NO_2 on the regular grid, it is now possible to compute the divergence of this flux, using the chosen finite difference method (shown in the green rectangle). This is further described in Section 3.3. Computing the divergence requires the availability of data in the surrounding grid cells. This gives a Boolean array for the grid cells for which it was possible to compute the divergence.

As we loop over the TROPOMI orbits, we sum the VCD and the divergence of the flux of NO_2, and both its availability. This eventually allows us to average the total sums, giving the average over the chosen time period of the VCD and the flux-divergence.

The next section elaborates on the used finite difference method.

3.3. Finite Difference Computation of Divergence

A key element in the implementation of this method, is the choice of method that is used to compute the divergence ∇ of the flux $\mathbf{f}$ of the NO_2 concentration. There are a number of discrete finite difference formulas that can be used. More information on the accuracy of these formulas can be found in Section 2.5.

The finite difference method used in the baseline implementation, is the second order central difference method, also including diagonal divergence ($\nabla_{2,b}$). This method averages the second order central finite difference using nearest neighbor cells (in the u (West to East) and v (South to North) direction, $\nabla_{2,n}$), and the second order central finite difference using diagonal neighbor cells (in the $u+v$

(South-West to North-East) direction and $v - u$ (South-East to North-West direction, $\nabla_{2,d}$).

This means two different representations of the flux **f** are needed, one on the original grid ($\mathbf{f}^n$) and one on a grid that is rotated $45°$ ($\mathbf{f}^d$). For this, we need two representations of the wind **w**: one on the regular grid ($\mathbf{w}^n$) and one on the rotated grid ($\mathbf{w}^d$).

$$\mathbf{f}^n = \begin{pmatrix} f^u \\ f^v \end{pmatrix} = V_{\mathsf{NO}_2} \cdot \mathbf{w}^n = V_{\mathsf{NO}_2} \cdot \begin{pmatrix} w^u \\ w^v \end{pmatrix} \tag{3.4}$$

$$\mathbf{f}^d = \begin{pmatrix} f^{u+v} \\ f^{v-u} \end{pmatrix} = V_{\mathsf{NO}_2} \cdot \mathbf{w}^d = V_{\mathsf{NO}_2} \cdot \begin{pmatrix} w^{u+v} \\ w^{v-u} \end{pmatrix} \tag{3.5}$$

V_{NO_2} denotes the VCD of NO_2. The divergence $\nabla_{2,b}$ is then given by the following formula:

$$D = \nabla_{2,b} \cdot \mathbf{f} = \frac{1}{2}\nabla_{2,n} \cdot \mathbf{f}^n + \frac{1}{2}\nabla_{2,d} \cdot \mathbf{f}^d, \tag{3.6}$$

where the nearest neighbor divergence $\nabla_{2,n}$ for grid cell (i, j) is computed as such:

$$\nabla_{2,n} \cdot \mathbf{f}^n_{(i,j)} = \frac{f^u_{(i+1,j)} - f^u_{(i-1,j)}}{2\Delta x} + \frac{f^v_{(i,j+1)} - f^v_{(i,j-1)}}{2\Delta y} \tag{3.7}$$

and the diagonal neighbor divergence $\nabla_{2,d}$ for grid cell (i, j) is:

$$\nabla_{2,d} \cdot \mathbf{f}^d_{(i,j)} = \frac{f^{u+v}_{(i+1,j+1)} - f^{u+v}_{(i-1,j-1)}}{2\Delta d} + \frac{f^{v-u}_{(i-1,j+1)} - f^{v-u}_{(i+1,j-1)}}{2\Delta d} \tag{3.8}$$

Δx denotes the length of a grid cell in its horizontal direction (u, in this case), and Δy denotes the length of a grid cell in its vertical direction (v, in this case). Δd denotes the length of the diagonal of a grid cell. In theory, it actually denotes the distance between the centers of a grid cell and its horizontal, vertical and diagonal neighbor respectively, but in this setting, these distances are the same.

For this research, two extensions to the baseline method are evaluated. For one of these, a simpler approach is used, where only the nearest neighbor second order finite difference is computed:

$$D = \nabla_{2,n} \cdot \mathbf{f}^n \tag{3.9}$$

This requires less data availability, which might be an advantage when satellite data is scarce. In theory, this formula has the same accuracy as the baseline implementation. However, we do lose information in the diagonal direction. The implementation that uses this finite difference formula is referred to as the DIVSON experiment.

A second method uses a fourth order central difference method, which also requires the second neighbor grid cells in the u and v direction ($D = \nabla_{4,n}$). The formula for this method is given by:

$$\begin{aligned} \nabla_{4,n} \cdot \mathbf{f}^n_{(i,j)} = &\frac{f^u_{(i-2,j)} - 8 \cdot f^u_{(i-1,j)} + 8 \cdot f^u_{(i+1,j)} + f^u_{(i+2,j)}}{12\Delta x} \\ &+ \frac{f^v_{(i,j-2)} - 8 \cdot f^v_{(i,j-1)} + 8 \cdot f^v_{(i,j+1)} + f^v_{(i,j+2)}}{12\Delta y} \end{aligned} \tag{3.10}$$

An advantage of this method is that it has a higher theoretical order of accuracy. Also, including further data cells can improve the ability of the Flux-Divergence method to recognize more spread-out emission sources. However, it does require the existence of data in a larger stencil around a grid cell. It performs well on smooth, continuous functions. The TROPOMI NO_2 data set contains a significant amount of noise and therefore this method can give more noisy results in practice. This implementation is referred to as the DIVFON experiment.

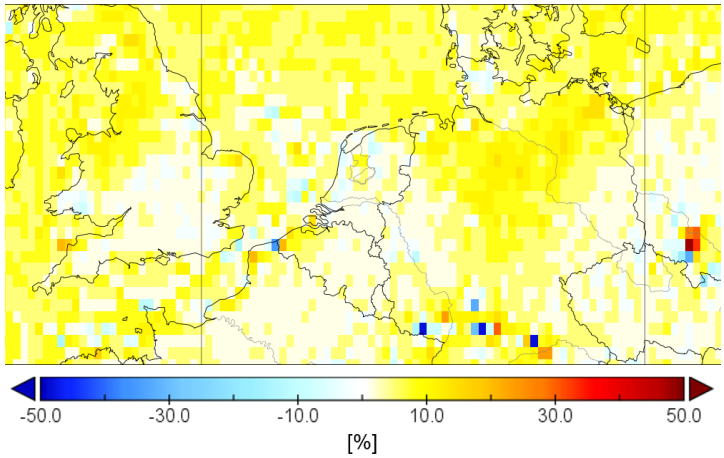

Figure 3.3: A plot of the relative difference between wind speed halfway the PBL, and wind speed averaged over the PBL. The wind speed is measured on the 1st of June 2019, at 11:00 AM.

In summary, two alterations to the baseline implementation are described in this section. One uses Equation 3.9 to compute the divergence. This implementation will be referred to as DIVSON. The other alteration uses Equation 3.10 to compute the divergence. This implementation will be referred to as DIVFON.

3.4. Wind Data Sets

It is assumed that all NO_2 flux is caused by transport through wind. Therefore, in computations, the flux of NO_2 is determined by multiplying NO_2 concentrations with the local wind velocity for each grid cell. The ECMWF wind data is used to provide these velocities, at different model heights. As the Flux-Divergence method reduces the atmosphere to a two-dimensional data set, this height profile must be reduced to one measure. For background on this topic, the reader can refer to Section 2.4.

In the baseline setting, the wind velocity at the height halfway the Planetary Boundary Layer (PBL) was chosen to represent the wind velocity within the PBL. However, due to surface drag, the wind speed distribution in relationship to the height is logarithmic, meaning this height choice can introduce a positive bias.

To remedy this, a different wind data processing is used, where the wind is averaged over the entire PBL. This creates a different data set, with on average slightly lower values for the wind. Figure 3.3 shows the relative difference of both data sets (where the mean wind speed is subtracted from the halfway wind speed, and the half way wind speed is used as a normalizing factor). As can be seen, the halfway wind is slightly higher, as expected.

3.4.1. Removing Divergence for Wind Data Sets

The Flux-Divergence method assumes that any divergence in the flux of NO_2 is caused by sources and sinks of NO_2. However, the flux is the product of the VCD of NO_2 and the wind velocity. Using the chain rule gives:

$$\nabla \cdot \mathbf{f} = \nabla \cdot (V\mathbf{w}) = (\nabla V) \cdot \mathbf{w} + V(\nabla \cdot \mathbf{w}) \tag{3.11}$$

A part of the divergence of the flux is therefore caused by divergence in the wind field, which is not linked to the emission or deposition of NO_2. On a global scale, divergence in wind is caused by transport between low pressure and high pressure areas. On a larger scale, divergence can also be caused by mountain ranges, coast lines, and other topographic features. On a smaller scale, the interpolation of the ECMWF grid to the regular grid can also introduce some divergence.

For this research, the wind divergence above the Netherlands was analysed. This was computed in the same way the divergence of NO_2 was previously calculated, using a second order central diver-

gence scheme, including diagonal divergence. This resulted in the wind map seen in Figure 3.5a. It can clearly be seen that there is some divergence along the coast of the Netherlands, probably caused by the sudden change in drag coefficient above land as compared to above sea.

It is interesting to investigate if it is possible to somehow reduce part of this divergence, by slightly changing the wind field. Considering the scale of the divergence, as compared to the wind velocity, we see that this is several orders of magnitude smaller, so there is reason to believe that this should be possible without changing the wind data set in such a way that it becomes unrealistic.

We thus have the following minimization problem:

Optimization Problem 1 ***Reducing Divergence in a Flux Field.***
Let F be a flux field containing divergence. We want to minimize the divergence of F: $\nabla \cdot F$. ***Cost function****: $(\nabla \cdot F)^\top (\nabla \cdot F)$*
Let F^* be an optimal solution to the problem.
Constraint*: $|F - F^*| < \xi$*

Figure 3.4 shows a graphic representation of this minimization problem. All possible flux fields are represented on the x-axis, and their divergence in represented on the y-axis. The tangent of each point on the minimization function is the gradient of the divergence: $\nabla(\nabla \cdot F)$. In blue, we shows the optimum we search: the flux field with lowest divergence. For this point, it holds that $\nabla(\nabla \cdot F) = 0$. Of course, in reality, the divergence is a function that projects $\mathrm{R}^n \rightarrow \mathrm{R}^n$. The cost function can contain many local minima.

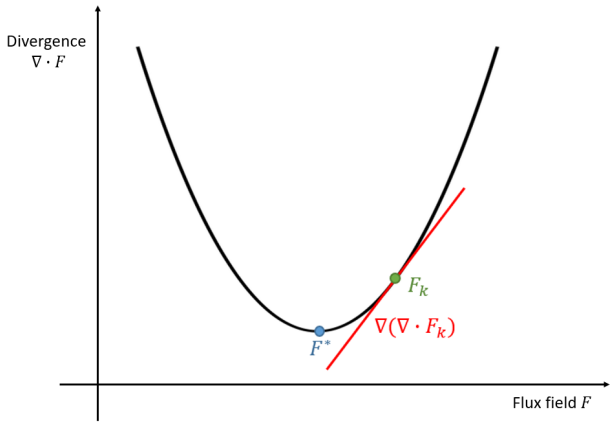

Figure 3.4: A graphic representation of the minimization problem presented in this section. All possible flux fields are represented on the x-axis, and the divergence of these flux fields is represented on the y-axis.

In order to find a flux-field for which $\nabla(\nabla \cdot F)$, Karl Sims described an algorithm [72]. This algorithm is similar to the Newton-Rhapson technique that iteratively approximates the root of a function [73] by continuously adding the derivative of a function to an initial guess for the root. For this thesis, the following algorithm proposed by Karl Sims was implemented:

Algorithm 1 ***Reducing Divergence in a Flux Field.***
Assume flux field F_1 contains divergence. Iterate:

1. *Compute the divergence of vector field F_k: $\nabla \cdot F_k$.*
2. *Compute the gradient of the divergence: $\nabla(\nabla \cdot F_k)$.*
3. *Update vector field: $F_{k+1} = F_k + m\nabla(\nabla \cdot F_k)$*

m is used to scale the update.
Stopping Criterion*: $|F_{k+1} - F_k| < 10^{-5}$* ***or*** *$k > 10000$.*

The functioning of this algorithm does not only have an analytical background, but also a physical background. The principle of reducing the divergence is based on the observation that an area has negative divergence when more flux enters a domain than leaves it. Conversely, a domain has positive divergence when it has a net outflow of particles. Therefore, divergence can be diminished by adding flow away from the area with a negative divergence, and towards areas with a positive divergence. Repeatedly adding the gradient of the divergence to a vector field achieves this, as the gradient is an arrow pointing from low-divergence areas to high-divergence areas.

A side note on the implementation of the algorithm is that the units of the original vector field (F) and the vector field we use as update ($\nabla(\nabla \cdot F)$) are different. In the specific implementation of wind vector field, the units of the original vector field are $\frac{m}{s}$, whereas the gradient of the divergence has units $\frac{1}{m \cdot s}$. To compensate for this, it was chosen to multiply the gradient of the divergence by the dimensions of the grid cells Δx and Δy. So the scaling factor m then becomes $m' \cdot \Delta x \cdot \Delta y$.

It is also important to note that the algorithm must be applied to the wind field after interpolation, as interpolation also introduces small-scale divergence.

Stopping Criterion
In each iteration, the absolute value of the divergence is summed over the research domain. When the decline of this metric is smaller than 10^{-5}, the algorithm is terminated. The sum over the divergence lies in the order of magnitude of 10^{-1}. A limit of 10 000 iterations is also implemented, in case the metric doesn't converge. This number was chosen as experimentation shows that the total divergence has converged for the scale on which this research is done.

Validation of Method
Limited literature was available on this method, so a thorough validation is necessary. In Figure 3.5, the evolution of different metrics are shown in Figures g-i, that can be used to summarize the performance of the algorithm. In Figure 3.5i, the mean divergence of all grid cells is shown in red. This shows a clear decline, which quickly decreases in steepness. However, a decline of the mean does not guarantee a good performance, as an increase in outlying values is not exempted. Figure 3.5j shows that the variance of the method also decreases. Combined with the fact that the total sum of all divergence also decreases (shown in Figure 3.5k), this shows that the algorithm functions properly. In Figure 3.5i, the divergence for different single grid cells are also plotted. This shows that the divergence is not strictly declining when looking at a single grid cell. This plot takes on different forms for different data points. It is possible that for certain grid cells, the divergence may even increase a bit, to allow for an overall decrease.

As can be seen, it is not possible to remove all divergence. The algorithm was iterated 1 000 000 times, and it seems a certain boundary cannot be surpassed. This is due to the fact that this algorithm is focused on a certain domain. Within this domain, it is possible to reduce the local divergence significantly. However there is also a certain inflow and outflow for the entire domain. As we only modify the wind field within our domain, this in and outflow does not change. For this reason, this divergence can not be removed by this algorithm. This does not pose an issue for this research, as the largest part of the divergence is induced by effects within the domain, such as coast lines. This divergence is removed using this algorithm.

To see the algorithm in action, examine Figure 3.5. The algorithm was applied to the ECWMF wind velocity measurements of the 1st of June 2019, at 11:00 AM, interpolated to the fine grid. The initial divergence of the wind is apparent in Figure 3.5a. There is a clear high divergence zone bordering a low divergence zone along the coast line, which makes sense, as this represents a drastic change in surface conditions. Some other high divergence areas can be seen in the Ruhr area. To the right of this image, we first see the divergence after 100 iterations of the algorithm, and then after 1 000 and 10 000 iterations, with a very clear decline in overall divergence. After 10 000 iterations, all local divergence has been smoothed out, and only a slightly positive divergence remains throughout the domain.

It is important that the wind velocity does not change too drastically. This means that, while a decrease in divergence is the primary goal, the wind velocity should still be close to the original data set, as the flux-divergence method heavily relies on wind for its results. The altered wind data set should still have a similar wind speed and wind direction as the original wind data set. In Figure 3.5, Figures e-h show that the overall structure of the wind velocity does not undergo any erratic changes. This has

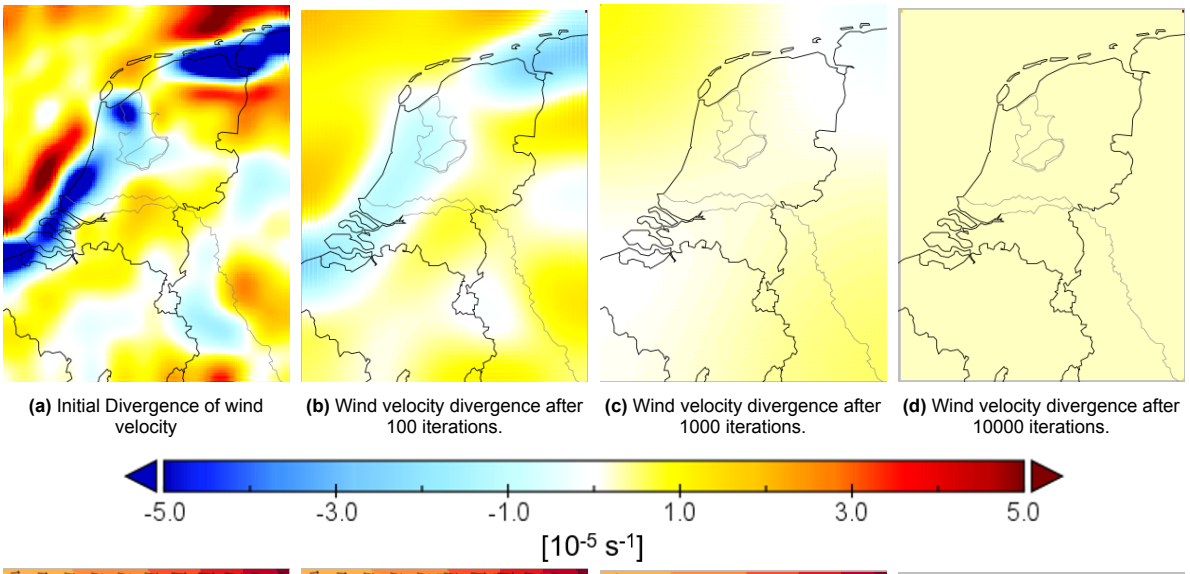

(a) Initial Divergence of wind velocity

(b) Wind velocity divergence after 100 iterations.

(c) Wind velocity divergence after 1000 iterations.

(d) Wind velocity divergence after 10000 iterations.

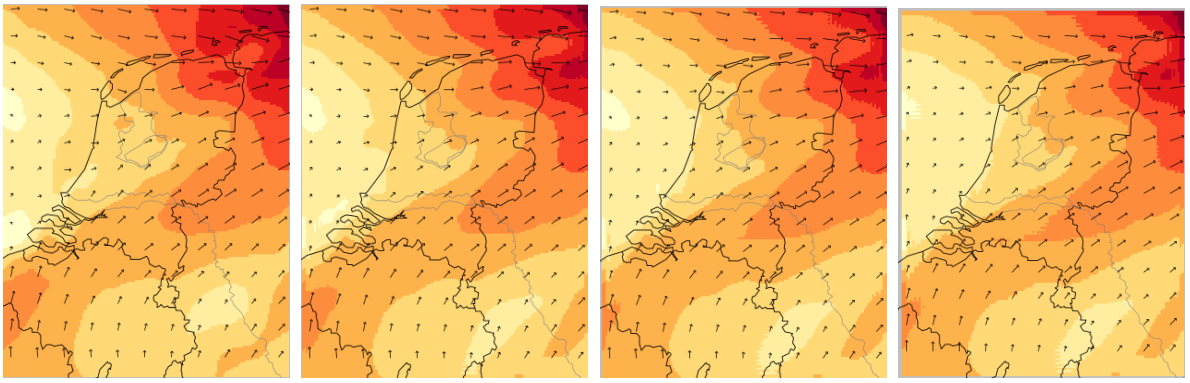

(e) Initial Wind Velocity of research domain.

(f) Wind Velocity after 100 iterations.

(g) Wind Velocity after 1000 iterations.

(h) Wind Velocity after 10000 iterations.

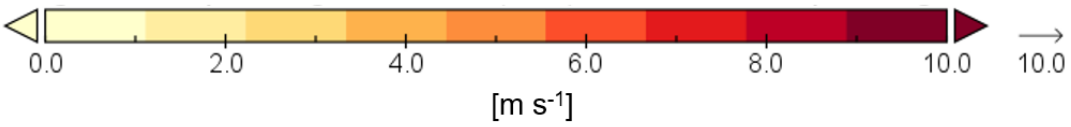

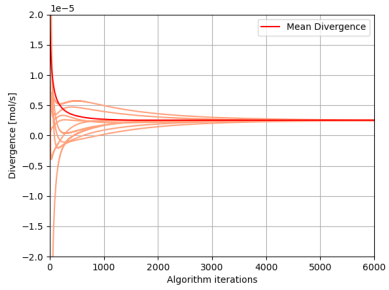

(i) Divergence of single grid cells and mean divergence.

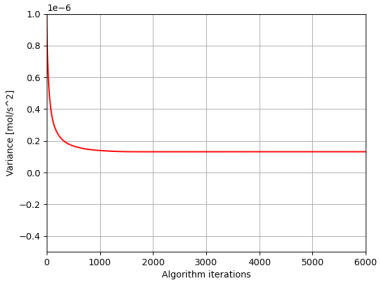

(j) Variance of divergence of all grid cells.

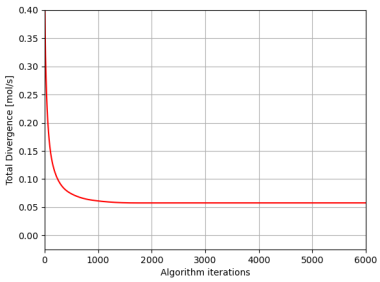

(k) Divergence summed over all grid cells

Figure 3.5: This figure validates the efficacy of Algorithm 1 in reducing divergence in the wind field. Figures a-d show the wind divergence for different algorithm iterations. Figures e-h show the wind velocity, starting with the initial setting, and then after 100, 1000 and 10000 algorithm iterations. The wind data set taken is the halfway wind velocity on 1st of June, 2019, at 11:00 AM. Figures i-k show the value for different metrics on the y-axis, against the algorithm iteration on the x-axis.

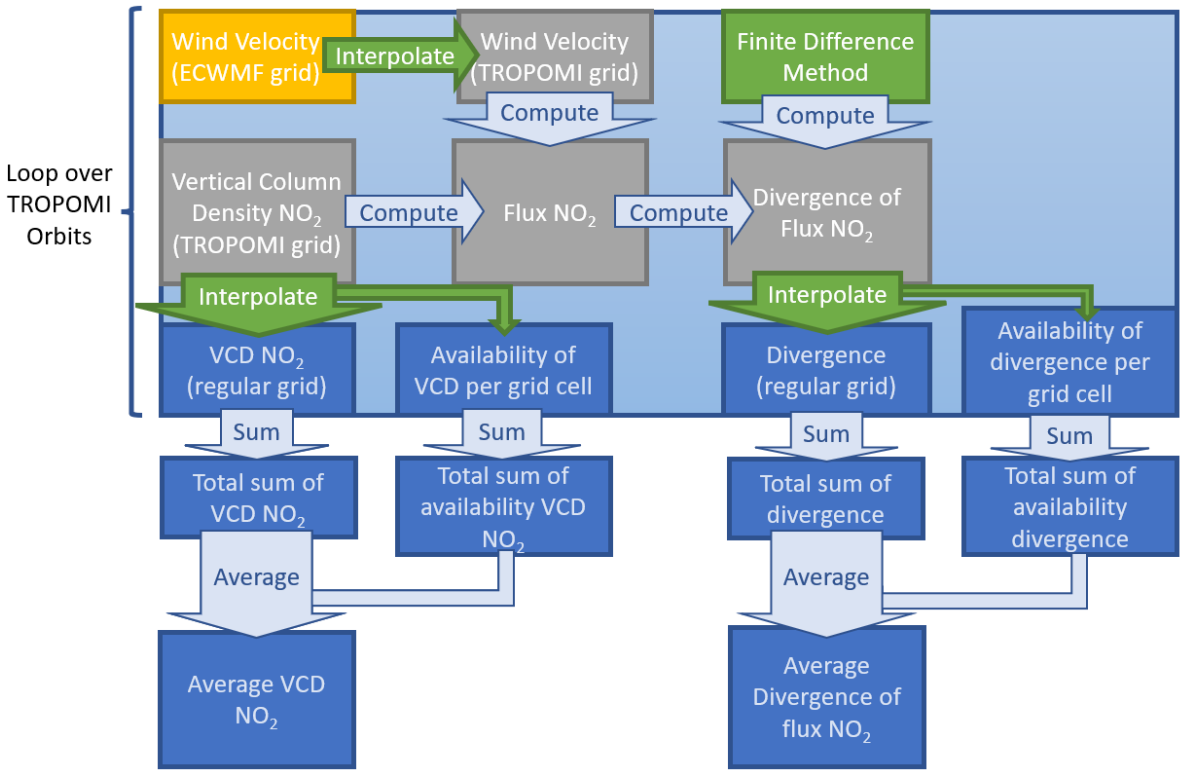

Figure 3.6: A flow chart showing the structure of the implementation of the Flux-Divergence method, using the TROPOMI grid cells to compute divergence. The data sets on the TROPOMI grid area shown in grey, and the data set on the ECWMF grid is shown in yellow.

not been implemented as a specific requirement in the coding of the algorithm.

To summarize, two different adjustments to the baseline scenario were implemented as experiments. One uses a wind data set where the wind is averaged over the PBL, instead of taken at the height halfway the PBL. This experiment is referred to as WINDMEAN. We also use the initial wind data set, but with reduced divergence. This experiment is referred to as WINDDIV.

3.5. Spatial averaging

Using a fixed grid allows for TROPOMI pixels to be averaged to an arbitrary resolution, including a resolution with grid cells that are significantly smaller than the original pixels. However, increasing the resolution will also lead to an increase in noise. In order to reduce this noise, the divergence was first computed on a refined grid. Subsequently, a coarser mesh was obtained by averaging over the refined grid. This was done by first applying the Flux-Divergence method on a 2.5x2.5 km grid, and then taking the average of a square of four grid cells, to eventually have a 5x5 km grid. The process is referred to as spatial averaging. The experiment is henceforth referred to as SAVG.

3.6. Using TROPOMI grid cells

So far, all TROPOMI orbits were first mapped to a regular grid, on which the divergence is computed. However, it is also interesting to examine the consequences of reversing this order, i.e. first computing the divergence on the TROPOMI pixels, and then mapping this to a regular grid, to still allow for temporal averaging. To implement this, the original code had to be adjusted rigorously. Additionally, an option was added to the code that allowed for separately using either only diagonal neighbors for divergence computation, or only the nearest neighbors, or taking an average of both. Initially, it was only possible to add the diagonal divergence to the nearest neighbor divergence, not to use it separately. The structure of the implementation is shown in Figure 3.6.

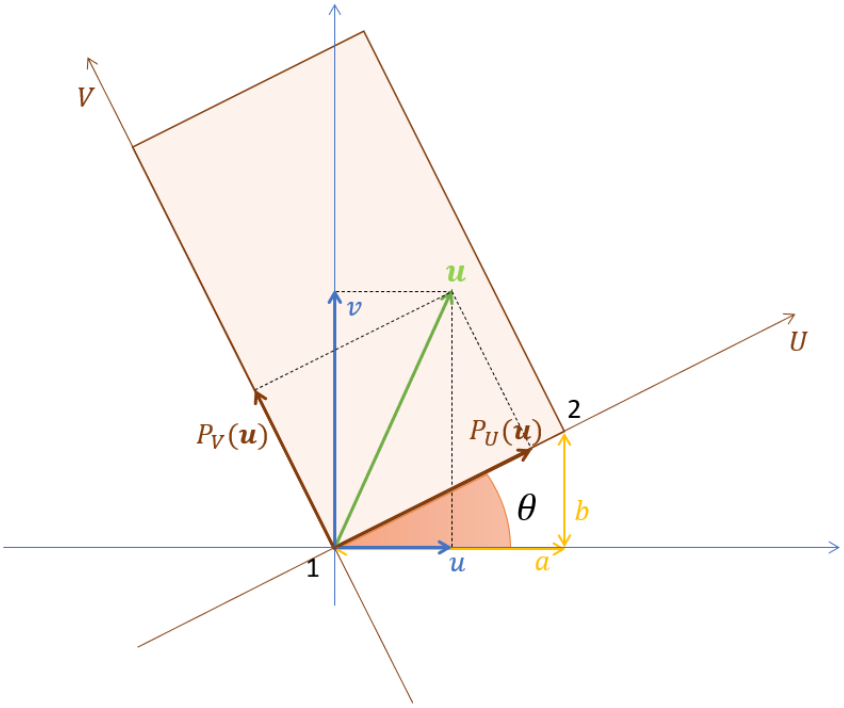

Figure 3.7: A schematic representation of rotating a wind velocity (in green) to a TROPOMI grid cell (in brown). The original u and v components of the wind velocity are shown in blue. The required U and V components ($P_U(\mathbf{u})$ and $P_V(\mathbf{u})$ respectively) of the wind velocity are represented by brown arrows. The angle with which the rotation must be done is denoted by θ. The distances which must be found to compute θ, a and b, are shown in yellow.

When comparing this figure to the original implementation shown in Figure 3.2, it can be seen that the main difference is that the majority of the data sets within the TROPOMI orbit loop are on the TROPOMI grid. In the original implementation, only the imported VCD data set was on the TROPOMI grid.

In the original implementation, the interpolation process of the wind was trivial, as the orientation of both mesh grids were the same. However, the orientation of the TROPOMI grid is different to the orientation of the ECWMF grid, with each TROPOMI pixel having a different orientation between themselves. The rotation formulas used are described in Section 3.6.1.

Moreover, the original finite difference method that was used, assumed that all grid cells had constant dimensions. However, this is not the case for TROPOMI grid cells, where the dimension of a pixel depends on the viewing angle to the satellite. More details on this are given in Section 3.6.2.

3.6.1. Wind Rotation

As explained previously, computing NO_2 flux is done simply by multiplying the VCD of NO_2 in that grid cell by the East-West (u) and North-South (v) component of the wind, which are provided in the ECMWF data set. No rotation is needed for the wind. However, this is only possible as the grid cells of the regular grid also have an East-West, North-South orientation. TROPOMI grid cells follow the track of the S5P satellite, and so, each pixel has a different orientation, and requires a separate rotation of the wind field to be able to compute the flux in that pixel. Instead of an East-West and North-South component of the wind velocity, we need to project the wind velocity on the across-track (U) and along-track (V) direction of the TROPOMI pixel.

First, the ECMWF data set needs to be interpolated to the TROPOMI grid. For each TROPOMI pixel, the four nearest wind grid cells are located. A weighted average of these four values is then taken to determine the value of the wind in North-South direction (v) and West-East direction (u). The weights are determined depending on the distance between the center of the TROPOMI pixel and the center of the wind grid cell.

After the u and v components for the wind are determined for each TROPOMI pixel, the wind is rotated. Figure 3.7 shows a schematic representation of the situation at hand. As the coordinates of the angles of the TROPOMI pixel are available, it is possible to compute the size of a and b, both marked in yellow. More specifically, a is computed by subtracting the longitude of angle 2 from angle 1, and b is computed by subtracting the latitude of angle 2 from angle 1. The different possible quadrants of θ are implemented as separate cases, and also account for the cases in which θ falls exactly on the boundary of two quadrants (though this will hardly occur in practice). We can then compute θ using $\theta = \arctan(b/a)$. Note that we need to take θ in negative direction (so $-\theta$) to get the correct rotation direction. Finally, the projection of the wind velocity on U and V (noted as $P_U(\mathbf{u})$ and $P_V(\mathbf{u})$ respectively) are computed using a rotation matrix:

$$\begin{pmatrix} P_U(\mathbf{u}) \\ P_V(\mathbf{u}) \end{pmatrix} = \begin{pmatrix} \cos(-\theta) & -\sin(-\theta) \\ \sin(-\theta) & \cos(-\theta) \end{pmatrix} \cdot \begin{pmatrix} u \\ v \end{pmatrix} \tag{3.12}$$

If the diagonal flux is included in the computation of the divergence, a more complex rotation is needed. This situation is sketched in Figure 3.8. In the baseline scenario, a simple 45 degree rotation was needed to determine the direction of the diagonals and obtain the diagonal flux.

However, the across-track distance of TROPOMI pixels varies, as was previously shown in Section 2.2.1, and depends mostly on the viewing angle of the satellite. This causes each diagonal to be non-orthogonal in relation to the other diagonals. Moreover, opposite diagonals are not in line with each other, so the diagonals do not represent a coordinate system. Instead of the original diagonals $u + v$ and $v - u$, we now have four diagonal directions, formed by the lines connecting the centers of the central grid cell and its four diagonal neighbors: $U + V$ (or $pUpV$), $U - V$ (or $pUmV$), $-U + V$ (or $mUpV$) and $-U - V$ (or $mUmV$). The corresponding projections of wind velocity **u** on these diagonals are noted as $P_{pUpV}(\mathbf{u})$, $P_{mUpV}(\mathbf{u})$, $P_{mUmV}(\mathbf{u})$ and $P_{pUmV}(\mathbf{u})$.

Figure 3.8 shows a schematic representation of wind rotation for diagonal wind velocity computation. The directions U and V divides the field into four quadrants, referred to as the original quadrants, and denoted as 1, 2, 3 and 4. The diagonals divide the field into four new, non-orthogonal quadrants (from hereon out called diagonal quadrants) and are named I, II, III and IV.

As was previously mentioned and can also be seen in the figure, the diagonal does not form an orthogonal coordinate system, and opposite diagonals are not in line with each other. Instead, it is possible to project the wind onto the closest diagonals, which gives relevant values that can be used to quantify the diagonal wind. So, the flux will have two components, one on either $pUpV$ or $mUmV$ and one on either $mUpV$ and $pUmV$. $pUpV$ and $mUpV$ are taken to be the positive directions, and $mUmV$ and $pUmV$ are taken to be the negative directions.

A first step is therefore to determine between which diagonals the wind falls. This can be done by comparing the slope of the wind and the diagonals. In the example shown in Figure 3.8, the projections of interest are $P_{pUpV}(\mathbf{u})$ and $P_{mUpV}(\mathbf{u})$ and are shown in red.

In order to compute these projections, the angles α and β need to be calculated. These represent the angles between the flux and the diagonal directions. α can be computed by calculating τ and σ. τ is the angle between **u** and U. σ is the angle between $pUpV$ and U. Subtracting these two gives the angle between **u** and $pUpV$. Additionally, calculating ρ gives the value for β. ρ is the angle between U and $mUpV$. Therefore, τ, ρ and β should add up to π, allowing us to derive the value for β.

In order to compute σ and ρ, the arctangent of these angles can be used. For this, we need to compute the distance between the centers of the nearest neighbors pixels and the central pixel. The distance between central pixel (i, j) and pixel $(i + 1, j)$ is noted as pU. Similarly, pV denotes the distance between pixel (i, j) and $(i, j + 1)$, mU denotes the distance between the central pixel and $(i - 1, j)$ and mV denotes the distance between the central pixel and pixel $(i, j - 1)$. These are shown in the figure in violet. Computing these distances can be done using the formula for Euclidean distance as the coordinates of the central point of each pixel are given. This gives the following values:

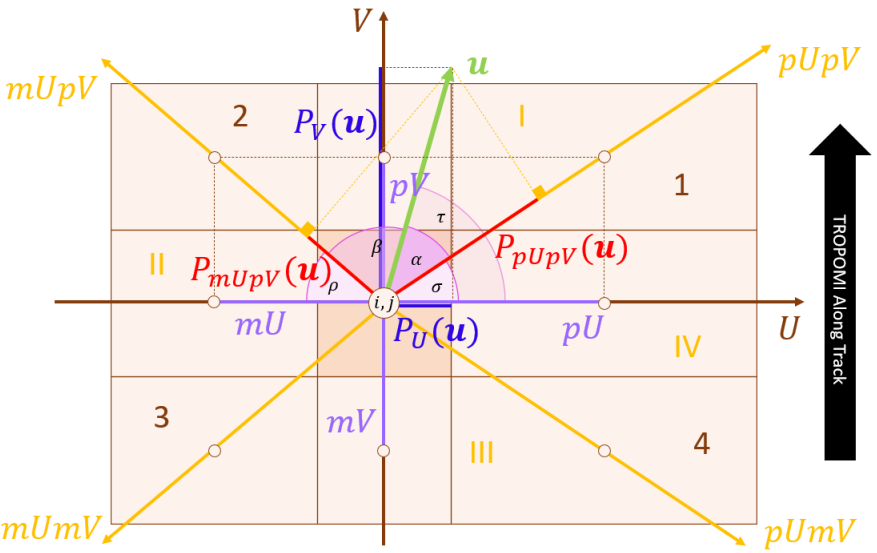

Figure 3.8: A schematic representation of wind projected onto diagonals. The brown background cells represent a TROPOMI pixel at location i, j and its diagonal and nearest neighbors. The wind velocity **u** is shown in green, and the components of its rotation to the TROPOMI grid (U and V in brown) are shown in blue. The projections of interest ($P_{pUpV}(\mathbf{u})$ and $P_{mUpV}(\mathbf{u})$) are shown in red. The distances between the nearest neighbor TROPOMI pixels mU, pU, mV and pV are shown in violet. The black arrow denotes the flying direction of the TROPOMI instrument.

$$pU = \sqrt{(lon_{i+1,j} - lon_{i,j})^2 + (lat_{i+1,j} - lat_{i,j})^2} \tag{3.13}$$

$$pV = \sqrt{(lon_{i,j+1} - lon_{i,j})^2 + (lat_{i,j+1} - lat_{i,j})^2} \tag{3.14}$$

$$mU = \sqrt{(lon_{i-1,j} - lon_{i,j})^2 + (lat_{i-1,j} - lat_{i,j})^2} \tag{3.15}$$

$$mV = \sqrt{(lon_{i,j-1} - lon_{i,j})^2 + (lat_{i,j-1} - lat_{i,j})^2} \tag{3.16}$$

$lon_{i,j}$ and $lat_{i,j}$ denote the longitude and latitude coordinates for pixel (i, j).

τ can also be computed using the arctangent, as $P_U(\mathbf{u})$ and $P_V(\mathbf{u})$ are known.

Combining this information, the following formulas are needed to compute all relevant angles:

$$\tau = \arctan(\frac{P_V(\mathbf{u})}{P_U(\mathbf{u})}) \tag{3.17}$$

$$\sigma = \arctan(\frac{pV}{pU}) \tag{3.18}$$

$$\rho = \arctan(\frac{pV}{mU}) \tag{3.19}$$

$$\alpha = \tau - \sigma \tag{3.20}$$

$$\beta = \pi - \tau - \rho \tag{3.21}$$

Using that the length of **u** is known ($|\mathbf{u}| = \sqrt{P_U(\mathbf{u})^2 + P_V(\mathbf{u})^2}$), the cosine of α and β can be used to compute $P_{pUpV}(\mathbf{u})$ and $P_{mUpV}(\mathbf{u})$:

$$P_{pUpV}(\mathbf{u}) = |\mathbf{u}| \cdot \cos\alpha \tag{3.22}$$

$$P_{mUpV}(\mathbf{u}) = |\mathbf{u}| \cdot \cos\beta \tag{3.23}$$

Depending on the original quadrant and diagonal quadrant in which the flux falls, different arctangent values are needed to compute σ, ρ and τ. It also differs per diagonal quadrant which diagonal is used

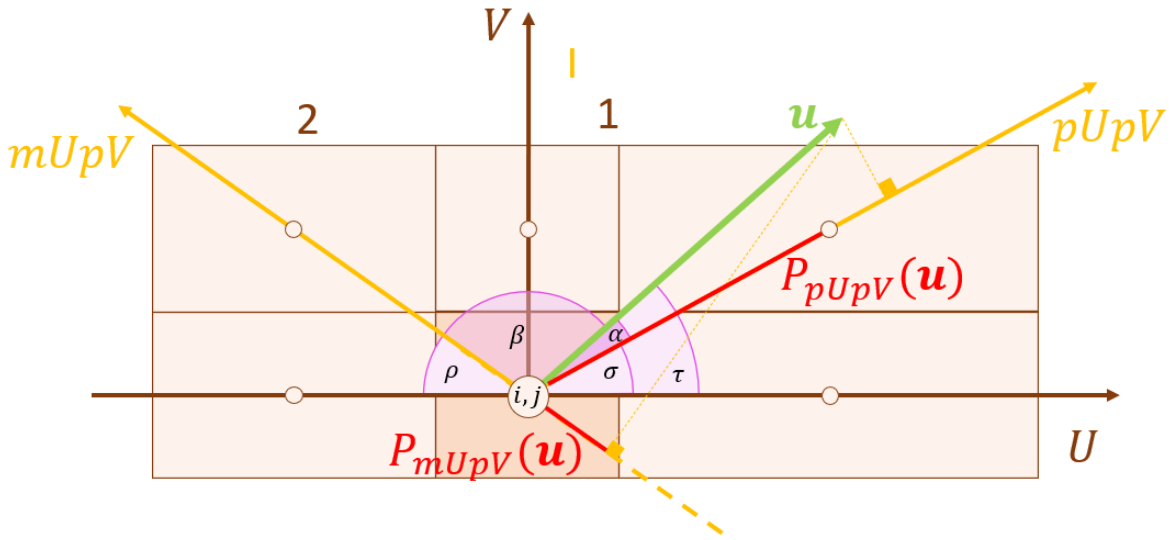

Figure 3.9: A schematic representation of wind projected onto diagonals, with β larger than $\frac{\pi}{2}$.

to project onto, whether α or β is needed to compute this direction and if this direction is positive or negative. The different formulas are summarized in Appendix B, in Table B.1. The first two columns show which projections are needed, and how these can be computed using α and β. Projection 1 is the projection onto either $pUpV$ or $mUmV$ and Projection 2 is the projection onto either $pUmV$ or $mUpV$. The last three columns then show how to compute τ, σ and ρ, which are used to compute α and β. This is always done using $\alpha = \tau - \sigma$ and $\beta = \pi - \tau - \rho$.

A final note that must be made on wind rotation. Due to the non-orthogonality of the diagonals, it is possible that β is larger than $\frac{\pi}{2}$. In this case, the projection is made onto the extension of the diagonal. This is shown in Figure 3.9 In this case, the projection $P_{mUpV}(\mathbf{u})$ would need to use $-\cos(\pi - \beta)$. However, using trigonometric identities for reflection, it is given that this is the same as $\cos(\theta)$, so this requires no additional implementation work.

3.6.2. Computing the Divergence

In Equation 3.6, in Section 3.3, the formula for second order divergence is given, where both the diagonal and nearest neighbor divergence is included. This formula can not be simply reused in this setting, as the pixels vary in size.

First, the distance between the centers of two pixels is not the same distance as the across track size of a pixel, which is the information that is available. The diagonals give the same problem. The along track size does not vary in size, so in this direction, it does not matter if the distance between two centers is taken, or if the dimension of the pixel is used.

The central finite difference formula that is used for the nearest neighbor divergence, is actually the mean of the forward first order finite difference and the first order backward finite difference:

$$\nabla_n \mathbf{f}^n_{i,j} = \frac{f^u_{(i+1,j)} - f^u_{(i-1,j)}}{2\Delta x} + \frac{f^v_{(i,j+1)} - f^v_{(i,j-1)}}{2\Delta y} \tag{3.24}$$

$$= \frac{1}{2}\left(\frac{f^u_{(i+1,j)} - f^u_{(i,j)}}{\Delta x} + \frac{f^u_{(i,j)} - f^u_{(i-1,j)}}{\Delta x}\right) + \frac{1}{2}\left(\frac{f^v_{(i,j+1)} - f^v_{(i,j)}}{\Delta y} + \frac{f^v_{(i,j)} - f^v_{(i,j-1)}}{\Delta y}\right) \tag{3.25}$$

In the forward difference term, Δx and Δy represent the distance between the center of the central pixel and the center of the pixel to the right and above respectively. For the backward difference term, Δx and Δy represent the distance between the center of the central pixel and the pixel to the right and below. However, in both instances of Δx, this coincides with the across pixel length and in both instances of Δy, this coincides with the along pixel length. Therefore, the equation can be simplified to the first form. Similarly, the diagonal delta's all have the same length, so a simplified version of the

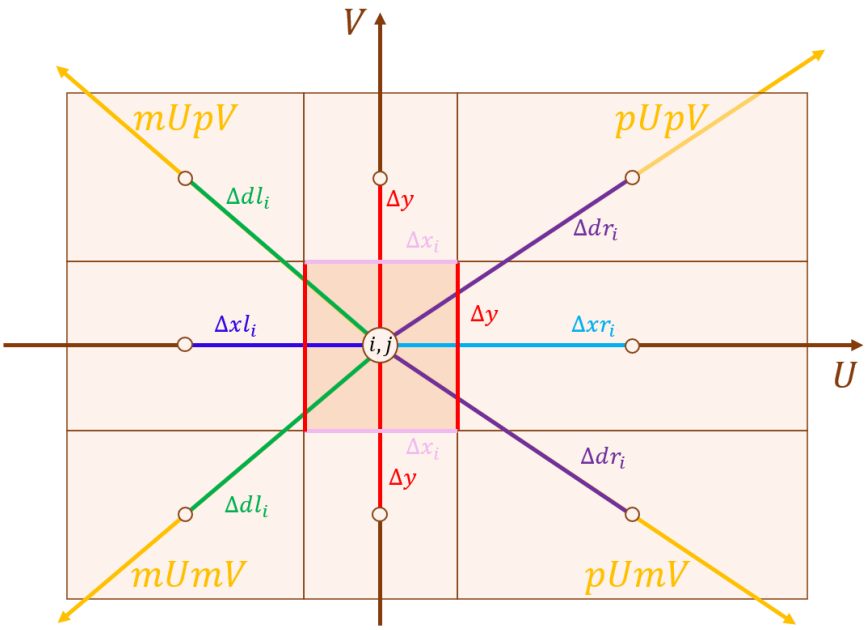

Figure 3.10: A schematic representation of the different lengths between centers of TROPOMI pixels.

formula can also be used.

However, in the case of TROPOMI pixels, only the along pixel length stays the same. Moreover, the dimensions of the pixels no longer coincide with the distances between centers of pixels. This is further illustrated in Figure 3.10 It can be seen that only in along track direction, Δy remains constant. However, a distinction must be made between Δx on the right and Δx on the left. These will now be named Δxr and Δxl. The same distinction is made for the diagonal dimensions Δdl and Δdr. These values differ for each pixel. The following formulas are then used to compute these values:

$$\Delta xr_i = \frac{1}{2}(\Delta x_{i+1} + \Delta x_i) \tag{3.26}$$

$$\Delta xl_i = \frac{1}{2}(\Delta x_{i+1} + \Delta x_i) \tag{3.27}$$

$$\Delta dr_i = \sqrt{\Delta x_r^2 + \Delta y^2} \tag{3.28}$$

$$\Delta dl_i = \sqrt{\Delta x_l^2 + \Delta y^2} \tag{3.29}$$

Here, the subscripts of Δx indicate the exact pixel of which the across track distance is used. This leads to the more complex form for the nearest and diagonal divergence:

$$\nabla_{2,n} \cdot \mathbf{f}_{(i,j)} = \frac{1}{2}\left(\frac{f^U_{(i+1,j)} - f^U_{(i,j)}}{\Delta xr_i} + \frac{f^U_{(i,j)} - f^U_{(i-1,j)}}{\Delta xl_i}\right) + \frac{f^V_{(i,j+1)} - f^V_{(i,j-1)}}{2\Delta y} \tag{3.30}$$

$$\nabla_{2,d} \cdot \mathbf{f}_{(i,j)} = \frac{1}{2}\left(\frac{f^{pUpV}_{(i+1,j+1)} - f^{pUpV}_{(i,j)}}{\Delta dr_i} + \frac{f^{pUpV}_{(i,j)} - f^{pUpV}_{(i-1,j-1)}}{\Delta dl_i}\right) + \frac{1}{2}\left(\frac{f^{mUpV}_{(i-1,j+1)} - f^{mUpV}_{(i,j)}}{\Delta dl_i} + \frac{f^{mUpV}_{(i,j)} - f^{mUpV}_{(i+1,j-1)}}{\Delta dr_i}\right) \tag{3.31}$$

$$\nabla \cdot \mathbf{f}_{(i,j)} = \frac{1}{2}(\nabla_{2,n} \cdot \mathbf{f}_{(i,j)} + \nabla_{2,d} \cdot \mathbf{f}_{(i,j)}) \tag{3.32}$$

The second order central difference using both nearest and diagonal neighbors is implemented, but an option is also used that allows us to select only the diagonal neighbors, or only the nearest neighbors. This gives rise to three adaptations, one using only the diagonal neighbors to compute the divergence (TROPD), one using only nearest neighbors (TROPN) and one using all surrounding neighbors (TROPDN).

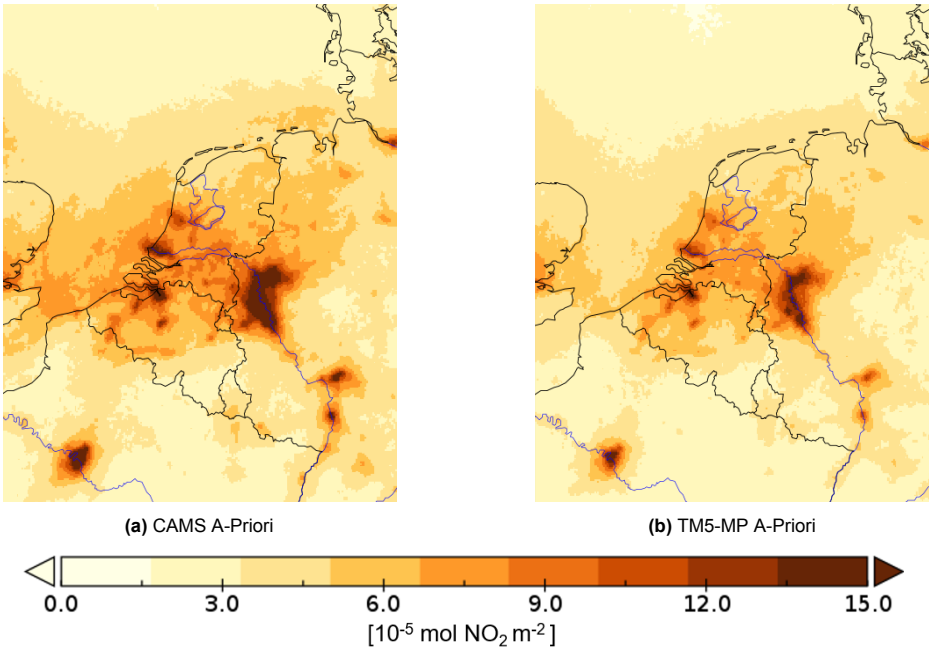

(a) CAMS A-Priori **(b)** TM5-MP A-Priori

Figure 3.11: This figure shows the NO_2 tropospheric column, gridded to a regular lat-lon grid with a 2.5x2.5 km resolution, and averaged over three months (Jun 2019 to August 2019). Figure 3.11a shows the tropospheric column using the CAMS a-priori product, and 3.11b shows the tropospheric column using the original TM5-MP tropospheric column.

3.7. A-priori Information

As explained before in Section 2.2.1, the chosen retrieval a-priori NO_2 vertical profile plays a vital role in determining the tropospheric column of NO_2. This research compares two a-priori profiles: the CAMS a-priori and the TM5-MP a-priori. This comparison has been made previously, including a paper describing the comparison between TROPOMI NO_2 observations and ground-based measurements in Helsinki [45], and a paper that presented a new TROPOMI product, where the TM5-MP a-priori profile is replaced by the CAMS a-priori profile [74].

The baseline scenario uses the CAMS a-priori, as both papers mentioned above reported that this data set has a smaller bias when compared to ground-based observations. As an experiment, the original TM5-MP a-priori is used. Figure 3.11 plots the NO_2 tropospheric column, averaged over three months. Figure 3.11a shows the result when using the CAMS a-priori, and Figure 3.11b uses the TM5-MP a-priori. It is clear that the CAMS a-priori yields higher NO_2 concentrations. Therefore, it is expected that applying the Flux-Divergence method using the TM5-MP a-priori profile will yield lower emissions.

Separate VCD data sets using both a-priori distribution are available as part of the TROPOMI product. Therefore, implementation of this experiment was trivial.

To conclude, this section introduces one new experiment, using a different NO_2 vertical profile a-priori. The experiment is henceforth referred to as DAP.

3.8. Estimating Emissions - Sink Term

The focus of the previous sections in this chapter have shown different possible alterations to the computation of the divergence of NO_2 flux. The final product that of interest is an emission map. This section discusses how this map is made, and how the choice of different parameters can influence the final result.

As described in the central paper of Beirle et al. [1], the NO_2 emission term (or source) is the sum of the sink term and the NO_2 flux-divergence. The crux of this section is thus estimating the sink.

At the TROPOMI overpass time, the largest cause of NO_2 loss is the chemical reaction of NO_2 with hydroxide (OH), which forms nitric acid (HNO_3) [68]. A time constant τ is used to model this, which describes the expected life time for a NO_2 molecule to be present in the atmosphere before having reacted with hydroxide.

A complication that should be addressed, is the fact that, at lower altitudes, NO_2 is photodissociated into NO and O. Conversely, NO and O_3 react to form NO_2 and O_2. Therefore, instead of computing NO_2 emissions, we calculate NO_x emissions, as both chemicals are so closely linked. The final emission term is thus multiplied with a conversion factor m, which is the fraction of NO_x to NO_2. This gives the following equation for the emission term:

$$E = m \cdot (\nabla \cdot \mathbf{f} + \frac{V_{NO_2}}{\tau}) \tag{3.33}$$

Different ways to choose m and τ are discussed in this section.

3.8.1. Constant values

Beirle et al. reported on values for m and τ, calculated by analysing plume formation from power plants in Riyadh [69]. For m they found a value of 1.32, with an error margin of 20%. For τ, they found 4 hours, with an error margin of 35%. First emission maps are made using these values of m and τ. However, this is not optimal, as lifetime of NO_2 depends on many factors, most notably the temperature, and the amount of OH and NO_2 present. The experiments using this fixed lifetime of 4 hours are referred to as EMISB.

3.8.2. Optimized constant values

Another approach in choosing τ and m, is optimizing them in such a way that they match expected values for emissions. On the one hand, we want emissions in low-emission regions to be minimized. As m is simply a scaling factor, this requirement can not be used to optimize m, as the optimal value is achieved by choosing m as small as possible. However, this requirement can be used to optimize τ.

This is done by selecting a lightly-trafficked part of the North Sea and computing the total emissions in this region. As the Flux-Divergence method does not exclude negative emissions, it is necessary to minimize the sum of the absolute value of the emissions in this region.

The CAMS emission inventory (Section 2.3.1) gives us an expected value for emissions for certain point sources of NO_2. Therefore, this data set can be used to optimize m in such a way that the difference in emission values for certain point sources is minimized when comparing the reported values of the Flux-Divergence method and the CAMS inventory. As point sources, seven different emitters were chosen that are visible on the scale of computation used in this research: Tata Steel, Rotterdam, Antwerp, Paris, the Ruhr area, Hamburg and Rouen (included to also have a smaller point source). A surrounding region is selected for each point source, in such a way that any smearing as a result of the implementation of the method is taken into account. The experiments using this optimized lifetime are further referred to as EMISBO.

3.8.3. Using DECSO lifetimes

As discussed in Section 2.3.2, one of the output data sets of the DECSO emission retrieval method is the lifetime of NO_2. It is used to minimize differences in VCDs between the DECSO output and the chemical transport model that is central to the method. As mentioned in the Theoretical Background, not much research is available on the validity of these values. However, it does display the expected seasonal patterns, with higher lifetimes in winter and lower lifetimes in summer. This can also be seen in Figure 3.12.

The DECSO data set provides monthly data values for τ. As the research time span is three months, from June 2019 until August 2019, the DECSO data set is averaged over these months. It is then linearly interpolated to the regular grid. The experiments using DECSO are further referred to as EMISD.

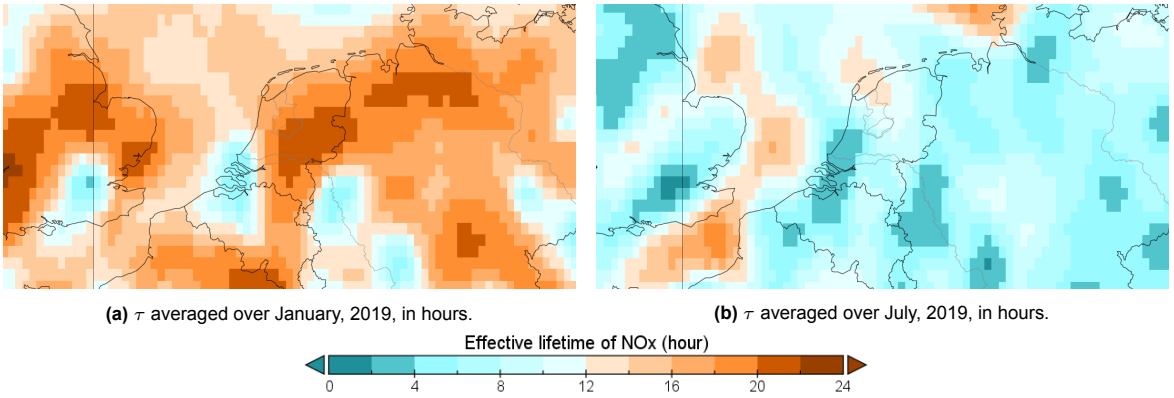

(a) τ averaged over January, 2019, in hours. **(b)** τ averaged over July, 2019, in hours.

Figure 3.12: The lifetime τ of NO_x, retrieved from the DECSO algorithm, in hours. Comparing both figures shows the higher NO_x lifetimes in the winter, as compared to the summer.

3.9. Metrics to Quantify Results Flux-Divergence Maps

Defining whether or not a certain experiment provides an improvement to the baseline scenario of the Flux-Divergence method is not straightforward. One of the main points of attention is that noise is reduced. However, it is also important that this noise reduction is not caused by a bias in the method, leading to an overall reduction of divergence, and consequently also in emissions. Several metrics are used to analyse the consequence of each alteration to the baseline scenario, which will be described in this section.

3.9.1. Total emissions

One metric used is the total amount of emissions (TE) over the entire domain. It is important that there is no severe decline or increase in the total amount of emissions, as this would indicate a possible bias in the alteration. Based on the work described in Section 3.8.1, a constant value of 4 hours was chosen for τ, and a constant value of 1.32 was chosen for m. The unit of NO_2 emissions is mol/m2/s. The area of each grid cell is computed, multiplied with the emission value of the grid cell, and these are summed over the entire domain, leading to a unit of mol/s.

3.9.2. Standard deviation

The TE of an experiment is not enough to adequately quantify its performance, as it is possible that an increase in noise does not change the emissions. Therefore, a second statistic is used to compare methods: the standard deviation of the divergence in a low emissions region (SDN). Ideally, this standard deviation should be very low. It was chosen to compute the standard deviation of the divergence instead of the emission, as an exact indication of emission is hard to give. The selected low emission region is the Ardennes, also extending into Northern France. To be more exact, the region chosen is the region between the longitudes 3.72 and 5.64 degrees East and 49.66 and 50.14 degrees North. It is assumed that any divergence here is noise, and so the standard deviation is ideally as low as possible. This assumption is debatable, considering it is possible that nearby sources of NO_2, such as Paris, may cause some deposition. Therefore, the mean divergence here should be at most slightly negative. This is indeed the case for each method. It is important to consult this value in combination with the TE value, as a reduction in noise can also be caused by a bias in the method, which will also lead to lower emissions values.

3.9.3. Scatterplots

Finally, scatter plots are a useful tool to provide more insight into the impact of each adaptation of the baseline scenario. For each pixel, the baseline flux-divergence is scattered against the flux-divergence value acquired by the adaptation. This scatterplot is then fitted using a Theil-Sen regressor.

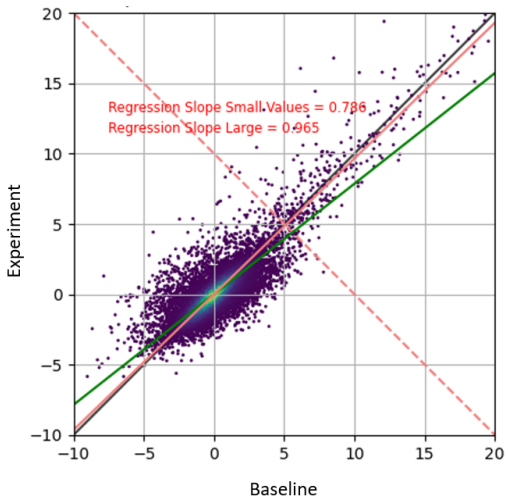

Figure 3.13: An example of a scatterplot used in this research. The baseline flux-divergence values are on the x-axis, and the flux-divergence values of the modification to the baseline scenario are on the y-axis. The green line represents the Theil-Sen regressor for small values. The red solid line represents the Theil-Sen regressor for large values. The red dotted line represents the separation between large and small values.

The Theil-Sen regressor was first introduced in 1950 [75]. The concept is simple: the slope between each pair of points is computed, and the median of these slopes is then taken as the regression slope. The intercept is determined using the median slope, passing it through each observation, and then again taking the mean of all resulting intercepts. An addition was made later by Sen, extending the case to situations where multiple observations have the same value on the x-axis [76]. This regressor was chosen as it is robust, symmetric, and hardly influenced by outliers. Especially the symmetric quality is an advantage in this setting, as both data sets do not necessarily represent the truth. Regressors such as the well-known least squares regressor use one of the variables as the truth scenario, and are thus not symmetric.

Two regressions were performed on each scatter plot. One regressor was fitted on the smaller divergence values (all values that meet the constraint [baseline value < - altered value +10]), and one on the larger divergence values (all other values). An example of this is shown in Figure 3.13. This separation was used, as the previous analysis on the low emission region indicated that most noise falls within the smaller divergence values. This distinction allowed for a separate analysis on large emitters and noise. Ideally, the slope of the regression line of the smaller values (RSS) should fall below 1, as this indicates a decline in noise. On the other hand, the regression line of the larger values (RSL) should be larger than the RSS value, and preferably near 1. This indicates that large emissions are maintained, and the reduction in noise is not caused by some bias in the method. However, an RSL value that is a bit smaller than 1, does not necessarily indicate that a part of the emission is lost. It is possible that a method leads to emission peaks that are more spread out over a region, but do not lead to lower emission values. Therefore, this statistic should also always be consulted in combination with the other statistics provided.

3.10. Validating Results for Emission Maps

The previous section elaborated on the different ways that the quality of flux-divergence maps are quantified for different experiments. This section does the same, but for emissions maps. The focus for emission maps is less focused on noise quantification, as most noise is introduced by the flux-divergence map. The other source of noise is the VCD, but as the different choices made for the emission experiments do no impact this map, noise will not vary much.

The main focus is whether the emission maps meet the expectations in terms of emission rates. This entails three factors. The first factor is how high emission is in regions where we do not expect much

emissions. The second factor is whether the emission rates of different point sources match reported emission rates of validated inventories. The final factor is how well the overall emission distribution matches the emission distribution of validated inventories.

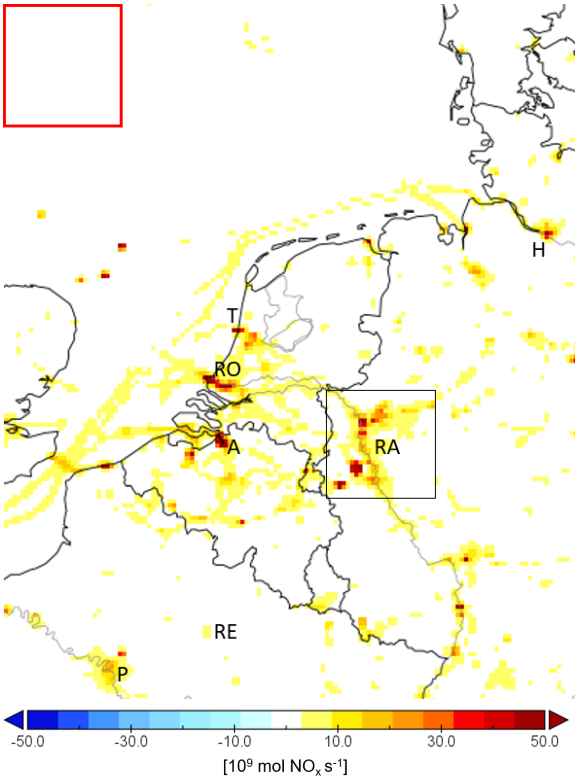

Figure 3.14: Reported NO_x emissions from the CAMS-REG emission inventory for 2017. The red square denotes the chosen low-emission region used to validate the results of the different emission experiments. Point sources used to compare emission inventories are also indicated: Tata Steel (T), Rotterdam (RO), Ruhr area (RA, also marked with black square), Hamburg (H), Antwerp (A), Reims (RE) and Paris (P).

Two inventories are used to validate the results: the DECSO method (which incorporates TROPOMI data) and the CAMS-REG emission inventory (which uses a bottom-up approach to compute emissions). We interpolate both emission inventories linearly to the regular grid and convert the data sets so the units match. The CAMS has yearly emission data bases, but unfortunately not for 2019. The closest year available is 2017. This is the data set we use. For the DECSO data set, the reported emissions are available on a daily basis, and thus require averaging from June 2019 to August 2019 (the time frame for which the emission maps using the Flux-Divergence method were created).

Emission in low-emission region

After analysing the emission map of the CAMS-REG emissions inventory, a low-emission zone above the North-Sea is selected as validation region. This region is shown in Figure 3.14, in red. Emissions are summed over this region. An overestimation of the lifetime of NO_2 can lead to negative emission, which should not be favored. Therefore, the absolute value of emissions is taken.

Emissions from point sources

A second metric chosen to validate the emission maps, is analysing the emissions for NO_x point sources. The selected point sources are: Tata Steel, Rotterdam (including the harbour region), Antwerp (including the harbor region), Paris, the Ruhr area, Hamburg and Rouen (a smaller city in Northern France). For each region, a larger surrounding area is chosen to account for possible smearing effects for any of the methods. All emissions within this area are summed and weighted with the corresponding area of the grid cell to find the total emissions of the point source.

Overall emission distribution

To quantify the overall emission distribution of the Flux-Divergence emission map, the Pearson correlation coefficient is used. Each grid cell is taken as a separate data entry, with one value from the Flux-Divergence emission map, and one value from the validation emission inventory.The formula for the correlation coefficient r is then given by:

$$r = \frac{\sum_{i=1}^{n} f_i v_i - \sum_{i=1}^{n} f_i \sum_{i=1}^{n} v_i}{\sqrt{n \sum_{i=1}^{n} {f_i}^2 - (\sum_{i=1}^{n} f_i)^2} \cdot \sqrt{n \sum_{i=1}^{n} {v_i}^2 - (\sum_{i=1}^{n} v_i)^2}}, \tag{3.34}$$

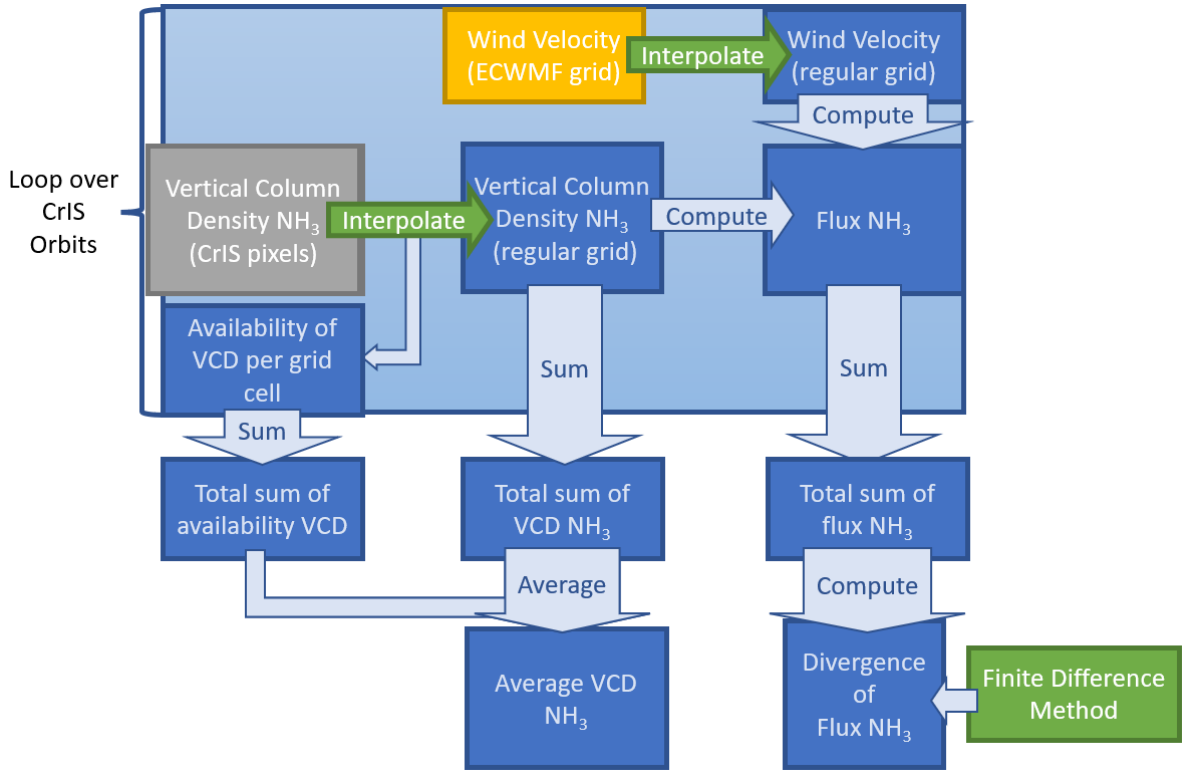

Figure 3.15: The structure of the code for the Flux-Divergence method as implemented for NH_3.

where n is the number of grid cells in the domain, f_i are the Flux-Divergence emission data points and v_i are the validation data set emission points. The correlation coefficient varies from -1 to 1. A negative correlation coefficient indicates an inverse relationship between the two data sets. The closer the correlation is to 1, the stronger the relationship is between both data sets [77].

3.11. Adaptations Flux-Divergence Method for Ammonia

Research question 1 of this thesis is focused on implementing and improving the Flux-Divergence method for NO_2 VCDs, from TROPOMI. However, we are also interested in whether or not the method can also be used for an atmospheric trace gas with very different characteristics, NH_3. This section will focus on how the method is adjusted to be able to implement it for ammonia VCDs. The largest part of the experiments was performed on data of the CrIS instrument (see also Section 2.2.2). Unfortunately, data from the CrIS instrument for the summer of 2019 is not available, as the CrIS instrument malfunctioned during this time. For this reason, data from the summer of 2016 has been used to perform the experiments.

The experiments are computed on two different resolutions: 10x10 km and 20x20 km. The resolution is chosen coarser than the experiments for TROPOMI, as previous emission retrieval methods for NH_3 were also performed a coarser grid (for example, the DECSO method). Moreover, ammonia is mostly emitted by the agricultural sector in the Netherlands. The emission points are therefore larger for NH_3 than for NO_x (an agricultural region instead of a company or industrial region).

3.11.1. Computing Divergence

The availability of satellite data for ammonia is much sparser than for nitrogen dioxide. This is mainly caused by the shape of the footprint of the CrIS instrument. It has a circular footprint. Therefore, computing the divergence on a single orbit is infeasible. For this reason, the divergence computation is taken outside of the orbit loop, and done on the averaged NO_2 flux. This code structure is shown in

Figure 3.15.

Given the seasonality in ammonia emissions, the averaging time must be chosen with care. Therefore, the first experiment analyses the impact of choosing different averaging times: 1 month (June 2019), 3 months (June-August 2019) and 5 months (May-August 2019). These experiments are referred to as NH3TIME1, NH3TIME3 and NH3TIME5.

It is also possible to compute the divergence multiple times after averaging over a certain amount of time, and then averaging the divergence. For this experiment, data from the summers of 2015, 2016, 2017 and 2018 is used. The averaging is done in two ways: yearly and monthly. In other words, the yearly experiment computes the divergence after averaging the VCDs from all orbits from the summer of a certain year. This is done four times (for 2015, 2016, 2017 and 2018). These four data sets are then averaged again, to find the final divergence. The monthly experiment averages all VCD data for the months June, July and August of the years 2015-2018 separately. This leads to three averages on which the divergence is computed, and again averaged. These experiments are referred to as NH3YEARAVG and NH3MONTHAVG.

This chapter introduced multiple experiments. These are presented in an overview in the following tables. All experiments that focus on the computation of the flux-divergence map for NO_x are shown in Table 3.2. The experiments that compute emission maps for NO_x are shown in Table 3.3. Finally, the experiments that focus on NH_3 are shown in Table 3.4. The next chapter provides the results for these experiments.

Name	Resolution	A-Priori	FDM	Wind Data	Computation Grid	Section
BASE-5	5x5 km	CAMS	$D = \frac{1}{2}\nabla_{2,n} \cdot \mathbf{f}^n + \frac{1}{2}\nabla_{2,d} \cdot \mathbf{f}^d$	Wind Half-PBL	Regular grid	3.2
BASE-2.5	2.5x2.5 km	CAMS	$D = \frac{1}{2}\nabla_{2,n} \cdot \mathbf{f}^n + \frac{1}{2}\nabla_{2,d} \cdot \mathbf{f}^d$	Wind Half-PBL	Regular grid	3.2
DIVSON-5	5x5 km	CAMS	$D = \nabla_{2,n} \cdot \mathbf{f}^n$	Wind Half-PBL	Regular grid	3.3
DIVSON-2.5	2.5x2.5 km	CAMS	$D = \nabla_{2,n} \cdot \mathbf{f}^n$	Wind Half-PBL	Regular grid	3.3
DIVFON-5	5x5 km	CAMS	$D = \nabla_{4,n} \cdot \mathbf{f}^n$	Wind Half-PBL	Regular grid	3.3
DIVFON-2.5	2.5x2.5 km	CAMS	$D = \nabla_{4,n} \cdot \mathbf{f}^n$	Wind Half-PBL	Regular grid	3.3
WINDMEAN-5	5x5 km	CAMS	$D = \frac{1}{2}\nabla_{2,n} \cdot \mathbf{f}^n + \frac{1}{2}\nabla_{2,d} \cdot \mathbf{f}^d$	Wind Mean of PBL	Regular grid	3.4
WINDMEAN-2.5	2.5x2.5 km	CAMS	$D = \frac{1}{2}\nabla_{2,n} \cdot \mathbf{f}^n + \frac{1}{2}\nabla_{2,d} \cdot \mathbf{f}^d$	Wind Mean of PBL	Regular grid	3.4
WINDDIV-5	5x5 km	CAMS	$D = \frac{1}{2}\nabla_{2,n} \cdot \mathbf{f}^n + \frac{1}{2}\nabla_{2,d} \cdot \mathbf{f}^d$	Wind Half-PBL, reduced divergence	Regular grid	3.4
WINDDIV-2.5	2.5x2.5 km	CAMS	$D = \frac{1}{2}\nabla_{2,n} \cdot \mathbf{f}^n + \frac{1}{2}\nabla_{2,d} \cdot \mathbf{f}^d$	Wind Half-PBL, reduced divergence	Regular grid	3.4
SAVG	5x5 km	CAMS	$D = \frac{1}{2}\nabla_{2,n} \cdot \mathbf{f}^n + \frac{1}{2}\nabla_{2,d} \cdot \mathbf{f}^d$	Wind Mean of PBL	Regular grid, interpolated from 2.5x2.5 km to 5x5 km resolution	3.5
TROPDN-5	5x5 km	CAMS	$D = \frac{1}{2}\nabla_{2,n} \cdot \mathbf{f}^n + \frac{1}{2}\nabla_{2,d} \cdot \mathbf{f}^d$	Wind Half-PBL	TROPOMI grid	3.6
TROPDN-2.5	2.5x2.5 km	CAMS	$D = \frac{1}{2}\nabla_{2,n} \cdot \mathbf{f}^n + \frac{1}{2}\nabla_{2,d} \cdot \mathbf{f}^d$	Wind Half-PBL	TROPOMI grid	3.6
TROPD-5	5x5 km	CAMS	$D = \nabla_{2,d} \cdot \mathbf{f}^d$	Wind Half-PBL	TROPOMI grid	3.6
TROPD-2.5	2.5x2.5 km	CAMS	$D = \nabla_{2,d} \cdot \mathbf{f}^d$	Wind Half-PBL	TROPOMI grid	3.6
TROPN-5	5x5 km	CAMS	$D = \nabla_{2,n} \cdot \mathbf{f}^n$	Wind Half-PBL	TROPOMI grid	3.6
TROPN-2.5	2.5x2.5 km	CAMS	$D = \nabla_{2,n} \cdot \mathbf{f}^n$	Wind Half-PBL	TROPOMI grid	3.6
DAP-5	5x5 km	TM5-MP	$D = \frac{1}{2}\nabla_{2,n} \cdot \mathbf{f}^n + \frac{1}{2}\nabla_{2,d} \cdot \mathbf{f}^d$	Wind Half-PBL	Regular grid	3.7
DAP-2.5	2.5x2.5 km	TM5-MP	$D = \frac{1}{2}\nabla_{2,n} \cdot \mathbf{f}^n + \frac{1}{2}\nabla_{2,d} \cdot \mathbf{f}^d$	Wind Half-PBL	Regular grid	3.7

Table 3.2: A summary of the baseline extensions on the computation of the flux-divergence map for NO_2 presented in Sections 3.2 to 3.7.

Name	**Resolution**	**Computation of τ**	**Computation of m**
EMISB	5x5 km	4 hours	1.32
EMISO	5x5 km	Minimizes emissions in low-emission region	Optimized to match peak emissions from CAMS inventory
EMISD	5x5 km	Taken from DECSO model run	Optimized to match peak emissions from CAMS inventory

Table 3.3: A summary of the approaches for computing NO_x emissions presented in Section 3.8.

Name	**Resolution**	Satellite Instrument	**Timeframe**	**VCD averaged over**
NH3TIME1-*x*	10x10 km and 20x20 km	CrIS	June 2016	All Data
NH3TIME3-*x*	10x10 km and 20x20 km	CrIS	June-August 2016	All Data
NH3TIME5-*x*	10x10 km and 20x20 km	CrIS	April-August 2016	All Data
NH3YEARAVG-*x*	10x10 km and 20x20 km	CrIS	June-August 2015-2018	Each Year Separately
NH3MONTHAVG-*x*	10x10 km and 20x20 km	CrIS	June-August 2015-2018	Each Month Separately

Table 3.4: A summary of the approaches for computing NH_3 flux-divergence maps presented in Section 3.11. The x in the method name indicates the resolution on which the results are presented.

4

Results

Experiment name	Methodology	Results	Appendix
BASE	3.2	4.1	A.1
DIVSON/DIVFON	3.3	4.2	A.2
WINDDIV	3.4	4.3.1	A.3
WINDMEAN	3.4	4.3.2	A.4
SAVG	3.5	4.4	A.5
TROPD/TROPN/TROPDN	3.6	4.5	A.6
DAP	3.7	4.6	A.7
EMISB/EMISO/EMISD	3.8	4.7	A.8
NH3TIME	3.11	4.8.1	A.9
NH3MONTHAVG/NH3YEARAVG	3.11	4.8.2	A.10/A.11

Table 4.1: This table shows the section in which the used implementation and results can be found for each method. It also shows in which appendix the flux-divergence and emission maps can be found.

In this chapter, the results of all adaptations to the baseline Flux-Divergence method are discussed. In Table 4.1, an overview is provided of all experiments, and the section in which their implementation and results are discussed. It also shows the appendix in which the resulting flux-divergence or emission maps are located.

Research question 1a focuses on analyzing the impact of different choices for the flux-divergence map of NO_x. This is focused on in Sections 4.1 to 4.6. The metrics described in 3.9 are used to characterize the performance of each adaptation. The values found for these methods are summarized in Table 4.2.

Research question 1b is aimed at analyzing the impact of using different approaches to approximate a lifetime for NO_x. The results of these experiments are given in Section 4.7. The metrics used to quantify these results are given in Section 3.10. The values for this metrics are given in Table 4.3.

Finally, the results for the ammonia flux-divergence maps are presented in Section 4.8. This section answers research question 2.

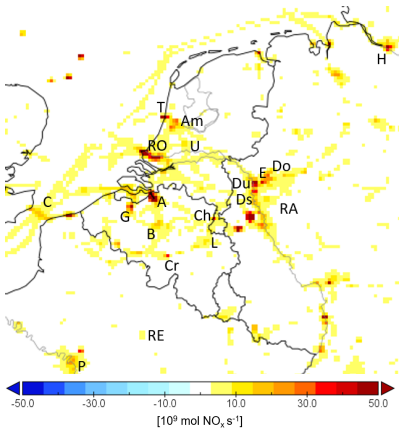

Figure 4.1: A map containing all locations mentioned in this chapter: Amsterdam (Am), Antwerp (A), Brussels (B), Chemelot (Ch), Charleroi (Cr), The Channel (C), Dortmund (Do), Düsseldorf (Ds), Duisburg (Du), Essen (E), Ghent (G), Hamburg (H), Liege (L), Paris(P), Ruhr Area (RA), Reims (RE), Rotterdam (RO), Tata Steel (T) and Utrecht (U).

Method	TE [10^{18} kmol/s]	SDN	RSS	RSL
BASE-2.5	2.50 kmol/s	1.142 (100%)	1	1
DAP-2.5	2.16 kmol/s	1.229* (107%)	0.829	0.775
DIVFON-2.5	2.49 kmol/s	1.611 (141%)	1.225	1.250
DIVSON-2.5	2.51 kmol/s	1.356 (119%)	1.085	1.103
TROPD-2.5	2.50 kmol/s	0.510 (45%)	0.223	0.730
TROPN-2.5	2.49 kmol/s	0.715 (63%)	0.440	0.825
TROPDN-2.5	2.49 kmol/s	0.535 (47%)	0.349	0.761
WINDDIV-2.5	2.49 kmol/s	1.088 (95%)	0.904	0.946
WINDMEAN-2.5	2.50 kmol/s	1.113 (97%)	0.959	0.963
BASE-5	2.51 kmol/s	0.523 (100%)	1	1
DAP-5	2.16 kmol/s	0.548* (104%)	0.778	0.702
DIVFON-5	2.46 kmol/s	0.775 (148%)	1.230	1.152
DIVSON-5	2.50 kmol/s	0.661 (126%)	1.091	1.058
SAVG	2.53 kmol/s	0.911 (174%)	1.205	1.169
TROPD-5	2.50 kmol/s	0.452 (86%)	0.676	0.926
TROPN-5	2.49 kmol/s	0.616 (118%)	0.927	1.016
TROPDN-5	2.49 kmol/s	0.490 (94%)	0.816	0.950
WINDDIV-5	2.48 kmol/s	0.527 (101%)	0.781	0.965
WINDMEAN-5	2.50 kmol/s	0.520 (99%)	0.961	0.976

Table 4.2: The reported metrics of all experiments on NO_2 flux-divergence maps. The metrics are the Total Emissions (TE), the Standard Deviation of Low-emission regions (SDN), the Theil-Sen Regression Slope for Small values (RSS) and the Theil-Sen Regression Slope for Large values (RSL). The values with an asterix (*) rescaled using TE. More information on the used metrics can be found in Section 3.9.

	EMISB	EMISO	EMISD	CAMS-REG	DECSO
PCC - CAMS	0.598	0.577	0.579	1	0.478
PCC - DECSO	0.820	0.730	0.854	0.478	1
Low-Emissions	7.59	0.47	0.46	0.29	N.A.
Emissions - Tata Steel	3.78	2.27	2.80	5.48	2.37
Emissions - Rotterdam	20.49	12.63	16.00	24.47	12.80
Emissions - Antwerp	24.30	16.76	23.61	18.63	16.23
Emissions - Ruhr area	178.85	99.15	156.16	97.88	125.61
Emissions - Paris	60.82	39.15	66.24	21.01	61.48
Emissions - Hamburg	15.34	11.02	16.74	10.10	10.67
Emissions - Reims	3.30	1.80	1.84	1.43	2.07

Table 4.3: The results of the metrics chosen to evaluate the NO_x emission maps (see Section 3.10). The emissions are given in 10^{18} mol/s. The PCC (Pearson's Correlation Coefficient) is dimensionless.

4.1. Baseline Method

This first result section discusses the output of the baseline Flux-Divergence method. This method was implemented at the KNMI by Henk Eskes prior to this research. All adjustments to this method that are included in this research paper will be compared to this setting.

Figure 4.2 shows the computed flux-divergence on a relatively coarse grid (5x5 km) and a more refined grid (2.5x2.5 km). The flux-divergence was averaged over three months, from June 1st 2019 until August 31st 2019. Both results show a spatial distribution that meets expectations, given the known NO_2 sources in the Netherlands.

Prominent industrial zones light up: Tata Steel, the Ruhr Area in Germany, and the harbours of Rotterdam, Hamburg and Antwerp. Some smaller industrial zones are also visible, including Chemelot in Dutch Limburg, and the area of Charleroi in Belgium.

Flux-divergence from transport is also visible on the map, most evidently the heavily trafficked North Sea along the coast of the Netherlands, Belgium and The Channel. Some effects from land transport are also visible, such as the highway connecting Utrecht and Amsterdam. Heavily trafficked city centers are also discernible, such as Brussels, Liège, Utrecht, Paris and Ghent.

Comparing the two resolutions gives a good insight in the advantages of a coarse grid and a fine grid. The coarse grid gives a good representation of the spatial distribution and, more importantly, shows less noise that the fine grid, making it easier to find flux-divergence hot spots that are slightly less easy to discern. This observation is reflected in the SDN, as shown in Table 4.2. The SDN is a lot lower for all experiments performed on the coarse grid than the SDN of the experiments performed on a fine grid. On the other hand, the fine grid does give a better refining of the location of flux-divergence. A clear example of this is the Northern hot spot in the Ruhr Area. On the coarse grid, this is condensed to one point source, but examining the finer grid shows multiple peaks within the hot spot, which correspond to the several cities within this region: Duisburg, Dortmund, Essen and Düsseldorf.

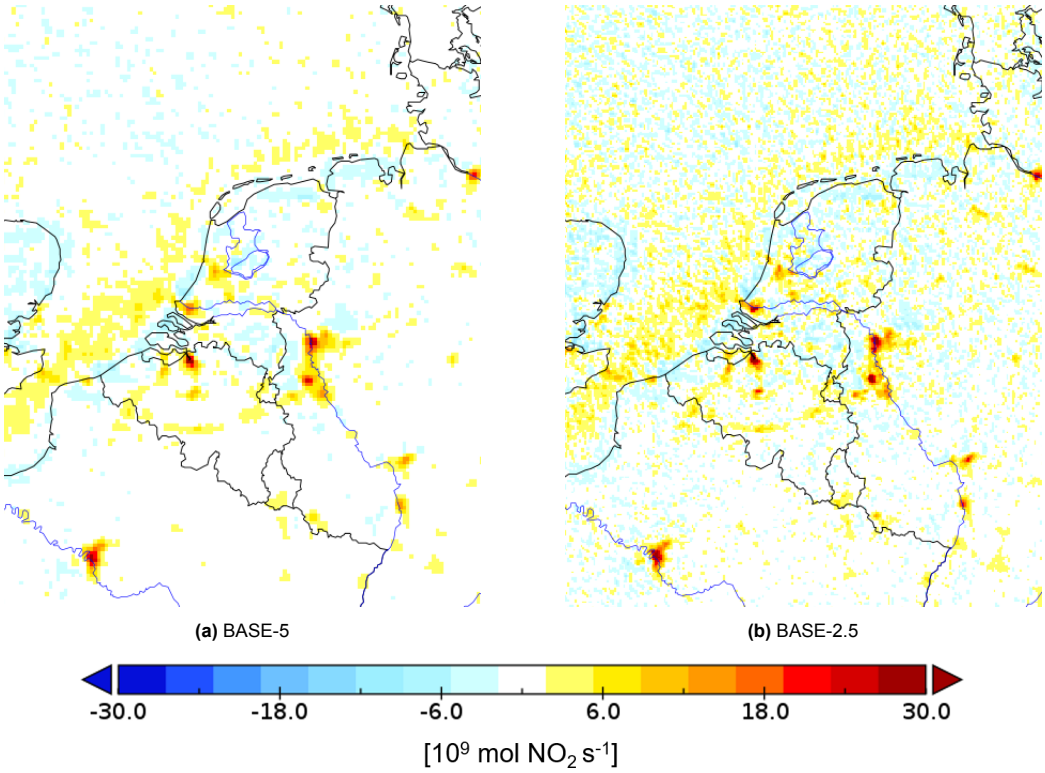

Figure 4.2: The flux-divergence map of running the baseline models, on a 5x5 km resolution (left) and a 2.5x2.5 km resolution (right).

4.2. Finite difference method

The current baseline method computes the divergence using a second order finite difference method, including diagonal neighbors and nearest neighbors. As described in Section 3.3, two alternatives have been implemented to the method. The first one uses only the nearest neighbors to compute the divergence (DIVSON), and the second one uses a fourth order finite difference method including the second neighbors (DIVFON).

4.2.1. Second Order Nearest neighbors (DIVSON)

Consulting Table 4.2 shows that this adaptation does not significantly change the total emissions. However, it does increase the amount of noise on the image, which is reflected in the SDN and the RSS. All maps and scatterplots for the DIVSON experiment can be found in Appendix A.2, in Figure A.2.

On the fine resolution grid, shown in Figure A.3b, the SDN increases with 19%. This increase in noise is visible above Northern France, and is also reflected in the RSS. Moreover, the RSL is larger than 1 for the fine resolution, meaning the emission points also increase along with the noise. The maps show slightly emission peaks with slightly clearer borders, although this is hardly visible. This result is most clear above Amsterdam, where two hot spots can be discerned, instead of one.

For the coarse resolution, the increase in SDN is even larger (26%). Given the relative lower noise-level of the coarse grid, this increase is better visible than for the fine resolution. The results for the coarse resolution are shown in Figure 4.3. Interestingly, the RSL is somewhat lower than the RSS, albeit still higher than 1. This was not the case for the fine resolution model. Looking at the map, the emission hot spots are slightly more well-defined than for the baseline scenario. This is especially clear in the Ruhr area.

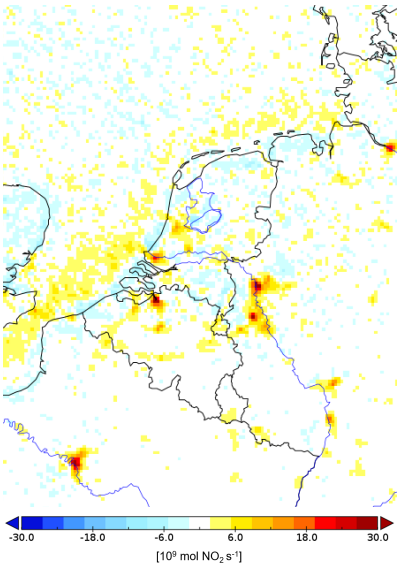

Figure 4.3: The flux-divergence map for DIVSON-5

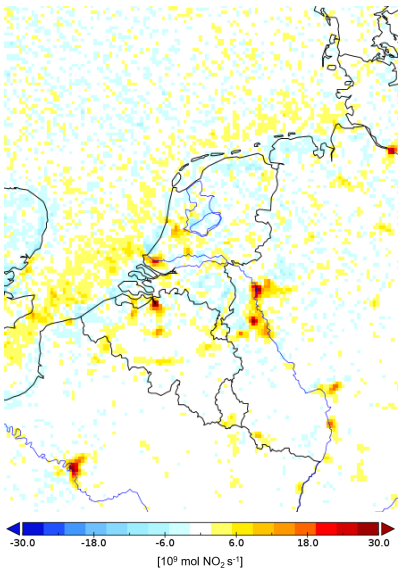

Figure 4.4: The flux-divergence map for DIVFON-5

In conclusion, using only nearest neighbors to compute the second order central divergence introduces noise, and is therefore not an improvement to the Flux-Divergence method, although it does better refine the emission hot spots.

4.2.2. Fourth Order Finite Difference (DIVFON)

The results of the DIVFON experiments mirror the results of the DIVSON experiment, although the increase in noise is more profound. The flux-divergence maps and scatterplots for DIVFON can be found in Appendix A.2, in Figure A.3.

On the fine resolution grid, the SDN increases by 41%. The map of this experiment is shown in Figure A.3b. Accompanied by an RSS value of 1.225, this indicates that the noise increases significantly in comparison to the baseline scenario. This is confirmed by the flux-divergence map, where low-emission regions like the North of France now consist almost entirely of noise. The RSL increases as well, shown in the map by more well-defined point sources. However, smaller cities like Reims are now indiscernible from the noisy background.

Figure 4.4 shows the flux-divergence map on the coarse grid for the DIVFON experiment. The noise increase for the coarse

resolution is 48%, which is even larger than for the fine grid. It is also larger than the coarse results of the DIVSON experiment. This is also seen when comparing Figure 4.3 and 4.4. Again, the RSL is slightly lower than the RSS. The emission sources are more detailed than in the baseline scenario.

In conclusion, DIVFON introduces even more noise than DIVSON, and is therefore not considered to be an improvement to the baseline scenario in the setting of this research. The Flux-Divergence method is moderately sensitive to the finite difference method used to compute the divergence.

4.3. Wind Dataset

Two new data sets of the wind have been used as an adaptation to the baseline scenario, leading to the WINDDIV and WINDMEAN experiments. The results for these experiments are described in this section. All WINDDIV maps can be found in Appendix A.3. All WINDMEAN maps are included in Appendix A.4.

4.3.1. WINDDIV

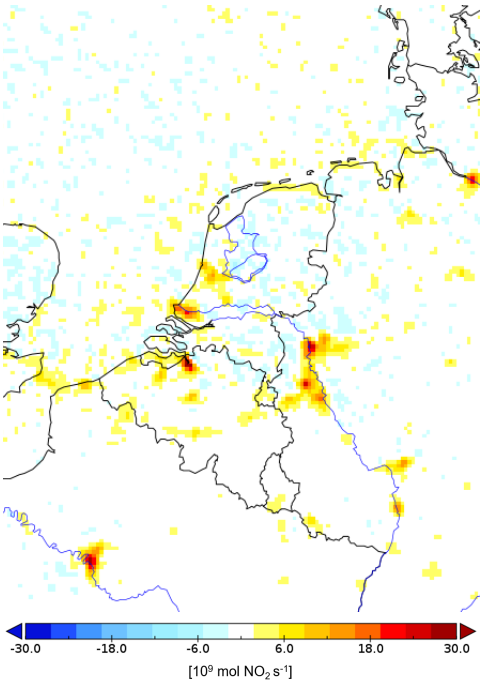

Figure 4.5: The flux-divergence map for WINDDIV-5

Figure 4.5 shows the results for the WINDDIV experiment on the coarse resolution grid. The most interesting result is the distribution of the flux-divergence along the coast. The flux-divergence within regions with previously high wind divergence has almost disappeared. There are still a few emission hot spots above the sea, such as the Channel route from Calais to Dover. The regions with negative flux along the coast have also been reduced, most notably along the French coast. These regions lie in regions with strong negative divergence in the wind. Peak emitters within these regions, most notably Tata Steel and the port of Rotterdam, are better visible in the WINDDIV setting. The same effect is present in the high-resolution maps, but the higher noise levels caused by the computation of divergence on this scale makes the effect harder to discern.

Figure 4.5 also shows that using this divergence-free data set does not influence the inland NO_2 emission hot spots. They are still distributed in the same way, and seem to have the same intensity. This is confirmed in Table 4.2, which shows that the total emission rate is almost the same, compared to the baseline scenario. The RSL is slightly lower than 1 for both resolutions. Figure 4.6 also shows that the highest emission values lie along the x=y line for the coarse resolution, which confirms this observation.

The level of noise does not alter much for most regions when compared to the baseline. The SDN hardly changes for the coarse resolution, and diminishes only slightly for the fine resolution. However, Figure 4.6 shows regression lines that indicate an improvement to the baseline scenario on the coarse grid. The regression line for large values is close to the x=y line, meaning emissions are not lost. Conversely, the regression line for small values is significantly less steep, meaning noise is reduced. As the value of the flux-divergence along the North Sea coast lies partially within the chosen noise boundary, it is well possible that this reduction in RSS is caused by the decline in this flux-divergence along the coast. This means that the overall noise levels do not necessarily change significantly. For the fine resolution, the reduction in RSS is much less, perhaps also because the effect of the WINDDIV experiment is less strong for this resolution.

In conclusion, the WINDDIV experiment markedly dampens both positive and negative flux-divergence values along the coast, which is the region where the divergence in wind flow is at its strongest. This improves the visibility of coastal emitters within regions with negative wind divergence, such as Tata Steel.

Inland emissions and overall noise are not significantly affected by this experiment, as the wind divergence here is low. The effect is most prominent on the coarse resolution maps. This experiment shows that the presence of divergence in wind data set has a large impact on the resulting flux-divergence map of NO_x.

4.3.2. WINDMEAN

In Section 3.4, it was already shown that averaging the ECMWF data set over the Planetary Boundary Layer (PBL) gave slightly lower wind velocity values than taking the wind velocity at the height halfway the PBL. The resulting flux-divergence maps hardly differ from one another, and the scatterplots are more or less on the x=y line. These maps are shown in Figure A.5. The metrics show a slight bias: both the RSS and RSL are slightly lower than 1, and the SDN has a slightly lower percentage than the baseline SDN. This bias is directly linked to the overall slight decline in wind velocities used for these maps. The differences are so small, that there is no decline in total emission (or hardly, in the case of the fine resolution grid). The Flux-Divergence method is thus hardly sensitive to the method used to summarize wind velocity within the PBL. This thesis suggests that both methods can be used interchangeably.

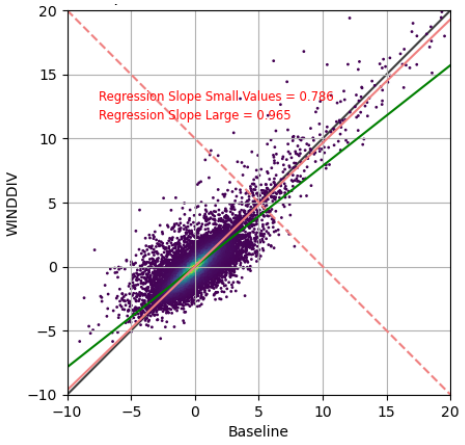

Figure 4.6: Scatterplot for WINDDIV-5

4.4. Spatial Averaging

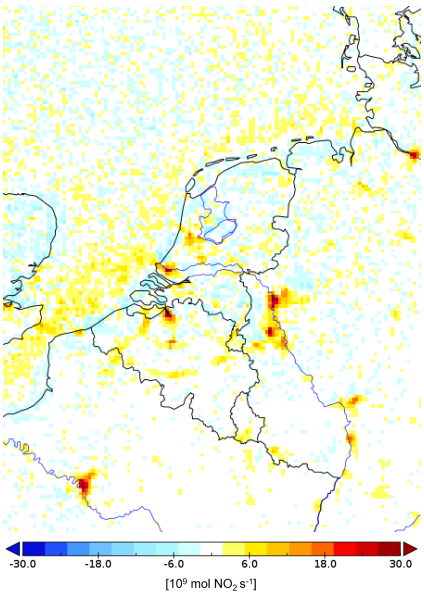

Figure 4.7: The flux-divergence map for SAVG.

This section discusses the result of spatially averaging the output of the baseline model run from a fine resolution grid to a coarse resolution grid. An explanation of this technique is given in Section 3.5. All figures for this experiment can be found in Appendix A.5.

Using this method has an overall poor influence on the output. The total emission does not change significantly, but the amount of noise does. This is clearly visible in Figure 4.7, which displays the flux-divergence map for this experiment. The SDN increases with 74%, and the RSS is well above 1.0.

One interesting improvement is the fact that the centers of hot spots become more well defined. Zooming in on the northern part of the Ruhr area shows this most clearly, where one large hot spot is separated into two, corresponding with the location of Duisburg and Düsseldorf. The RSL is above 1, but lower than the RSS. However, a regression slope does not properly capture more distinct emission sources, as a more well-defined emission source will contain some grid cells that are lower, and a few that are higher than the original, less well-defined emission source.

In conclusion, it is not recommended to use the spatial averaging approach in the context of this research, as it enhances noise considerably, although peak sources are also enhanced.

4.5. TROPOMI grid

As described in Section 3.6, it is possible to compute the flux and resulting divergence on the TROPOMI grid instead of on the regular grid. This reverses the order in which data is interpolated to the regular grid and the divergence is computed. The results of this approach will be shown in this section, describing three different experiments, TROPD, TROPN and TROPDN. Each method differs in which neighboring pixels were used when computing the flux-divergence. TROPD uses only diagonal neighbors, TROPN uses only nearest neighbors and TROPDN uses both. The method was implemented on two different grid resolutions: a fine grid of 2.5x2.5 km and a coarse grid of 5x5 km.

On the coarse grid, the SDN reduces for both TROPD and TROPDN, but increases for TROPN. However, all of the RSS values are lower than 1, indicating that these methods generally dampen the noise. The RSL is close to 1 for all three experiments, showing that emissions are not lost using this method. This is also reflected in the TE, as this is the same as for the baseline results. It is important to include the diagonal divergence, as this reduces the noise. The clearest example of this can be seen above the North Sea. All coarse grid flux-divergence maps are included in Appendix A.6, in Figure A.7. The scatterplots are shown in Figure A.9.

The noise reduction is even more clear when examining the method on the 2.5x2.5 km grid resolution. When including the diagonal flux, the SDN is halved. TROPN also leads to a significant noise reduction. The RSS values are all significantly smaller than any other method that has been used. However, the RSL values are also smaller than 1, especially for the methods including diagonal divergence. This could indicate that emission peaks are horizontally smeared, as the TE values show that emissions are not lost.

From Table 4.2, it would seem that using only diagonal divergence (TROPD) is beneficial, as it has the lowest SDN and RSS, whereas using only nearest neighbors (TROPN) has higher values for these metrics. However, it is still advisable to include all neighbors (TROPDN), as TROPD has less well-defined emission peaks. This is most evident when examining Rotterdam and Tata Steel. The centers of these peaks are hard to distinguish on the TROPD map, and are more clear on the TROPDN map. The results for TROPDN are shown in Figure 4.8. Here, we clearly see the noise reduction in comparison to the baseline map. The peak emitters are still clear on the TROPDN map, although they have somewhat less well-defined centers (a clear example of this is seen in Paris). All fine grid flux-divergence maps can be found in Appendix A.6, in Figure A.8, with the scatterplots included in Figure A.9.

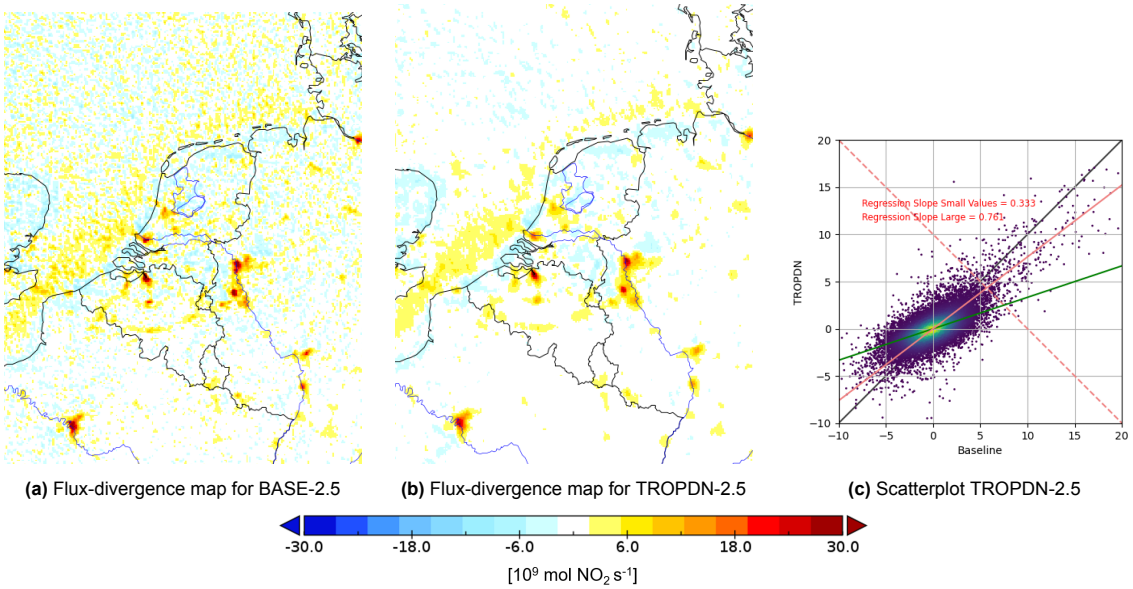

(a) Flux-divergence map for BASE-2.5 **(b)** Flux-divergence map for TROPDN-2.5 **(c)** Scatterplot TROPDN-2.5

Figure 4.8: The flux-divergence maps of the baseline scenario (a) and the result of the TROPDN experiment on a 2.5x2.5 km grid resolution (b), including the scatterplot of these results (c). The green line in the scatterplot is the Theil-Sen regressor for small values, and the red line is the Theil-Sen regressor for large values.

In conclusion, TROPN, TROPD and TROPDN all offer a significant improvement on the baseline scenario, especially when considering fine resolution maps. TROPDN is the preferred option of these three, as it significantly reduces the noise (more so than TROPN), while it maintains well-defined emission points (more than TROPD).

4.6. A-priori Information

In Section 3.11 it was described how a different a-priori choice for the NO_2 vertical column profile could be introduced in the implementation of the Flux-Divergence method. As described, the CAMS a-priori is used in the baseline scenario, which yields a higher overall NO_2 concentration than the TM5-MP a-priori. This last a-priori was used as an adaptation to the baseline. All figures for this experiment can be found in Appendix A.7.

As can be expected, this lower NO_2 concentration used in the Flux-Divergence method also leads to lower flux-divergence values. This bias is clear in every metric used to measure the performance of methods. The TE for this experiment is 86% of the TE of the baseline scenario, and the regression slopes of both the larger and smaller values are well below 1.0. What is interesting to note for both resolutions, is that the RSL is lower than the RSS, meaning that the decrease in flux-divergence in the hot spots is more prominent than the flux-divergence in the areas where noise predominates.

As the TE differs significantly for this method from the baseline TE, the SDN was scaled using the ratio between both TE values, to allow for a fair comparison with the baseline scenario. We note that for both resolutions, the scaled SDN value is slightly higher than the original SDN. In conclusion, using the TM5-MP a-priori does not benefit the Flux-Divergence method. This experiment also shows that the Flux-Divergence method is very sensitive for the a-priori vertical profiles used in the TROPOMI retrieval. The a-priori profiles should thus be carefully chosen when using the Flux-Divergence methods.

4.7. Emission Estimation

The previous sections of this chapter discussed the results of different alternatives proposed to the baseline method for creating the flux-divergence map. As explained in Section 3.8, the next step in the Flux-Divergence method is estimating a sink term for NO_2, in order to compute emissions. The focus is on the estimation of the lifetime for NO_2. The NO_2 emissions will also be converted to NO_x emissions, using a mixing ratio. This section discusses three different approaches in estimating the sink term: EMISB, EMISO and EMISD. Table 3.3 summarizes the differences between these methods.

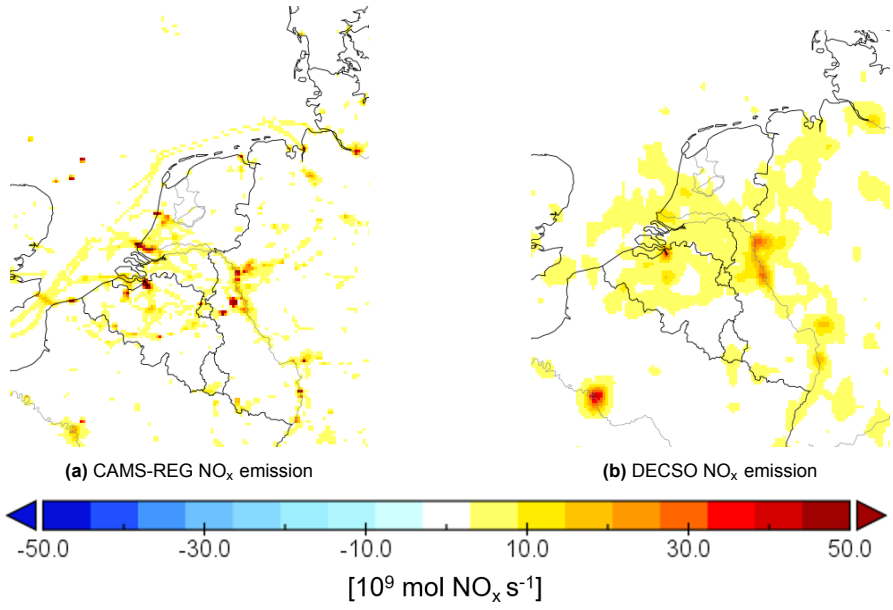

Figure 4.9: NO_x emissions from the two validation data sets used in the research, CAMS-REG and DECSO. Both have been interpolated to the regular grid, at a resolution of 5x5 km.

Section 3.10 discusses the metrics used to quantify the results of each approach. These metrics are summarized in Table 4.3. Two data sets are used to compare the results of this approach to: the CAMS-REG emission inventory (as presented in Section 2.3.1) and the DECSO algorithm results (see also Section 2.3.2). The metrics for these data sets are included in Table 4.3 as well.

Figure 4.9 shows the NO_x emissions for both validation data sets, interpolated to the regular grid. CAMS-REG is based on a bottom-up inventory, which is clear from the well-defined emission points, and continuous emissions lines from sea transport. DECSO uses satellite data to create emission maps, and shows a more smeared emission map. The correlation coefficient between these two data sets is 0.478, indicating a moderate correlation. For most coastal point sources (Tata Steel, Rotterdam and Antwerp), CAMS-REG reports higher emission values than DECSO. For inland point sources (Ruhr area, Reims and especially Paris), DECSO shows higher emission values. Hamburg has a similar emission rate for both data sets. Note that both methods do not allow for negative emissions.

In order to compute the emission maps, the flux-divergence map from the TROPDN experiment was selected (Section 4.5), as this adaptation performs best in the setting of this research. The following sections will discuss the results of each method used to estimate the sink term. All emission maps can be found in Appendix A.8.

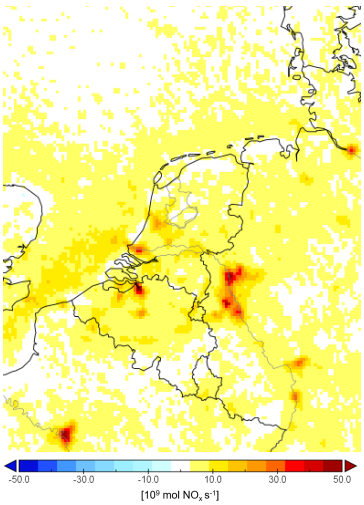

Figure 4.10: NO_x emission map for EMISB.

4.7.1. EMISB

The first emission maps were created using a reported multiplication factor of $m = 1.32$ and lifetime of $\tau = 4.00$, found in the paper of Beirle et al. [1]. These values lead to an emission map with very high background concentrations. This is clear from the high emission rate for the low-emission region. For the analysed point sources, the emission rates are mostly higher than the reported rates of both DECSO and CAMS-REG, with a few exceptions: EMISB and DECSO agree for Paris, and CAMS-REG reports higher emission rates for Tata Steel and Rotterdam. The emission map from Figure 4.10 on a coarse grid shows a high level of background emissions. This indicates that the chosen lifetime and multiplication factor do not succeed in adequately estimating the sink term. Larger point sources are still visible, but smaller point sources such as Reims are not.

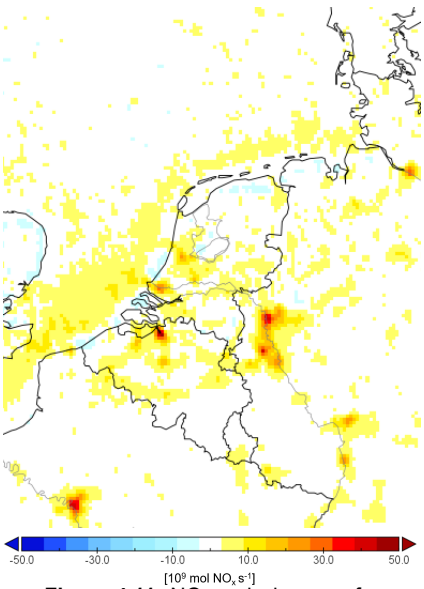

Figure 4.11: NO_x emission map for EMISO-5

Overall, it is not recommended to use this approach in computing the sink term. Most emission rates are overestimated, and the high background emissions reduce the visibility of smaller point sources.

4.7.2. EMISO

The second approach to estimate the NO_2 sink term, optimizes the lifetime τ in such a way that emissions in areas where no emissions are expected are reduced as much as possible. The value of τ was varied between 1 and 24, and the optimum is reached for $\tau = 10.062$. The optimal value for m is then chosen in such a way that the analyzed emission peaks are as close as possible to the reported emission peaks of the CAMS-REG inventory. The value of m is varied between 1 and 4, and the optimum is reached for $m = 1.390$, which is close to the reported value from the EMISB experiment.

This approach works well to remove emissions in low-emission regions: for the analyzed low-emission region, the total emissions are around 16 times lower than for the EMISB experiments, and only 1.5 times as high as the CAMS-REG inventory. Figure

4.11 shows the resulting emissions. The strong background emissions found for EMISB have indeed decreased significantly. Emission sources are still visible on this map, including smaller sources like Reims.

Interestingly, the correlation coefficient with the DECSO data set is the lowest across all sink term estimation experiments in this thesis. The coastal hot spots (Tata Steel, Rotterdam, Antwerp and Hamburg) correlate well between these two data sets, but the Ruhr area and Paris differ strongly, with the DECSO reported value being significantly higher. The CAMS-REG data set shows similar emissions for the Ruhr area, although its reported emissions for Paris are half those of the EMISO experiment. On the other hand, emissions for Antwerp, and especially Tata Steel and Rotterdam, are higher in the CAMS-REG inventory.

4.7.3. EMISD

The final approach implemented to estimate the sink term, uses NO_2 lifetimes modelled by the DECSO algorithm. It must be noted that the maximal available latitude degree covered by the DECSO model is 55° N, which excludes most of the used low-emission region. All grid cells to the North of this latitude use a lifetime of 10 hours for the EMISD Experiment. This is the value found in the EMISO experiment. For this reason, the low-emission values reported in Table 4.3 are not representative for the validity of this approach. However, Figure 4.12 shows that emission in other low-emission regions, such as the region between France and the border of Belgium, contain hardly any emissions. Small-scale emitters in this region, such as Reims, are still visible. This shows that this approach does not underestimate lifetimes too much, as it removes unwanted background emissions, whilst still displaying strong signals from known peak emitters. It also does not overestimate lifetimes, as this would lead to large areas with negative emission values, which is now only the case for small parts of Northern Netherlands and Eastern England.

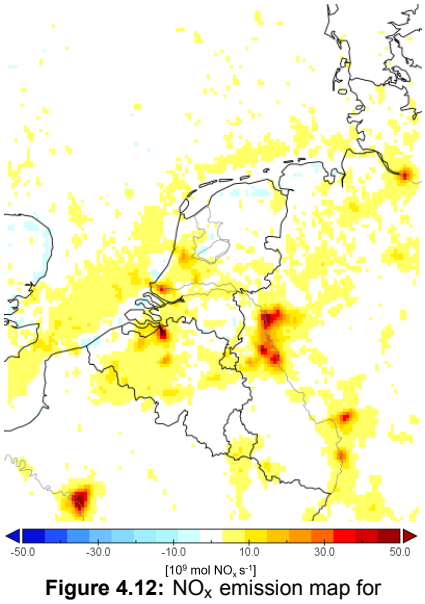

Figure 4.12: NO_x emission map for EMISD-5

The reported correlation coefficient betweeen EMISD and the CAMS-REG dataset is comparable to the correlation coefficient of the other two methods. The correlation coefficient between DECSO and EMISD is the highest across all experiments, and shows a strong relationship between the two data sets.

The emission rates for most peak emitters are higher than both DECSO and CAMS-REG for Hamburg, Paris, the Ruhr area and Antwerp. Tata Steel and Rotterdam are two emitters for which the CAMS-REG data set reports emissions rates that are double of the reported values of DECSO. Conversely, DECSO has a reported emission higher than the CAMS-REG data set for Reims. For these locations, EMISD reports values that are between the two data sets, but closer to the DECSO values.

To conclude, EMISB has the strongest correlation with the CAMS-REG data set, but shows large amounts of background emissions, and is therefore not a suitable approach to estimate lifetimes. This background emission is strongly reduced for EMISD and EMISO, with EMISD showing a strong correlation with the DECSO data set. The resulting emissions from the flux-divergence map are clearly very sensitive to the lifetimes used in the computation of the sink term.

4.8. Flux-Divergence Maps Ammonia

The final part of this research focuses on finding flux-divergence maps for ammonia satellite data, from the CrIS instrument (Section 2.2.2) . Section 3.11 elaborates on how some adjustments were made to the method, to make it more appropriate for the structure of the CrIS data set. The results of these experiments are discussed in this section. All experiments were performed on a coarser grid than the

previous experiments: the fine grid now has a resolution of approximately 10x10 km and the coarse grid now has a resolution of 20x20 km. This was done to match the coarser satellite data that is used.

4.8.1. NH3TIME*x*

The largest obstacle in computing the divergence is the fact that CrIS measures its VCD in circular footprints, which are at a distance from one another. This is in contrast with the continuous footprint of TROPOMI. This means that the VCDs should be averaged over a certain amount of time, in order to accumulate data and remove holes in the data set. The first experiment focuses on selecting a suitable period of time over which to average the VCD before computing the divergence. Three different averaging times are used: 1 month (June 2016), 3 months (June-August 2016) and 5 months (April-August 2016). These experiments are referred to as NH3TIME1, NH3TIME3 and NH3TIME5 respectively. All maps for these results are included in Appendix A.9.

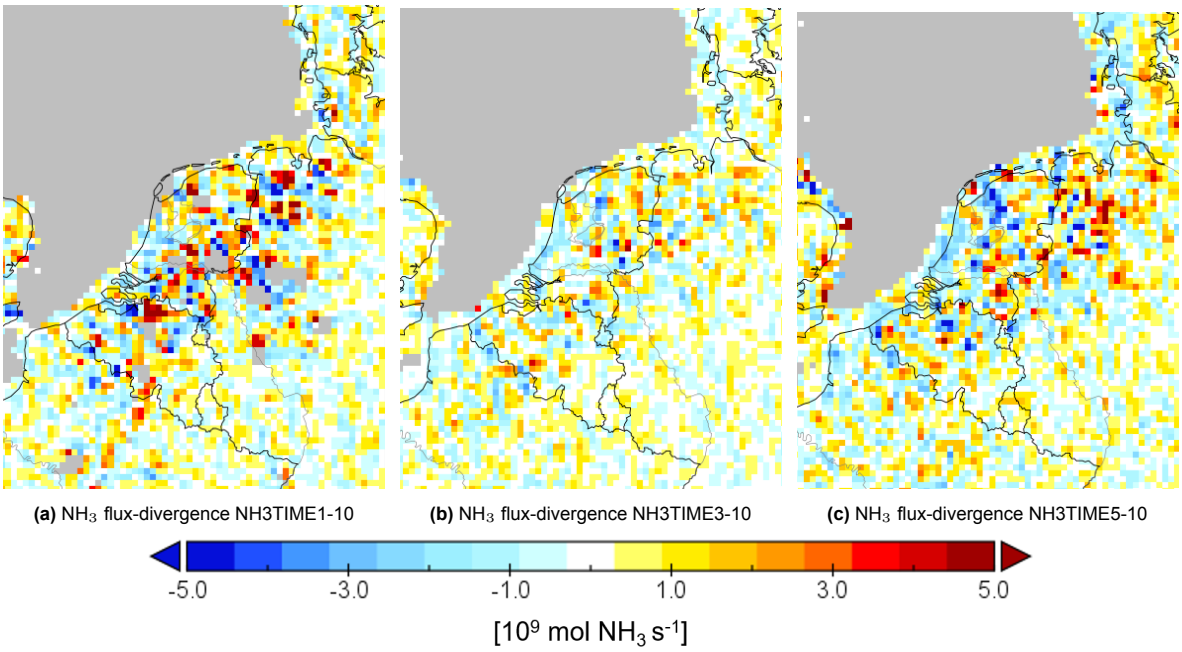

(a) NH_3 flux-divergence NH3TIME1-10 **(b)** NH_3 flux-divergence NH3TIME3-10 **(c)** NH_3 flux-divergence NH3TIME5-10

Figure 4.13: Results of NH3TIME experiments, on a 10x10 km resolution.

Figure 4.13 shows the results of the three different averaging times. After one month of averaging, there are still some gaps in the data. These gaps have disappeared after three months of averaging. After five months of averaging, the seasonal variation in ammonia emissions has significantly changed the flux-divergence intensity. Therefore, it is recommended to use three months of data, from a period of time with similar emission patterns.

These results also show that the Flux-Divergence method is not nearly as effective for ammonia as it is for nitrogen oxides. Averaging the data makes it possible to capture the VCD concentrations effectively. However, using the Flux-Divergence method leads to a noisy result. For the fine resolution model, some areas with higher emissions are still discernible, although the background regions are very noisy. For the coarse resolution model, the difference between noise and flux-divergence is unclear.

4.8.2. NH3MONTHAVG and NH3YEARAVG

In an effort to remove noise from the flux-divergence map, all CrIS summer data from 2015-2018 is downloaded. This allows for the computation of multiple flux-divergence maps, which can then be averaged to find a final result.

Two different options were implemented. On the one hand, we averaged all available data for every month separately, meaning there are three flux-divergence maps which we can average: June, July and August. On the other hand, we averaged all available data for each year separately, meaning

there were four flux-divergence maps that were then averaged. These experiments are referred to as NH3MONTHAVG and NH3YEARAVG, respectively. The resulting maps are shown in Appendix A.10 and A.11.

The VCD maps profit from the addition of more data, with a clear high-concentration region that matches bottom-up inventories. The filter that should flag data above sea does not work properly for all data sets.

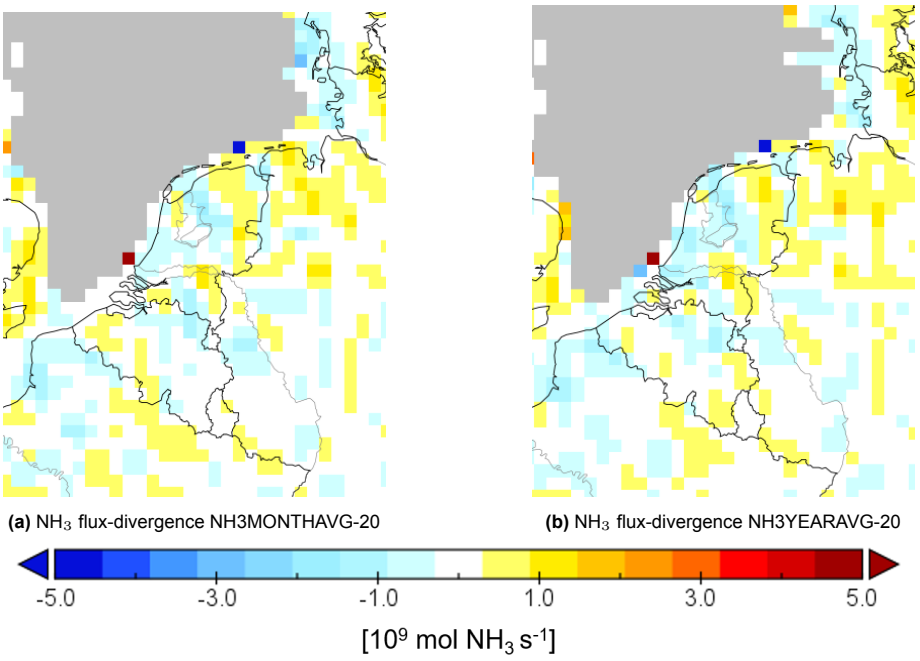

(a) NH_3 flux-divergence NH3MONTHAVG-20 **(b)** NH_3 flux-divergence NH3YEARAVG-20

Figure 4.14: Results of NH3AVG experiments, on a 20x20 km resolution.

The flux-divergence maps for the coarse resolution grid in Figure 4.14 show that this approach does not change the noise level significantly. There is little distinction between the NH3YEARAVG and NH3MONTHAVG experiment, and the level of noise ensures that the maps do not contain useful information that allows for the computation of ammonia emissions.

In conclusion, the flux-divergence method is highly suitable for pollutants with fixed, local emitters, such as NO_2. Ammonia has much larger emitters (agricultural areas), with lower emission rates per square meter. Therefore, the flux-divergence maps is too much influenced by the noise-to-signal ratio, and are not suitable for the estimation of emissions. Using the Flux-Divergence method for ammonia data depends on an accurate estimation of a lifetime for ammonia. This is a more promising approach than using flux-divergence maps, as the VCD maps are more well-structured, and show heightened ammonia concentrations where we expect them.

5

Conclusion and Discussion

This research focused on improving the current implementation of the Flux-Divergence method at the KNMI, and examining its sensitivities to different factors within the implementation. The current implementation is also referred to as the baseline scenario, to which different modifications are compared. In the introduction, three research questions were stated, which have been answered in this report. This section will formulate a clear conclusion for each question, using the results and methodology presented in Chapter 3 and 4. The first research question was:

***Research Question 1:* In which ways is it possible to improve the current KNMI implementation of the Flux-Divergence method when applied to NO_2 TROPOMI satellite data above the Netherlands?**

The Flux-Divergence method is governed by the following steady-state continuity equation:

$$\nabla \cdot \mathbf{f} = E - S$$

The Flux-Divergence method consists of two different terms that need to be estimated in order to find an emission map (E): the flux-divergence map ($\nabla \cdot \mathbf{f}$) and the sink term (S). The flux-divergence term is the focus of the first sub-question:

Research Question 1a: *How do different choices in the following factors influence the flux-divergence map:*

- *grid resolution,*
- *grid on which divergence is computed,*
- *finite difference method,*
- *wind data and*
- *a priori distribution.*

Each factor will be discussed separately.

Grid Resolution

Two grid cell resolutions were used for this research, one coarse grid (5x5 km) and one fine grid (2.5x2.5 km). The first resolution is similar to the TROPOMI footprint. In the baseline implementation, the fine grid introduced more noise than the coarse grid. Two factors contribute to this extra noise.

The first factor is that the interpolation of the vertical columns density (VCD) of NO_2 to a fine grid introduces slightly more noise than the interpolation to a coarse grid. A possible explanation for the

extra noise on the fine grid as compared to the coarse grid in the interpolation step could be its large difference in size with the original TROPOMI pixel. One TROPOMI pixel covers on average at least four fine grid cells, as opposed to only one grid cell on the coarse grid. In areas with low NO_2 concentrations, where the signal-to-noise ratio is higher ([42]), one noisy TROPOMI pixel therefore influences more pixels on the fine grid, creating more noisy concentration maps in these regions. As the used finite difference methods are sensitive to this noise, this has a larger influence on the computation of the flux-divergence map for the fine grid cells.

The second factor is that the division in the flux-divergence computation has less of a smoothing property. To compute the finite difference flux-divergence, the formula shown in Equation 3.6is used. We divide the difference in flux between neighboring grid cells by the distance between their centers. Dividing by the distance between grid cells has a dampening effect on flux-divergence. As the distance between grid cells in the fine grid is smaller, this dampening effect is also smaller, and the noise is more persistent.

A major advantage of using the fine grid, is that it better defines the boundaries of emission hot spots. Regions with multiple emission sources close together, such as the Ruhr area, are smeared into one emission source on a coarse grid. However, they can still be distinguished on a fine grid. Therefore, a method that contains this information of the fine grid, but limits its noise, is optimal.

The spatial averaging step introduced in Section 3.5 (Experiment SAVG) does not provide a solution to reduce noise during the interpolation step. In fact, it adds more noise to the coarse resolution map. It seems that this extra noise is caused by using noisy data from a fine grid as an input. Therefore, it is better to initially grid the satellite data directly to a coarser resolution. However, the refined emission sources are also still visible after spatially averaging to a coarse grid. A method that includes the reduced noise of a coarse grid with the precision of a fine grid would be optimal, but spatial averaging is not adequate, and creates maps that are not an improvement to the original method.

In conclusion, the Flux-Divergence method is highly sensitive to the resolution on which it is used. A fine resolution leads to noisy results in low-emission areas, but also better defines regions with a high emission rate. Oversampling better positions emission sources, and benefits from the changing location of TROPOMI pixels.

Grid on which divergence is computed

In the baseline implementation, the NO_2 VCD was first interpolated to a regular grid, on which the flux and divergence was then computed. In the TROPN, TROPD and TROPDN experiments, this order was reversed. The flux and divergence were computed on the TROPOMI pixels, or TROPOMI grid. The divergence was then interpolated to a regular grid, to allow for temporal averaging. TROPN used only nearest neighbors to compute the divergence, TROPD used only diagonal neighbors, and TROPDN used both. These experiments were successful at reducing noise, both on a coarse grid and most drastically on a fine grid. This can be seen visually, but is also reflected in metrics such as the SDN and RSS.

The first reason for this noise reduction is that the interpolation step does not impact the finite difference method. This is visible in the results for the coarse grid. A second reason for the noise reduction is that the damping effect of the division is larger, especially for the fine grid. The distance between TROPOMI grid cells is larger than the distance between grid cells on the regular fine grid. The total emission does not change significantly, so this noise reduction is not caused by an overall bias. The results of TROPDN on a fine grid are shown in Figure 4.8.

We also show that including diagonal divergence when computing the flux-divergence dampens noise. This is caused by the larger distance between the diagonal neighbors as opposed to the nearest neighbors. However, when using only diagonal neighbors, the damping was so strong, that the smearing effect on the peak emitters counteracted the positive effect of using a fine grid. Including both diagonal divergence and nearest neighbor divergence, allows for a significant reduction in noise, and maintains well-defined emission points.

To conclude, the setting of the TROPDN experiment yields a significant improvement compared to the original baseline implementation. The total amount of emission is not sensitive to the order of interpolation and divergence computation, but the amount of noise is.

Finite Difference Method

The finite difference method used in the baseline scenario, is the second order central difference method, including diagonal divergence. Two other finite different methods were used: the second order central difference method using only nearest neighbors (DIVSON), and the fourth order central difference method (DIVFON). In the setting of this research, the original baseline scenario yielded the best results. Both DIVFON and DIVSON yielded more noise.

In the case of DIVSON, a possible explanation for this noise-inducing effect can be due to the fact that only the nearest neighbors are considered for the divergence computation, and the diagonal divergence is omitted. The difference terms in these calculations are divided by a distance term, more precisely the distance between the centers of the grid cells and the centers of the neighboring/diagonal grid cells. In the case of diagonal divergence, this distance is higher, meaning diagonal divergence has a somewhat dampening effect. When the diagonal divergence is omitted, this dampening effect on the noise is also lost. The dampening effect of the diagonal neighbors also somewhat smears the emission hot spots.

The DIVFON experiment gives more noise than the DIVSON experiment, although the used finite difference method has a higher theoretical accuracy. However, part of the error term of the finite difference method is caused by noise, as shown in Equation 2.44. This part of the error term gets larger for smaller terms of h, which explains the extra noise present on the fine grid. This measurement error term is also larger than the measurement error term of the second order central finite difference method. It appears this error term has a larger impact than the truncation error.

In conclusion, the finite different method used in the baseline scenario to compute the results, yields the least noisy result when compared to other central finite difference methods.

Wind data

In order to compute the flux, a wind data set is needed. The baseline scenario uses a wind data set where the wind speed is taken halfway the Planetary Boundary Layer (PBL). This thesis analysed the impact of using two other wind data sets. One wind data set took an average over the wind speeds within the PBL (Experiment WINDMEAN). For the other wind data set, we implemented an algorithm that reduces local divergence in a flux field (WINDDIV).

The WINDMEAN experiment shows that using a different metric to project the 3D wind field within the PBL to a 2D wind field does not have a large impact on the final flux-divergence map. This is shown in the value for the SDN, which is almost the same as the SDN of the baseline scenario. The RSS and RSL are both close to 1.The slightly lower values for the averaged wind data set as opposed to the baseline wind data set also leads to a slightly lower flux-divergence. However, it does not structurally change the resulting flux-divergence map.

The WINDDIV experiment shows that it is beneficial to use a wind data set with reduced divergence. In the Netherlands, the largest divergence in wind is experienced along the coast. The abrupt change in surface fraction leads to a high-divergence region along the coast above sea, and a low-divergence region along the coast above land. As the Flux-Divergence method assumes all positive divergence in the flux is caused by emission and deposition, the coastal divergence is incorrectly attributed. The effect causes a strong increase in estimated emission above sea, but also a decrease for emitters that are located along the coast, such as Tata Steel and the port of Rotterdam. A fast algorithm is provided that partially removes local divergence effects, while maintaining the overall structure of the wind. As a result, only the strongest emission remains above the sea, such as emission along the connection between Dover and Calais. The emission rates of Tata Steel and the port of Rotterdam are enhanced. Compared to the CAMS-REG inventory, the emission of these hot spots are underestimated using the normal wind data set, as shown in Table 4.3. The flux-divergence map of the WINDDIV experiment on a coarse grid is compared to the baseline results in Figure 4.5.

The WINDDIV experiment also shows that the flux-divergence map does not capture emissions from mobile sources well, such as big cargo ships. Using divergence-free wind results in a slight amplification along the coast, but this is hardly distinguishable from noise. Less-heavily trafficked routes, such as the route connecting the Netherlands and Scandinavia, are not visible. This shows that the flux-divergence map is very good at picking up emissions from fixed, local emitters, such as power plants or cities. The gradient of the flux near such sources is high, as there is a large difference between neighboring grid

cells. However, for emission sources such as ships, the emission of NO_2 is done at a lower rate per ship, and is spread out over a large region. This is not properly captured in the flux-divergence term. Such emissions rely mostly on a reliable estimation of the sink term to be captured using the Flux-Divergence method. However, this is typically much harder than estimating a flux-divergence map.

Road traffic is better detected than ship transport on flux-divergence maps, presumably because of its denser concentration. Highways that are visible on the map are the A4 highway, connecting The Hague and Amsterdam, and the Route du Soleil in southerly direction from Luxembourg.

To conclude, the Flux-Divergence method is not very sensitive to using a different estimate of the wind velocity within the PBL. However, removing divergence from the wind data set does have a large influence and benefits emission estimates from emitters in regions with negative wind divergence, such as Tata Steel and the port of Rotterdam.

A-Priori

The baseline implementation uses a high resolution vertical column profile a-priori for TROPOMI's NO_2 retrieval algorithm. This a-priori profile is called the CAMS a-priori and was developed by Douros et al. [74]. This research applied a different low-resolution a-priori, called the TM5-MP a-priori (the DAP experiment). The DAP experiment shows that the Flux-Divergence method is highly sensitive to the used a-priori. The CAMS a-priori gives higher vertical column density values than the TM5-MP a-priori. This also leads to higher flux-divergence values and a 17% increase in emission values. As literature shows, the CAMS a-priori gives better emission values upon validation, and should therefore be used [45] [74].

The second subquestion of this research focused on the sink term of NO_2:

Research Question 1b: How can the NO_2 sink term better be estimated by optimizing the NO_2 lifetime or using DECSO estimates for the lifetime?

This research used three different approaches to estimate the lifetime of NO_x in order to compute the sink term. The first approach used a fixed lifetime of NO_2 of 4.0h, which was retrieved from empirical studies in Riyadh [69]. The experiment is referred to as EMISB. The second approach used a constant optimized lifetime, which minimizes the emissions in a low-emission region (EMISO). The third approach, called EMISD, uses NO_x lifetimes retrieved from the DECSO algorithm which is currently being developed at the KNMI [3]. The retrieved emissions are compared to two emission inventories: the CAMS-REG inventory, which uses a bottom-up approach to compute emissions, and the DECSO inventory, which uses data assimilation to incorporate satellite data.

All resulting emission maps from the lifetime experiments show a strong correlation with the DECSO data set, and a mildly strong correlation with the CAMS-REG inventory. This makes sense, as the DESCO data set also uses satellite data, and is thus structured similarly. The CAMS-REG data set mostly uses a bottom-up approach, and therefore provides a more localized version of peak emitters. Especially transport emission from ships and road traffic are better structured in that way. The values reported show that all data sets largely agree on the location of emitters.

We show that the fixed lifetime used in EMISB is an underestimation of the lifetime for the region of the Netherlands, and leads to an overestimation of emissions. This is best seen in the low-emissions value shown in Table 4.3. Analysis of low-emission regions shows that using the optimized lifetimes and the DECSO lifetimes gives better results than using the lifetimes found in literature. Both values are similarly low, and only twice as high as the CAMS-REG inventory.

The emission rate found by EMISO and EMISD for certain hot spots, shown in Table 4.3, largely correspond to the emission rates found by the CAMS-REG inventory. Only the reported emissions of coastal hot spots Tata Steel and Rotterdam are underestimated using both the optimized lifetimes and DECSO lifetimes, possibly due to the presence of negative divergence in the wind fields of this region. On the other hand, the reported emissions for Paris are much higher for satellite-based methods, including the DECSO data set.

These experiments show that the emission rates found using the Flux-Divergence method are highly sensitive to the estimation of the sink term and the linked NO_x lifetime. This value should thus be chosen with care. For each used lifetime estimation, the Flux-Divergence method emission map has a high correlation with the DECSO emission map, and a moderately high correlation with the CAMS-REG emission inventory.

Research question 2 focused on applying the Flux-Divergence method to ammonia emission data from the CrIS instrument.

***Research Question 2:* What is the result of a flux-divergence map for NH_3 concentrations from satellite data above the Netherlands?**

Different approaches were implemented to find a flux-divergence map for ammonia emission. The VCD was averaged over one month, three months and five months, in the NH3TIME experiments. Two different ways to average flux-divergence were used in the NH3MONTHAVG and NH3YEARAVG experiments. None of these experiments led to a useful flux-divergence map.

The emission of ammonia in the Netherlands occurs mostly above agricultural land, as shown in the VCD maps in Figure A.15. This emission source is much more spread out than the compact point-sources of NO_2. A flux-divergence map is not able to capture this as a source. The grid size being used is much smaller than the size of the region emitting ammonia. Therefore, when computing the divergence of the flux, no difference is found between neighboring grid cells, and the region is not recognized as a source. This is clear when examining the resulting flux-divergence maps in Figures A.12, A.13, A.14 and A.15. Taking a larger grid size does not yield better results. Moreover, choosing a grid size that matches the size of the emitting region counteracts the resolution of the available CrIS data set. When using the Flux-Divergence method for ammonia, the importance of a sink term is thus even higher. Given that it is possible to create VCD maps that meet expectation of ammonia concentration, we can conclude that an accurate lifetime also leads to a useful emission map.

Another issue with CrIS data that hinders the performance of the Flux-Divergence method on NH_3, is the fact that the pixels are not adjacent to each other. This means that the flux must first be averaged over a certain period of time, before the divergence can be computed. This raises some issues, as measurements from different time stamps are compared and used to find the divergence.

To conclude, the flux-divergence map does not properly capture NH_3 emissions. When applying the Flux-Divergence method to NH_3, the sink term contains the most useful information in computing an emission map.

Discussion and Future Research

This thesis raises some interesting questions that requires more research. This section discusses some issues that should be examined in future research within this topic.

This method assumes a steady state continuity equation. However, this is not necessarily the case, as the amount of a certain trace gas can fluctuate. In the case of NO_2 and NH_3, this fluctuation is linked amongst others to temperature. Therefore, future research could include a time derivative in the continuity equation.

As was remarked in Section 2.2.1, the relative uncertainty for low concentrations of NO_2 can be as high as 100%. This was not accounted for in this research. Pixels were filtered based on their quality factor. However, experiments should be done to analyse the influence of such pixels with high uncertainty. Especially when this method is used to give concrete estimations of emission rates, this should be assessed.

The metrics used to analyse the influence of a certain factor on the Flux-Divergence method were the total emission, the standard deviation in a low-emission region, and the slopes of Theil-Sen regressor fitted on large and small flux-divergence values. However, in future research, an extra metric should be included that deteriorates when emission hot spots are less well-defined. This is a quality that was

assessed visually for this research, but this should also be done analytically. A possible approach could be to use a peak-fitting algorithm on certain hot spots.

The algorithm used to remove divergence from wind has only been validated for the current research domain. For this region, we showed that the algorithm removes divergence locally. However, the region does not have strong topographic features, such as mountain ranges. The validity of this method should therefore also be validated for other regions with different orographic features. It is also interesting to evaluate the algorithm at different wind speed heights. It would also be interesting to examine the location of the high- and low-divergence regions for the wind and how this location changes for different wind directions.

Using this wind data with reduced divergence seems to improve emission in regions where the wind divergence is negative. However, this method assumes two-dimensional transport of trace gases. In practice, the transport of air through the Planetary Boundary layer is three-dimensional. Divergence in the wind field could also indicate vertical transport of air, and thus also of trace gases. Clean air is added to the grid cell from above, while polluted air is transported horizontally. More research should be done on whether or not divergence in wind should be included, and if it properly models vertical pollutant transport. If it turns out that wind divergence does not capture vertical transport, perhaps a different method should be found to incorporate this.

Looking at sensitivity of the Flux-Divergence method for the lifetime of NO_x shows that much future research should be done to include better lifetimes. The optimized lifetime approach assumes a fixed lifetime for NO_2. In real life, however, this is not the case. The lifetime of NO_2 also depends on the amount of OH available. It is also strongly seasonally dependent. This should therefore be included in future models. The DECSO lifetime does not assume a fixed lifetime. However, little research has been done to validate the retrieved lifetimes. This could be a solution for future models used at the KNMI.

This research analyzed the sensitivity of the flux-divergence map to different factors in its implementation. However, this was not translated to sensitivity of the emission rates to these choices. Is should definitely be included in future research.

Despite the difficulties in estimating the lifetime of NO_2, the Flux-Divergence method is a very promising tool in the creation of emission maps for NO_2 using TROPOMI data. It is a computationally efficient method to implement. Another big advantage is that the method is based on a simple principle, thereby making the computation of emission values more transparent to the public.

In the case of NH_3, this thesis only focused on the flux-divergence term. This gave a noisy result. However, the VCD map did meet expectations set by previous NH_3 concentration maps. Therefore, it could be possible to find an adequate sink term, and use this in the computation of an emission map. This should be researched.

The circular structure of the current available NH_3 data is not well suited for the Flux-Divergence method. It is not possible to reverse the order of interpolation and divergence computation, which yielded an improvement for this method when applied to NO_2. If satellite data becomes available that has a measuring swath comparable to that of TROPOMI, the method could be more successful, as temporal averaging before divergence computation is not necessary anymore. However, other methods seem to be more promising. An important example is the DECSO method, which uses Kalman filters to estimate ammonia emissions [3].

At the moment of writing this thesis, satellite data is not yet used in the Netherlands to help form policies. However, in September 2022, the NKS-SAGEN research program commenced. In this program, different research institutes such as KNMI, but also TNO, ULeiden, WUR and the RIVM, bundle their knowledge to start incorporating satellite data in the creation of emission maps used for the development of Dutch policies. The Flux-Divergence method is one of the tools that will be used by this research program.

In conclusion, this research shows the strengths of the Flux-Divergence method in an improved implementation, applied to TROPOMI data for NO_2 concentrations. This improved implementation reduces noise, most drastically on a fine grid, by reversing the order of divergence computation and interpolation to a regular grid. The research also develops a tool to better detects point sources in

regions with negative wind divergence, by reducing divergence in the wind data set. The sensitivities of the flux-divergence map to different implementation choices are analysed. The limits of the flux-divergence map are also explored, in the application to NH_3 data of the CrIS instrument. Figure 5.1 shows a final comparison of the improved Flux-Divergence method emission maps, the CAMS-REG inventory, and the DECSO algorithm. Table 5.1 qualitatively summarizes the impact of different factors on the Flux-Divergence method.

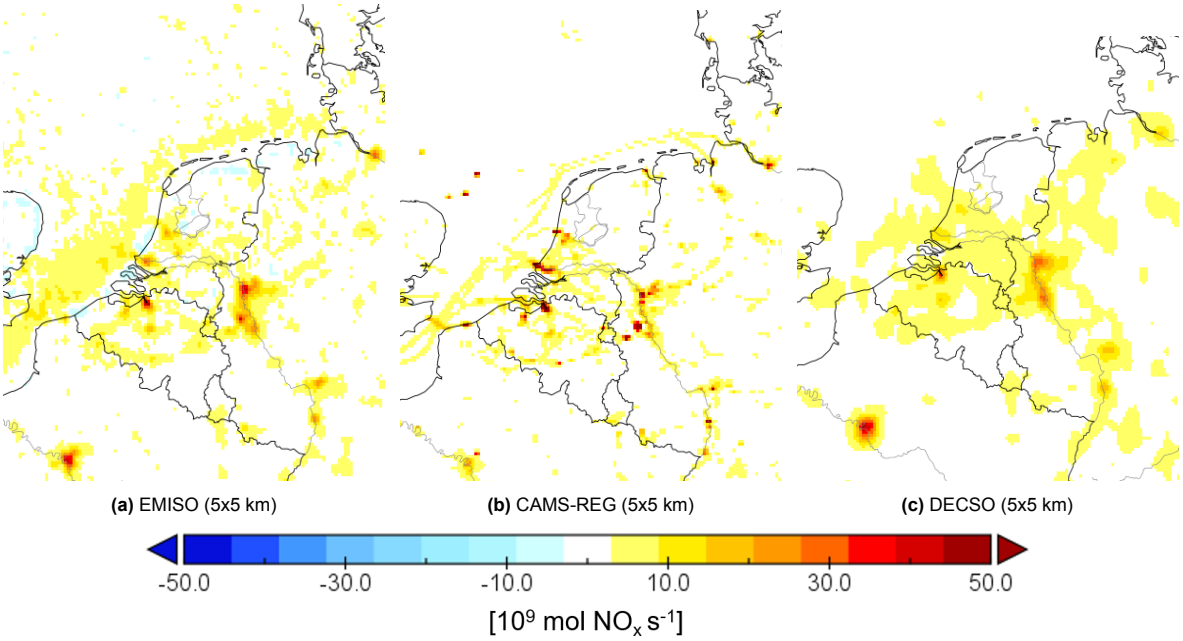

Figure 5.1: A comparison of the improved Flux-Divergence method implementation (TROPDN experiment using EMISO lifetime approach), the CAMS-REG inventory and the DECSO inventory (currently still being developed at the KNMI).

Low impact
Using different wind metric (WINDMEAN)
Moderate impact
Finite Difference method (DIVFON/DIVSON and TROPDN/TROPD/TROPN) Reducing Wind Divergence (WINDDIV) Spatial Averaging (SAVG)
High impact
A-priori vertical profile (DAP) Computing divergence on TROPOMI grid (TROPDN/TROPD/TROPN) Lifetime estimation (EMISB/EMISO/EMISD)

Table 5.1: This table qualitatively summarizes the impact of different choices on the result of the Flux-Divergence method applied to NO_x. The division is made on a combination of the values found for the SDN, TE, RSS, RSL, visual analysis and reported emission rates.

References

[1] S. Beirle, C. Borger, S. Dörner, *et al.*, “Pinpointing nitrogen oxide emissions from space”, *Science advances*, vol. 5, no. 11, eaax9800, 2019.

[2] S. Beirle, C. Borger, S. Dörner, *et al.*, “Catalog of nox emissions from point sources as derived from the divergence of the no2 flux for tropomi”, *Earth System Science Data*, vol. 13, no. 6, pp. 2995–3012, 2021.

[3] B. Mijling and R. Van Der A, “Using daily satellite observations to estimate emissions of short-lived air pollutants on a mesoscopic scale”, *Journal of Geophysical Research: Atmospheres*, vol. 117, no. D17, 2012.

[4] M. R. Rands, W. M. Adams, L. Bennun, *et al.*, “Biodiversity conservation: Challenges beyond 2010”, *Science*, vol. 329, no. 5997, pp. 1298–1303, 2010.

[5] European Commission, *Natura 2000 - environment*, Accessed: 06-12-2022, 2016. [Online]. Available: https://ec.europa.eu/environment/nature/natura2000/index_en.htm.

[6] ——, *Council directive 92/43/eec of 21 may 1992 on the conservation of natural habitats and of wild fauna and flora*, Accessed: 06-12-2022, 1992. [Online]. Available: https://eur-lex.europa.eu/legal-content/EN/TXT/?uri=celex%5C%3A31992L0043.

[7] Rijksinstituut voor Volksgezondheid en Milieu, *Stikstof-reductie opties effectiviteit en streefwaarden*, Accessed: 06-12-2022, 2020. [Online]. Available: https://www.rivm.nl/sites/default/files/2020-04/V4%5C%20Presentatie%5C%20BWO%5C%206%5C%20maart%5C%202020.pdf.

[8] Raad van State, *Pas mag niet als toestemmingsbasis voor activiteiten worden gebruikt*, Accessed: 06-12-2022, 2019. [Online]. Available: https://web.archive.org/web/20190930203505/https://www.raadvanstate.nl/@115651/pas-mag/.

[9] Ministerie van Justitie en Veiligheid, *Wet van 10 maart 2021 tot wijziging van de wet natuurbescherming en de omgevingswet (stikstofreductie en natuurverbetering)*, Accessed: 06-12-2022, 2021. [Online]. Available: https://zoek.officielebekendmakingen.nl/stb-2021-140.html.

[10] J. D. van der Ploeg, “Farmers’ upheaval, climate crisis and populism”, *The Journal of Peasant Studies*, vol. 47, no. 3, pp. 589–605, 2020.

[11] M. Kowalska, M. Skrzypek, M. Kowalski, and J. Cyrys, “Effect of nox and no2 concentration increase in ambient air to daily bronchitis and asthma exacerbation, silesian voivodeship in poland”, *International Journal of Environmental Research and Public Health*, vol. 17, no. 3, p. 754, 2020.

[12] J. Veefkind, I. Aben, K. McMullan, *et al.*, “Tropomi on the esa sentinel-5 precursor: A gmes mission for global observations of the atmospheric composition for climate, air quality and ozone layer applications”, *Remote sensing of environment*, vol. 120, pp. 70–83, 2012.

[13] R. J. Glumb and D. C. Jordan, “Enhancements to the crosstrack infrared sounder (cris) for improved radiometric accuracy”, *Infrared Spaceborne Remote Sensing VIII*, vol. SPIE 4131, pp. 323–333, 2000.

[14] M. Liu, R. van der A, M. van Weele, *et al.*, “A new divergence method to quantify methane emissions using observations of sentinel-5p tropomi”, *Geophysical Research Letters*, vol. 48, no. 18, e2021GL094151, 2021.

[15] B. Dix, C. Francoeur, B. McDonald, *et al.*, “Nox emissions from us oil and gas production using tropomi no2 and the divergence method”, *EGU General Assembly Conference Abstracts*, EGU21–13 554, 2021.

[16] J. W. Erisman, W. de Vries, and e.a., *Stikstof - De sluipende effecten op natuur en gezondheid.* Amsterdam, The Netherlands: Uitgeverij Lias, 2021.

[17] G. P. Brasseur, J. J. Orlando, and G. S. Tyndall, *Atmospheric Chemistry and Global Change*. New York, USA: Oxford University Press, 1999.

[18] European Comission, *Emissions in the automotive sector*, Accessed: 02-09-2022, 2022. [Online]. Available: https://single-market-economy.ec.europa.eu/sectors/automotive-industry/environmental-protection/emissions-automotive-sector_en.

[19] K. F. Boersma, G. C. Vinken, and J. Tournadre, "Ships going slow in reducing their nox emissions: Changes in 2005–2012 ship exhaust inferred from satellite measurements over europe", *Environmental Research Letters*, vol. 10, no. 7, p. 074 007, 2015.

[20] K. A. Hossain and N. G. Zakaria, "A study on global shipbuilding growth, trend and future forecast", *Procedia engineering*, vol. 194, pp. 247–253, 2017.

[21] S. Jutterström, F. Moldan, J. Moldanová, M. Karl, V. Matthias, and M. Posch, "The impact of nitrogen and sulfur emissions from shipping on the exceedance of critical loads in the baltic sea region", *Atmospheric chemistry and physics*, vol. 21, no. 20, pp. 15 827–15 845, 2021.

[22] Central Bureau for Statistics, *Emissies van luchtverontreinigende stoffen volgens nec-richtlijnen*, Accessed: 10-10-2022, 2022. [Online]. Available: https://opendata.cbs.nl/#/CBS/nl/dataset/70947ned/table.

[23] R. Delmas, D. Serça, and C. Jambert, "Global inventory of nox sources", *Nutrient cycling in agroecosystems*, vol. 48, no. 1, pp. 51–60, 1997.

[24] L. Jaeglé, L. Steinberger, R. V. Martin, and K. Chance, "Global partitioning of nox sources using satellite observations: Relative roles of fossil fuel combustion, biomass burning and soil emissions", *Faraday discussions*, vol. 130, pp. 407–423, 2005.

[25] T. Stavrakou, J.-F. Müller, K. Boersma, *et al.*, "Key chemical no x sink uncertainties and how they influence top-down emissions of nitrogen oxides", *Atmospheric Chemistry and Physics*, vol. 13, no. 17, pp. 9057–9082, 2013.

[26] W. A. Asman, M. A. Sutton, and J. K. Schjørring, "Ammonia: Emission, atmospheric transport and deposition", *The New Phytologist*, vol. 139, no. 1, pp. 27–48, 1998.

[27] F. Paulot, D. J. Jacob, M. T. Johnson, *et al.*, "Global oceanic emission of ammonia: Constraints from seawater and atmospheric observations", *Global Biogeochemical Cycles*, vol. 29, no. 8, pp. 1165–1178, 2015.

[28] G. Lammel and H. Graßl, "Greenhouse effect of nox", *Environmental Science and Pollution Research*, vol. 2, no. 1, pp. 40–45, 1995.

[29] A. Singh and M. Agrawal, "Acid rain and its ecological consequences", *Journal of Environmental Biology*, vol. 29, no. 1, pp. 15–24, 2007.

[30] W. A. Wurtsbaugh, H. W. Paerl, and W. K. Dodds, "Nutrients, eutrophication and harmful algal blooms along the freshwater to marine continuum", *Wiley Interdisciplinary Reviews: Water*, vol. 6, no. 5, e1373, 2019.

[31] J. J. Beaulieu, T. DelSontro, and J. A. Downing, "Eutrophication will increase methane emissions from lakes and impoundments during the 21st century", *Nature communications*, vol. 10, no. 1, pp. 1–5, 2019.

[32] A. César, J. Carvalho Jr, and L. Nascimento, "Association between nox exposure and deaths caused by respiratory diseases in a medium-sized brazilian city", *Brazilian Journal of Medical and Biological Research*, vol. 48, pp. 1130–1135, 2015.

[33] K. Dornelles, M. Roriz, V. Roriz, and R. Caram, "Thermal performance of white solar-reflective paints for cool roofs and the influence on the thermal comfort and building energy use in hot climates", in *ISES Solar World Congress*, Kassel, Germany, 2011, pp. 1–12.

[34] J. Burrows, E. Hölzle, A. Goede, H. Visser, and W. Fricke, "Sciamachy—scanning imaging absorption spectrometer for atmospheric chartography", *Acta Astronautica*, vol. 35, no. 7, pp. 445–451, 1995.

[35] S. Pandey, R. Gautam, S. Houweling, *et al.*, "Satellite observations reveal extreme methane leakage from a natural gas well blowout", *Proceedings of the National Academy of Sciences*, vol. 116, no. 52, pp. 26 376–26 381, 2019.

[36] D. G. Loyola, S. Gimeno García, R. Lutz, *et al.*, "The operational cloud retrieval algorithms from tropomi on board sentinel-5 precursor", *Atmospheric Measurement Techniques*, vol. 11, no. 1, pp. 409–427, 2018.

[37] J. P. Burrows, U. Platt, and P. Borrell, *The Remote Sensing of Tropospheric Composition from Space*. Berlin Heidelberg, Germany: Springer-Verlag, 2011.

[38] M. N. Deeter, *Calculation and application of mopitt averaging kernels*, Accessed: 06-12-2022, 2002. [Online]. Available: https://www.acom.ucar.edu/mopitt/MOPITT/data/avg_krnls_app.pdf.

[39] K. Bogumil, J. Orphal, T. Homann, *et al.*, "Measurements of molecular absorption spectra with the sciamachy pre-flight model: Instrument characterization and reference data for atmospheric remote-sensing in the 230–2380 nm region", *Journal of Photochemistry and Photobiology A: Chemistry*, vol. 157, no. 2-3, pp. 167–184, 2003.

[40] J. P. Burrows, M. Weber, M. Buchwitz, *et al.*, "The global ozone monitoring experiment (gome): Mission concept and first scientific results", *Journal of the Atmospheric Sciences*, vol. 56, no. 2, pp. 151–175, 1999.

[41] P. Levelt, G. Van den Oord, M. Dobber, *et al.*, "The ozone monitoring instrument", *IEEE Transactions on Geoscience and Remote Sensing*, vol. 55, pp. 1093–1101, 5 2006.

[42] Koninklijk Nederlands Meteorologisch Instituut, *Algorithm theoretical basis document for the tropomi l01b data processor, tech. rep. s5p-knmi-l01b-0009-sd, ci-6480-atbd, issue 8.0.0*, Accessed: 14-10-2022, 2019. [Online]. Available: https://josvg.home.xs4all.nl/KNMI/papers/KNMI-ESA-S5L2PP-ATBD-001-v3.1-20190517-NO2.pdf.

[43] J. van Gent, *Three years of tropomi measurements*, Accessed: 14-10-2022, 2021. [Online]. Available: https://www.aeronomie.be/en/news/2021/three-years-tropomi-measurements.

[44] J. E. Williams, K. F. Boersma, P. Le Sager, and W. W. Verstraeten, "The high-resolution version of tm5-mp for optimized satellite retrievals: Description and validation", *Geoscientific Model Development*, vol. 10, no. 2, pp. 721–750, 2017.

[45] I. Ialongo, H. Virta, H. Eskes, J. Hovila, and J. Douros, "Comparison of tropomi/sentinel-5 precursor no 2 observations with ground-based measurements in helsinki", *Atmospheric Measurement Techniques*, vol. 13, no. 1, pp. 205–218, 2020.

[46] R. Beer, M. W. Shephard, S. S. Kulawik, *et al.*, "First satellite observations of lower tropospheric ammonia and methanol", *Geophysical Research Letters*, vol. 35, no. 9, 2008.

[47] D. Blumstein, G. Chalon, T. Carlier, *et al.*, "Iasi instrument: Technical overview and measured performances", *Infrared Spaceborne Remote Sensing XII*, vol. 5543, pp. 196–207, 2004.

[48] M. Shephard and K. Cady-Pereira, "Cross-track infrared sounder (cris) satellite observations of tropospheric ammonia", *Atmospheric Measurement Techniques*, vol. 8, no. 3, pp. 1323–1336, 2015.

[49] Y. Han, H. Revercomb, M. Cromp, *et al.*, "Suomi npp cris measurements, sensor data record algorithm, calibration and validation activities, and record data quality", *Journal of Geophysical Research: Atmospheres*, vol. 118, no. 22, pp. 12, 734–12, 748, 2013.

[50] C. D. Rodgers, *Inverse Methods for Atmospheric Sounding*. Singapore, Singapore: World Scientific Publishing, 2000.

[51] M. W. Shephard, E. Dammers, K. E. Cady-Pereira, *et al.*, "Ammonia measurements from space with the cross-track infrared sounder: Characteristics and applications", *Atmospheric Chemistry and Physics*, vol. 20, no. 4, pp. 2277–2302, 2020.

[52] J. Kuenen, S. Dellaert, A. Visschedijk, J.-P. Jalkanen, I. Super, and H. Denier van der Gon, "Cams-reg-v4: A state-of-the-art high-resolution european emission inventory for air quality modelling", *Earth System Science Data*, vol. 14, no. 2, pp. 491–515, 2022.

[53] UNECE, *1999 protocol to abate acidification, eutrophication and ground-level ozone to the convention on long-range transboundary air pollution, as amended on 4 may 2012*, (Accessed: 17-10-2022), 2012. [Online]. Available: https://www.unece.org/fileadmin/DAM/env/documents/2013/air/eb/ECE.EB.AIR.114_ENG.pdf.

[54] European Commission, *Directive (eu) 2016/2284 on the reduction of national emissions of certain atmospheric pollutants*, (Accessed: 17-10-2022), 2016. [Online]. Available: https://eur-lex.europa.eu/legal-content/EN/TXT/?uri=uriserv:OJ.L_.2016.344.01.0001.01.ENG&toc=OJ:L:2016:344:TOC.

[55] J.-P. Jalkanen, L. Johansson, J. Kukkonen, A. Brink, J. Kalli, and T. Stipa, "Extension of an assessment model of ship traffic exhaust emissions for particulate matter and carbon monoxide", *Atmospheric Chemistry and Physics*, vol. 12, no. 5, pp. 2641–2659, 2012.

[56] J. Kaiser, A. Heil, M. Andreae, *et al.*, "Biomass burning emissions estimated with a global fire assimilation system based on observed fire radiative power", *Biogeosciences*, vol. 9, no. 1, pp. 527–554, 2012.

[57] Q. Zhang, D. G. Streets, G. R. Carmichael, *et al.*, "Asian emissions in 2006 for the nasa intex-b mission", *Atmospheric Chemistry and Physics*, vol. 9, no. 14, pp. 5131–5153, 2009.

[58] J. Ding, R. J. Van Der A, B. Mijling, and P. F. Levelt, "Space-based no x emission estimates over remote regions improved in decso", *Atmospheric Measurement Techniques*, vol. 10, no. 3, pp. 925–938, 2017.

[59] J. Ding, R. van der A, B. Mijling, P. Levelt, and N. Hao, "No x emission estimates during the 2014 youth olympic games in nanjing", *Atmospheric Chemistry and Physics*, vol. 15, no. 16, pp. 9399–9412, 2015.

[60] N. Berkhout, "Determining emissions from NO_2 acquired from sentinel 5p's tropomi", M.S. thesis, University of Twente, Enschede, The Netherlands, Jun. 2020.

[61] ECMWF, *Era5: Compute pressure and geopotential on model levels, geopotential height and geometric height*, Accessed: 06-12-2022, 2022. [Online]. Available: https://confluence.ecmwf.int/display/CKB/ERA5%5C%3A+compute+pressure+and+geopotential+on+model+levels%5C%2C+geopotential+height+and+geometric+height.

[62] Lead Centre on Verification of Ensemble Prediction System, *Timesequence of score of the ensemle mean forecast*, Accessed: 17-10-2022, 2022. [Online]. Available: http://epsv.kishou.go.jp/EPSv/html/all/ts_accerrspd.html.

[63] ECMWF, "Part iii dynamics and numerical procedures", in *IFS Documentation CY47R3*. Reading,UK: ECMWF, 2021, pp. 1–31.

[64] Copernicus Climate Change Service, *Era5 hourly data on pressure levels from 1959 to present*, Accessed: 06-12-2022, 2022. [Online]. Available: https://cds.climate.copernicus.eu/cdsapp#!/dataset/reanalysis-era5-pressure-levels?tab=eqc.

[65] H. Hersbach, B. Bell, P. Berrisford, *et al.*, "The era5 global reanalysis", *Quarterly Journal of the Royal Meteorological Society*, vol. 146, no. 730, pp. 1999–2049, 2020.

[66] D. G. Andrews, *An Introduction to Atmospheric Physics*. Cambridge, UK: Cambridge University Press, 2000.

[67] C. Vuik, F. Vermolen, M. van Gijzen, and M. Vuik, *Numerical Methods for Ordinary Differential Equations*. Delft, The Netherlands: Delft Academic Press, 2015.

[68] J. H. Seinfeld, "Urban air pollution: State of the science", *Science*, vol. 243, no. 4892, pp. 745–752, 1989.

[69] S. Beirle, K. F. Boersma, U. Platt, M. G. Lawrence, and T. Wagner, "Megacity emissions and lifetimes of nitrogen oxides probed from space", *Science*, vol. 333, no. 6050, pp. 1737–1739, 2011.

[70] M. W. Shepard and K. Cady-Pereira, *Cris NH_3 data usage statement*, Accessed: 06-12-2022, 2021. [Online]. Available: https://hpfx.collab.science.gc.ca/~mas001/satellite_ext/cris/snpp/nh3/v1_5/CrIS_NH3_data_usage_statement.pdf.

[71] A. A. Nair and F. Yu, "Quantification of atmospheric ammonia concentrations: A review of its measurement and modeling", *Atmosphere*, vol. 11, no. 10, p. 1092, 2020.

[72] K. Sims, *Fluid flow tutorial*, (Accessed: 19-10-2022), 2018. [Online]. Available: https://www.karlsims.com/fluid-flow.html.

[73] R. A. Adams, *Calculus: A complete course*. Toronto, Canada: Pearson Addison Wesley, 2006.

[74] J. Douros, H. Eskes, J. van Geffen, *et al.*, “Comparing sentinel-5p tropomi NO_2 column observations with the cams-regional air quality ensemble”, in *EGU General Assembley*, Vienna, Austria, 2022, pp. 1–40.

[75] H. Theil, “A rank-invariant method of linear and polynomial regression analysis”, *Indagationes mathematicae*, vol. 12, no. 85, p. 173, 1950.

[76] P. K. Sen, “Estimates of the regression coefficient based on kendall’s tau”, *Journal of the American statistical association*, vol. 63, no. 324, pp. 1379–1389, 1968.

[77] W. C. Navidi, *Principles of statistics for engineers and scientists*. New York, USA: McGraw-Hill, 2010.

A

Maps of Results

A.1. Baseline Method - Averaging Time

The averaging time for the baseline Flux-Divergence method and all implemented extensions to the method is set at three months. This section shows the effect of varying this averaging time. As can be expected, taking a longer averaging time filters out a large part of the noise. However, the method scales linearly with time. Running the model for the chosen research area for three months takes approximately 20-30 minutes.

Figure A.1 shows the effect of three different averaging times, on a resolution of 5x5 km. The first image depicts an averaging time of one (particularly sunny) day. Although the weather conditions are favorable, there are still some significant spatial gaps in the data. The data is very noisy, notably above the North Sea to the West of Denmark. Some hot spots do already light up, such as Paris, Hamburg and the Ruhr Area. It should be noted that most days will only contain a fraction of the data available in this image.

The middle image shows the effect of using a week as averaging time. The gaps in the data have almost disappeared, but the data is still very noisy. After averaging over a month of data (Figure A.1c), all gaps in the data have gone, and the noise has also greatly diminished. However, three months is still preferable, as it makes the distinction between noise and small-scale sources more clear.

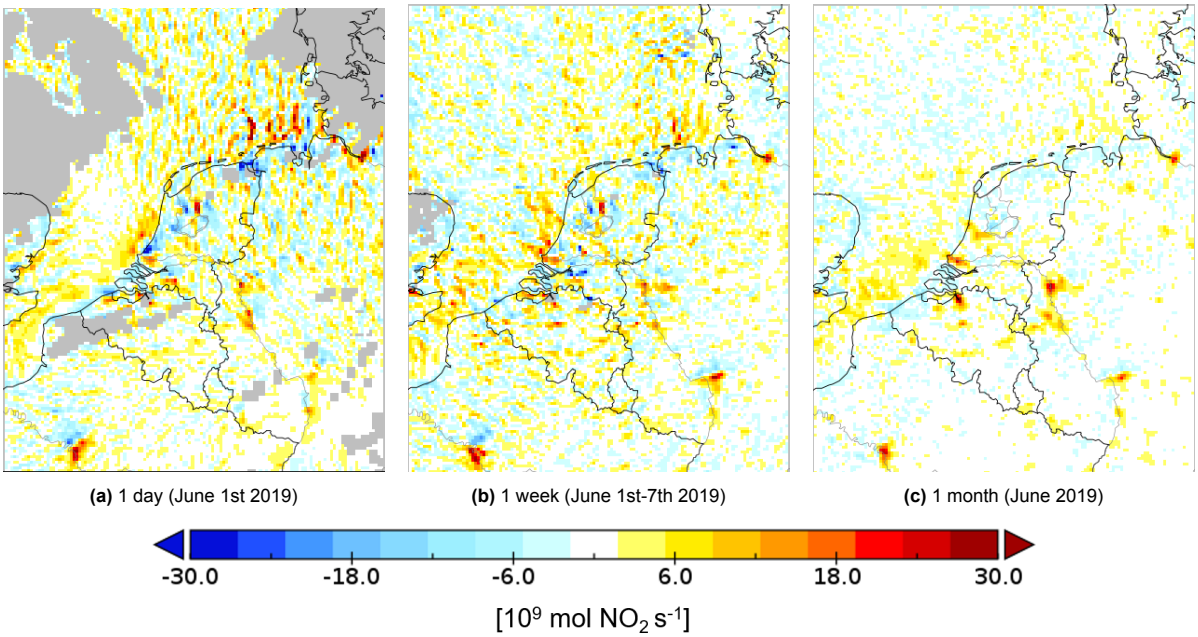

(a) 1 day (June 1st 2019) **(b)** 1 week (June 1st-7th 2019) **(c)** 1 month (June 2019)

Figure A.1: The flux-divergence map of the baseline model, using three different averaging times. The model is run on a resolution of 5x5 km.

A.2. Finite Difference method

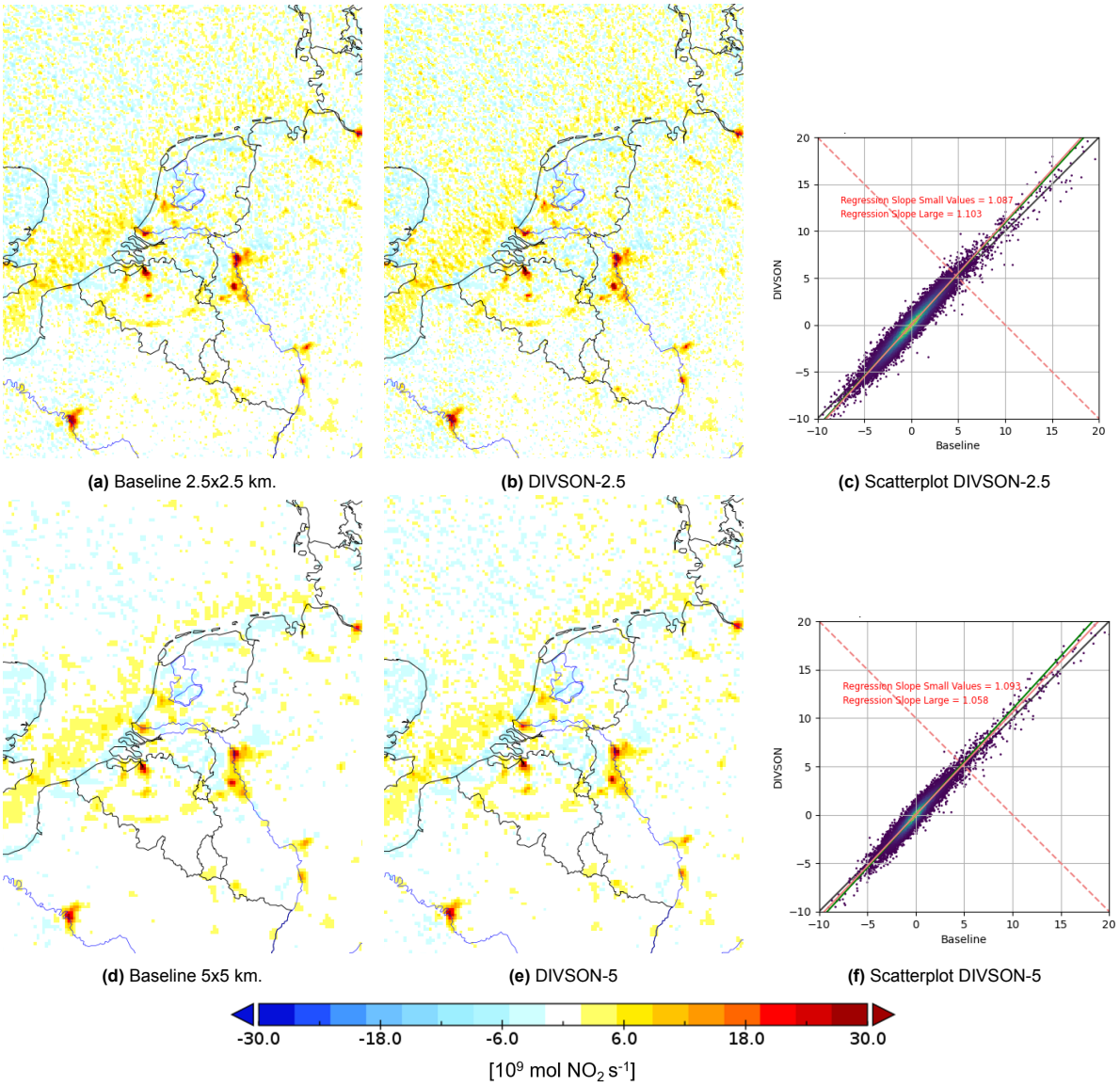

(a) Baseline 2.5x2.5 km. **(b)** DIVSON-2.5 **(c)** Scatterplot DIVSON-2.5

(d) Baseline 5x5 km. **(e)** DIVSON-5 **(f)** Scatterplot DIVSON-5

Figure A.2: Results when using only the nearest neighbours for second order finite difference on a 5x5 km resolution (DIVSON-5).

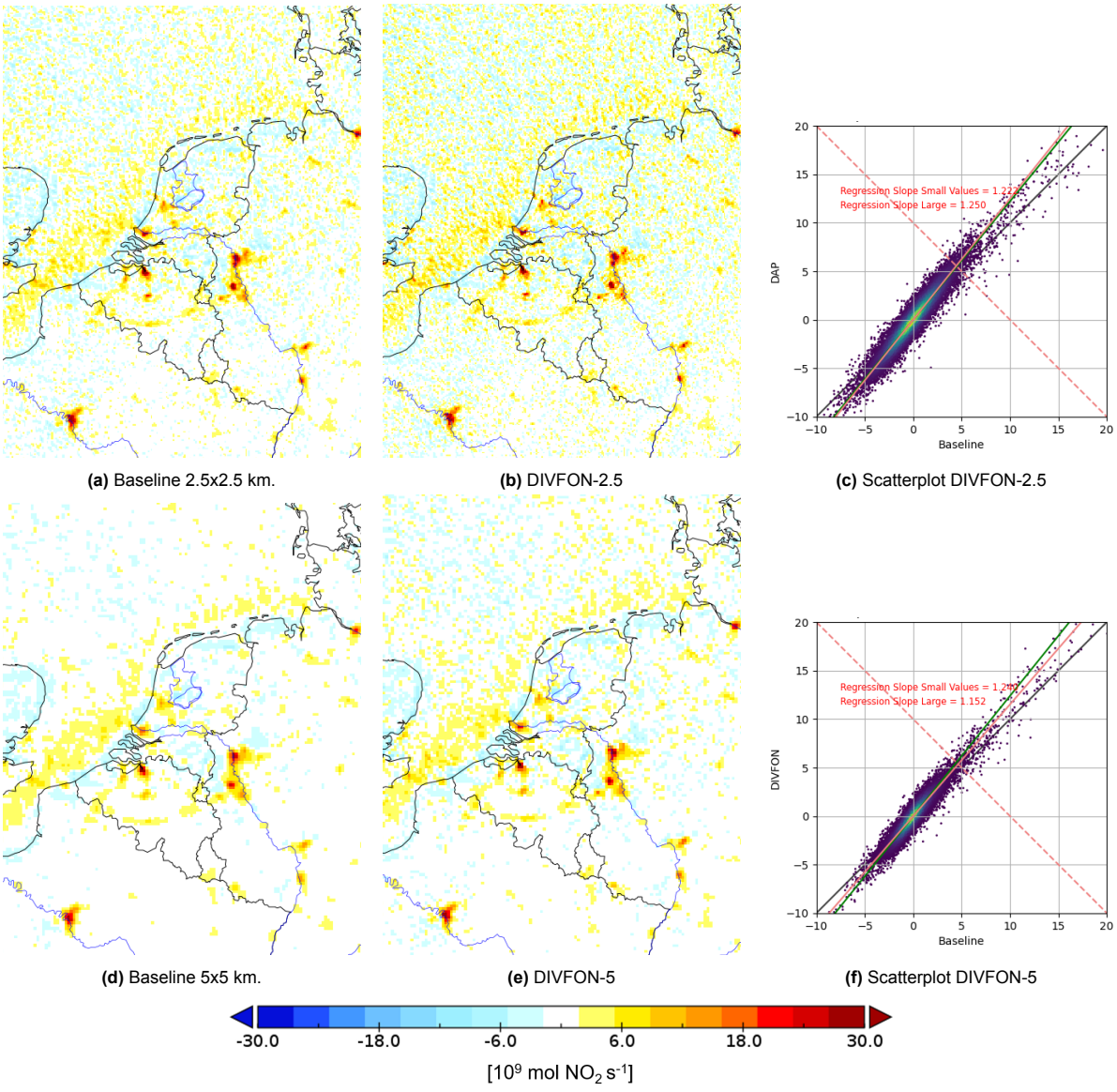

(a) Baseline 2.5x2.5 km. **(b)** DIVFON-2.5 **(c)** Scatterplot DIVFON-2.5

(d) Baseline 5x5 km. **(e)** DIVFON-5 **(f)** Scatterplot DIVFON-5

Figure A.3: Results when using a fourth order finite difference method on a 5x5 km resolution (DIVFON-5).

A.3. WINDDIV

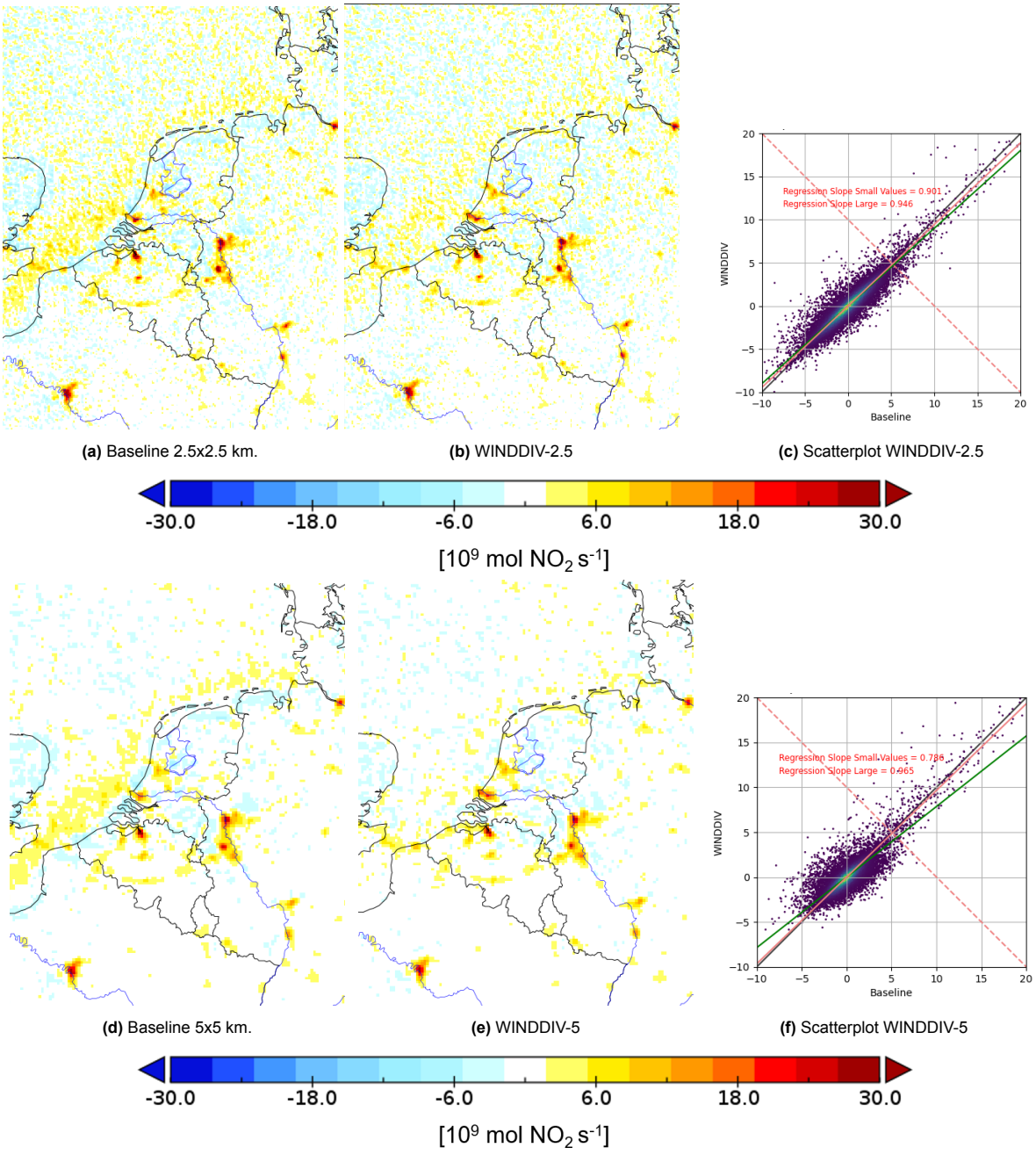

(a) Baseline 2.5x2.5 km. **(b)** WINDDIV-2.5 **(c)** Scatterplot WINDDIV-2.5

(d) Baseline 5x5 km. **(e)** WINDDIV-5 **(f)** Scatterplot WINDDIV-5

Figure A.4: Results when using the wind data set after diminishing its divergence, on a 2.5x2.5 km resolution (WINDDIV-2.5).

A.4. WINDMEAN

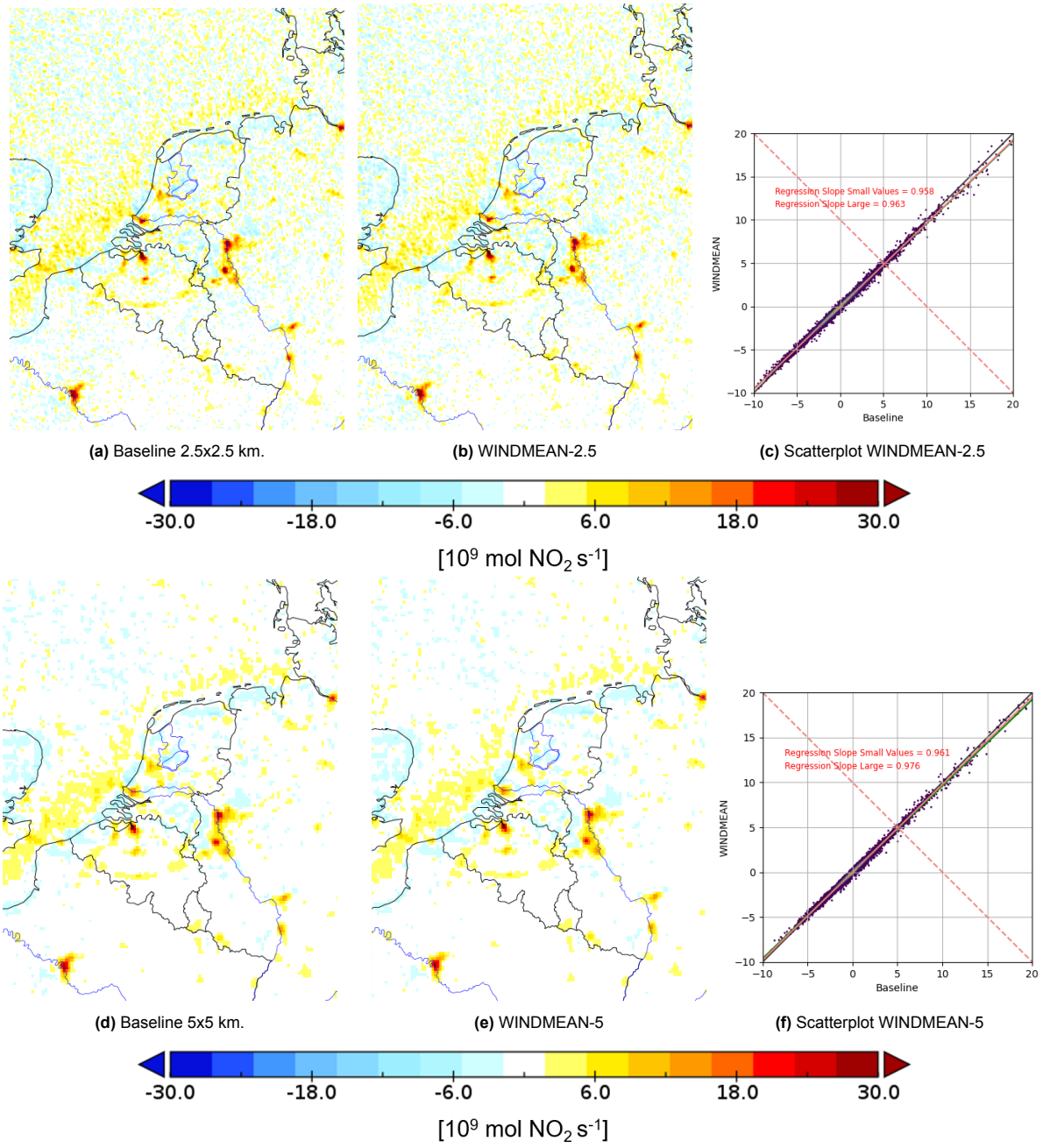

(a) Baseline 2.5x2.5 km. **(b)** WINDMEAN-2.5 **(c)** Scatterplot WINDMEAN-2.5

(d) Baseline 5x5 km. **(e)** WINDMEAN-5 **(f)** Scatterplot WINDMEAN-5

Figure A.5: Results when using the averaged wind over the PBL, instead of the half-way wind, on a 2.5x2.5 km resolution (WINDMEAN-2.5).

A.5. SAVG

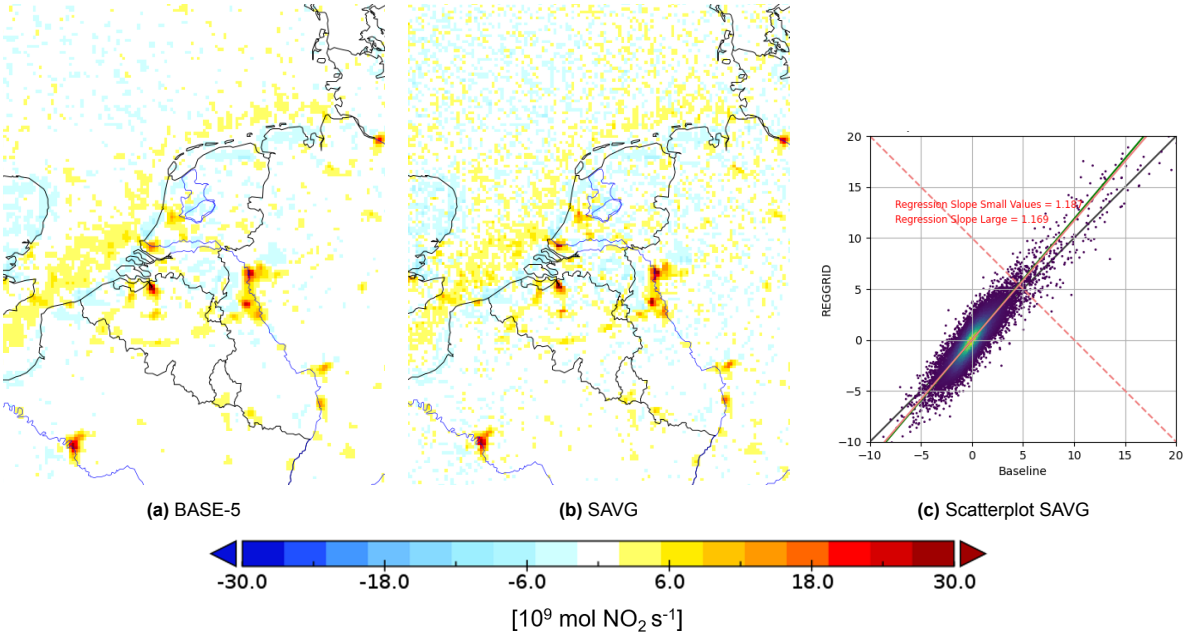

(a) BASE-5 **(b)** SAVG **(c)** Scatterplot SAVG

Figure A.6: Results when spatially averaging the 2.5x2.5 km resolution baseline dataset to a 5x5 km resolution (SAVG).

A.6. TROPOMI Grid

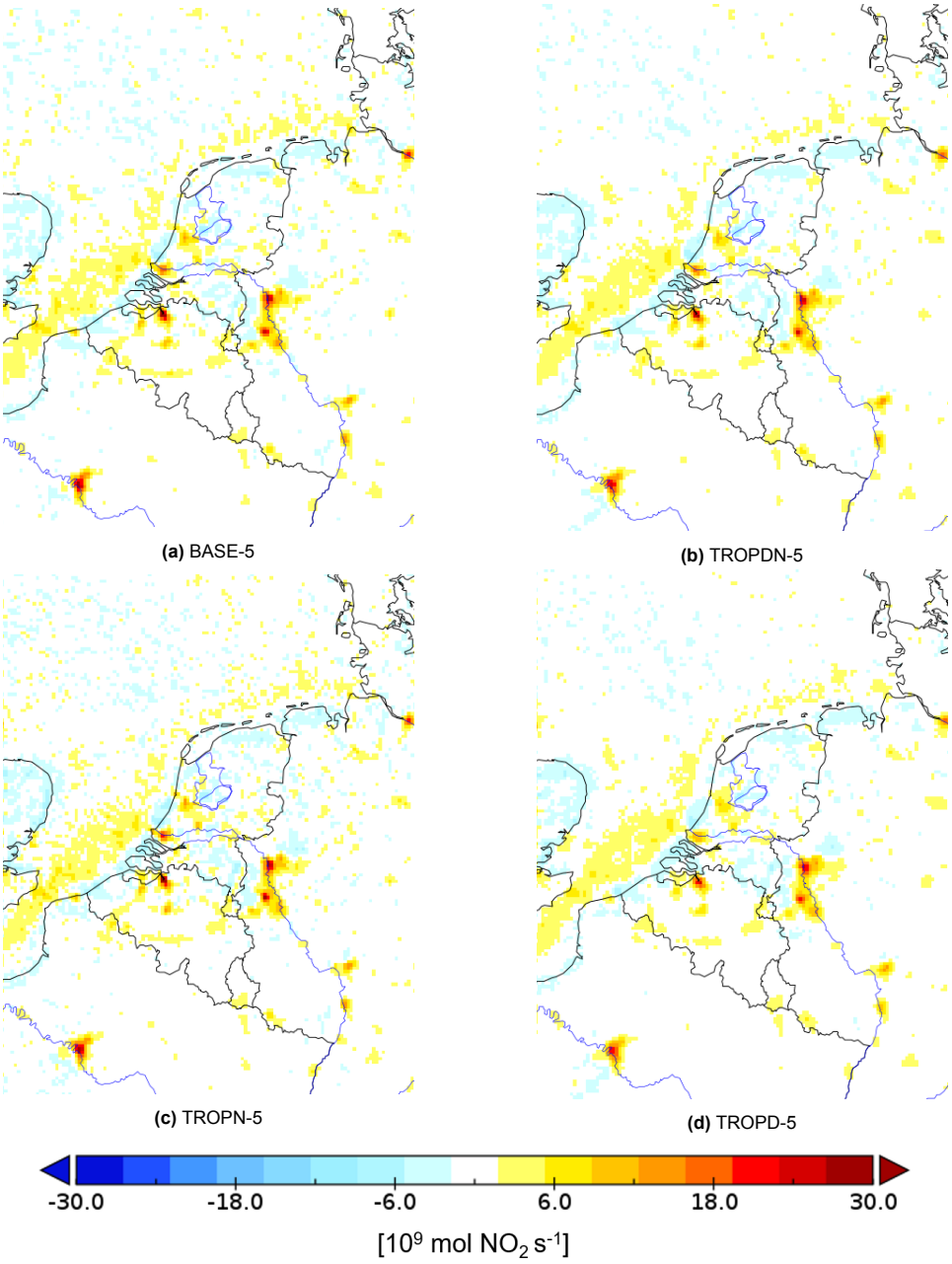

Figure A.7: Results using divergence computed on the TROPOMI grid on a 5x5 km grid. The baseline scenario, where the divergence is computed on the regular latitude-longitude grid, is included for comparison in (a).

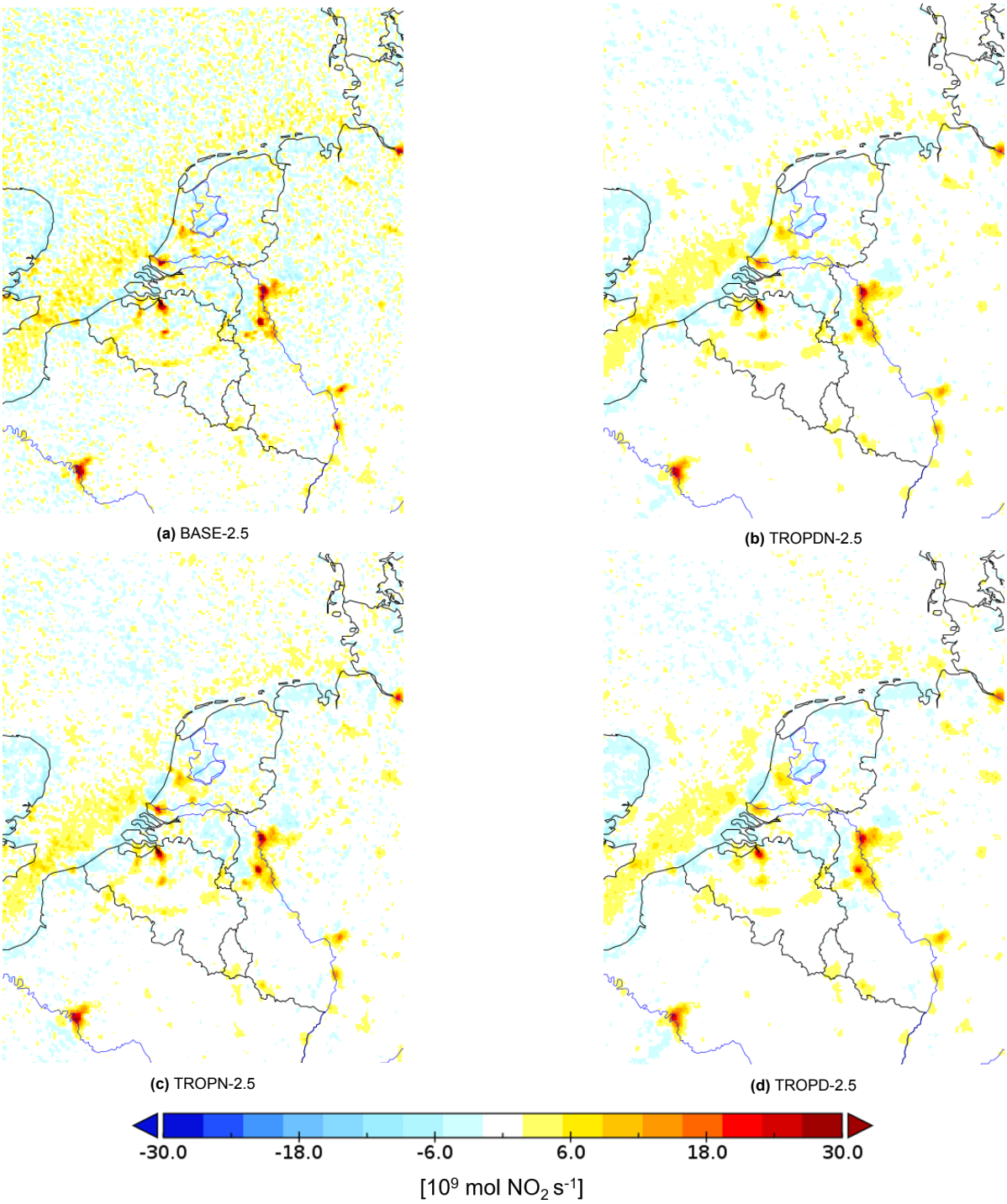

(a) BASE-2.5

(b) TROPDN-2.5

(c) TROPN-2.5

(d) TROPD-2.5

Figure A.8: Results using divergence computed on the TROPOMI grid on a 2.5x2.5 km grid. The baseline scenario, where the divergence is computed on the regular latitude-longitude grid, is included for comparison in (a).

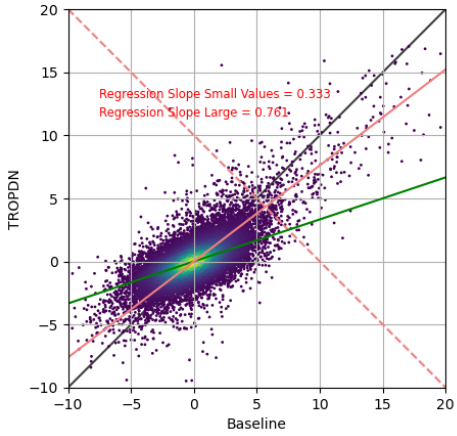

(a) Nearest and diagonal flux-divergence.

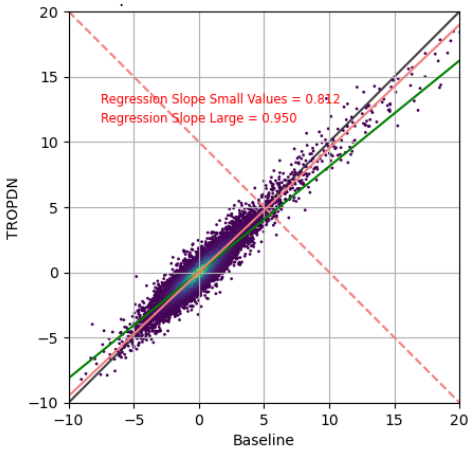

(b) Nearest flux-divergence.

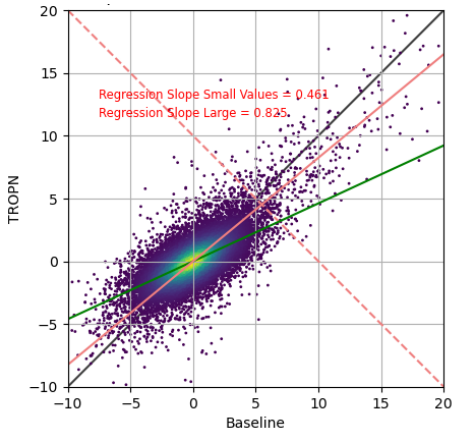

(c) Diagonal flux-divergence.

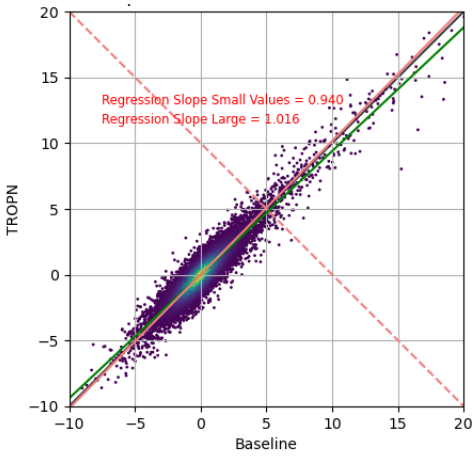

(d) Nearest and diagonal flux-divergence.

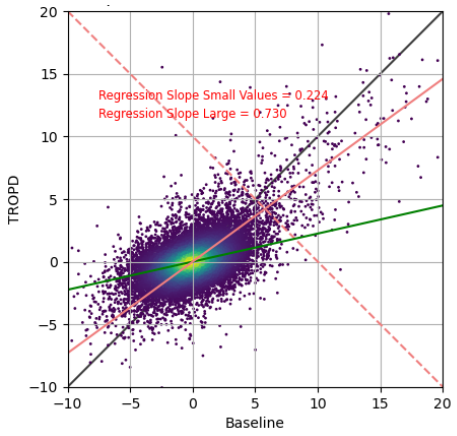

(e) Nearest flux-divergence.

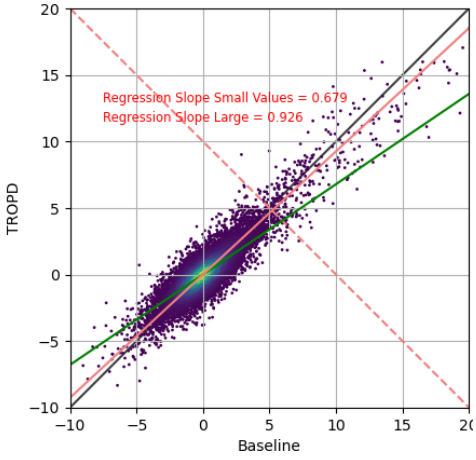

(f) Diagonal flux-divergence.

Figure A.9: Scatterplots comparing baseline values and values where the TROPOMI grid was used to compute divergence, on a gridding resolution of 5x5 km.

A.7. DAP

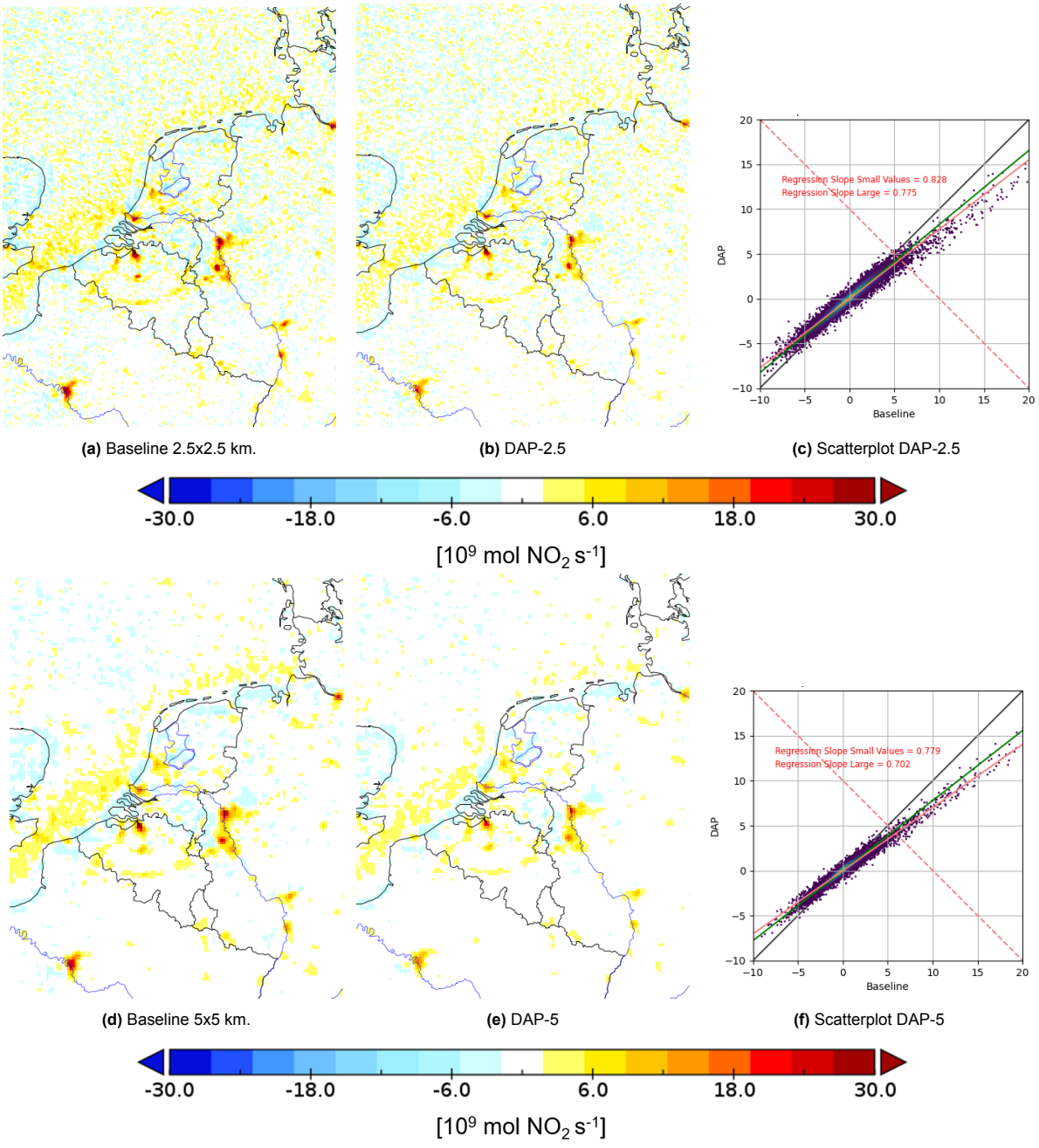

(a) Baseline 2.5x2.5 km. **(b)** DAP-2.5 **(c)** Scatterplot DAP-2.5

(d) Baseline 5x5 km. **(e)** DAP-5 **(f)** Scatterplot DAP-5

Figure A.10: Results when using the default retrieval a-priori instead of the CAMS a-priori (DAP-5).

A.8. Emissions

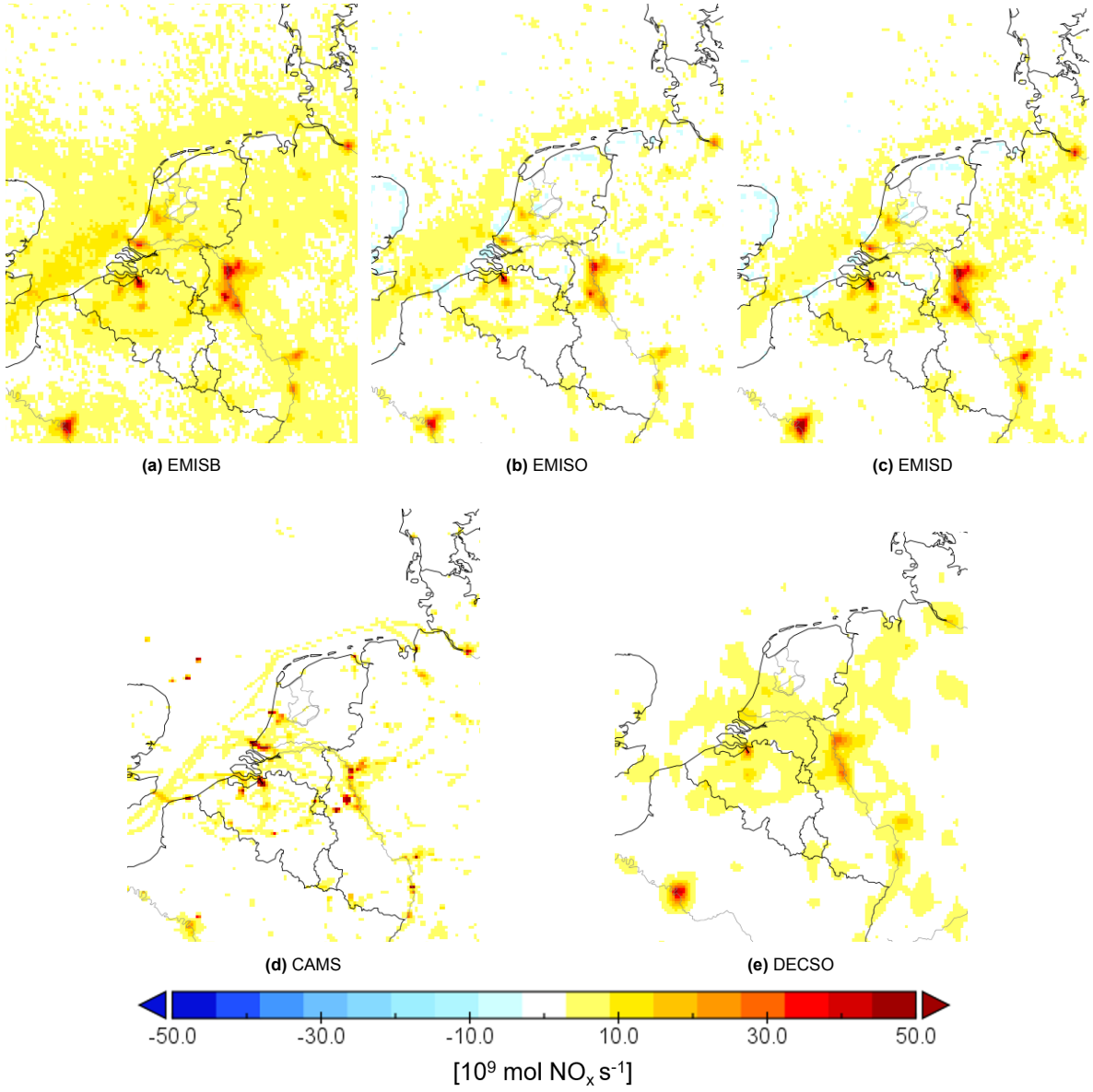

Figure A.11: Results of emission experiments on a resolution of 5x5 km.

A.9. Ammonia - NH3TIMEx

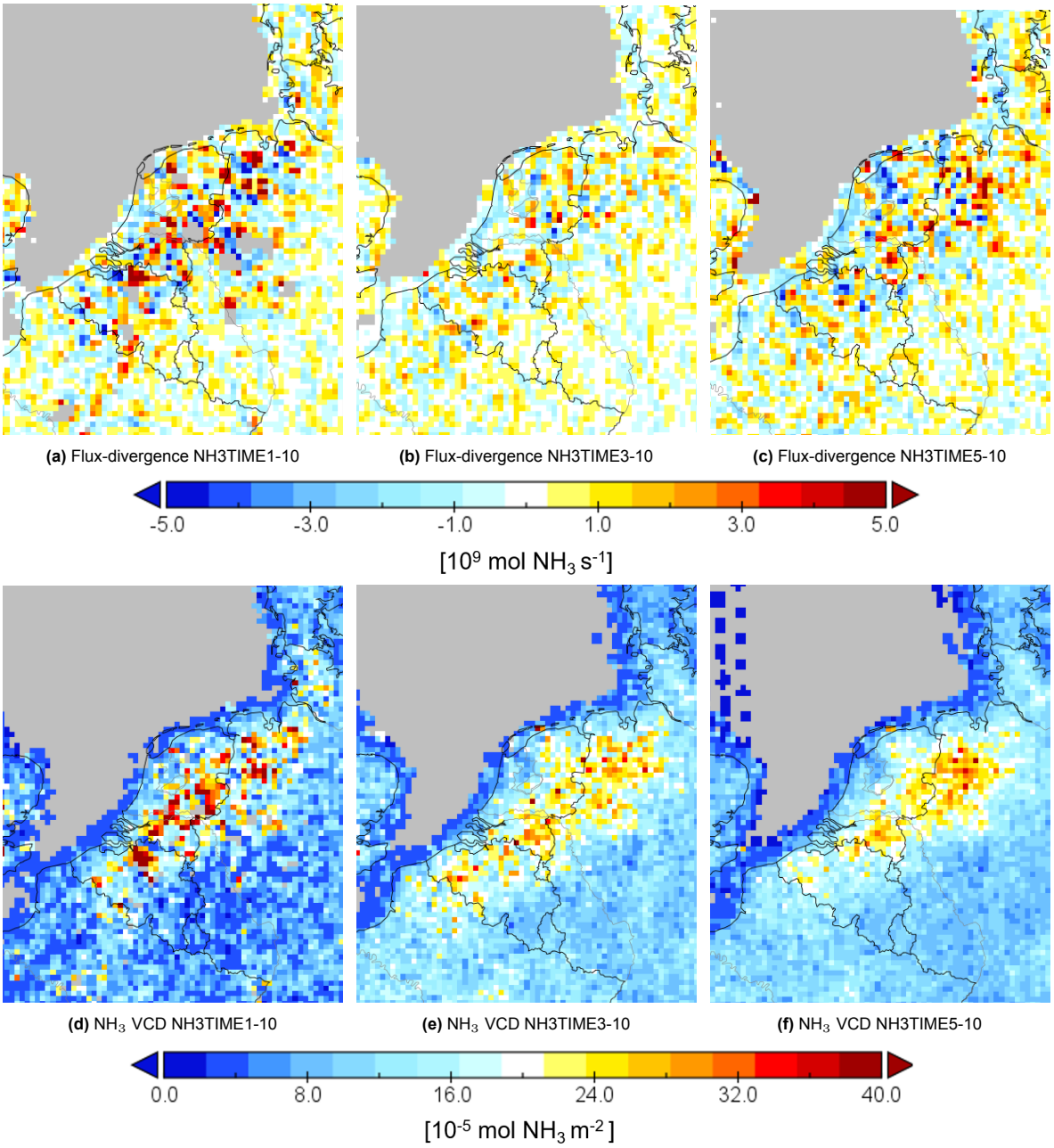

(a) Flux-divergence NH3TIME1-10 **(b)** Flux-divergence NH3TIME3-10 **(c)** Flux-divergence NH3TIME5-10

(d) NH_3 VCD NH3TIME1-10 **(e)** NH_3 VCD NH3TIME3-10 **(f)** NH_3 VCD NH3TIME5-10

Figure A.12: Results of NH3TIME experiments, on a 10x10 km resolution.

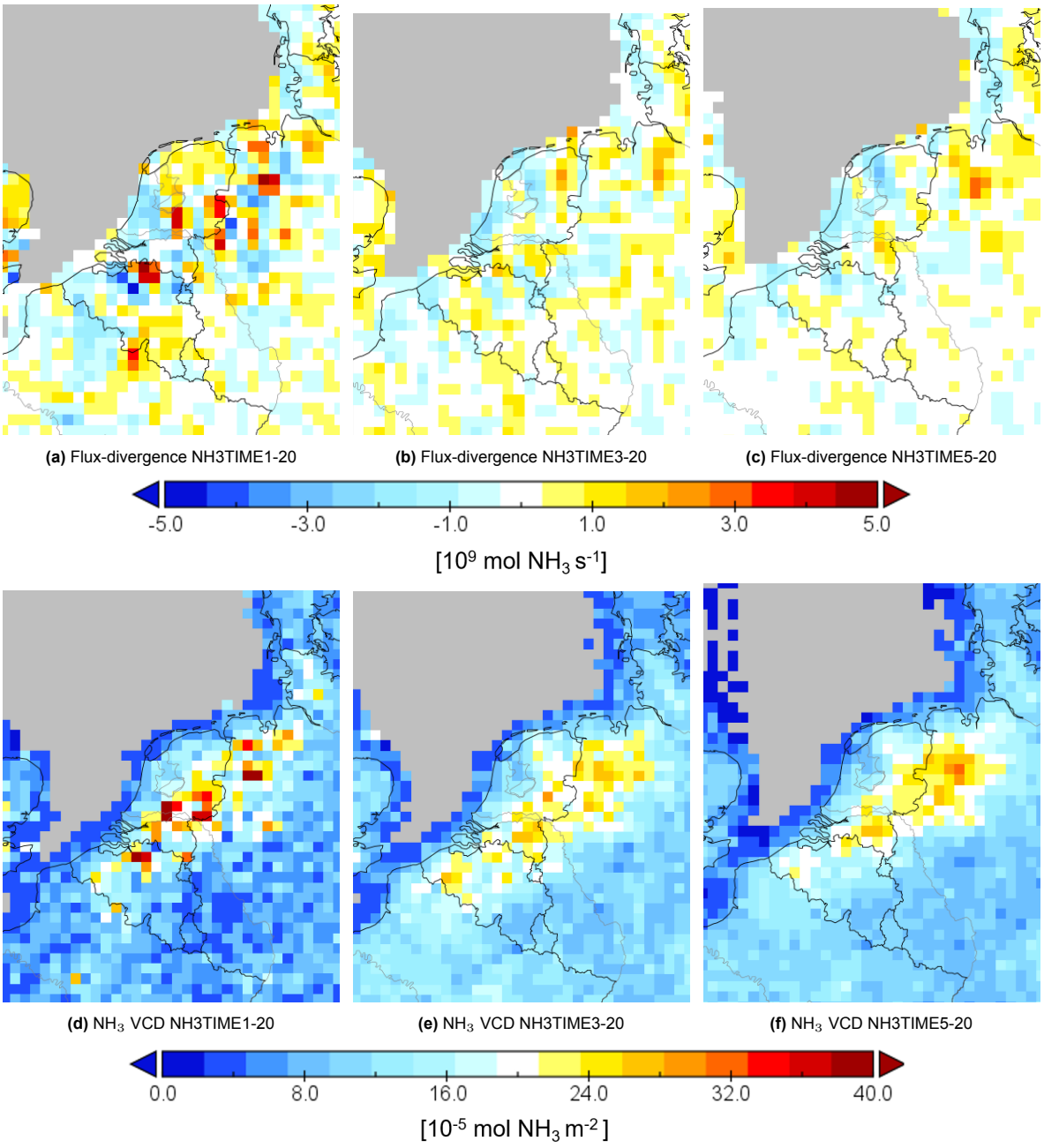

Figure A.13: Results of NH3TIME experiments, on a 20x20 km resolution.

A.10. Ammonia - NH3MONTHAVG

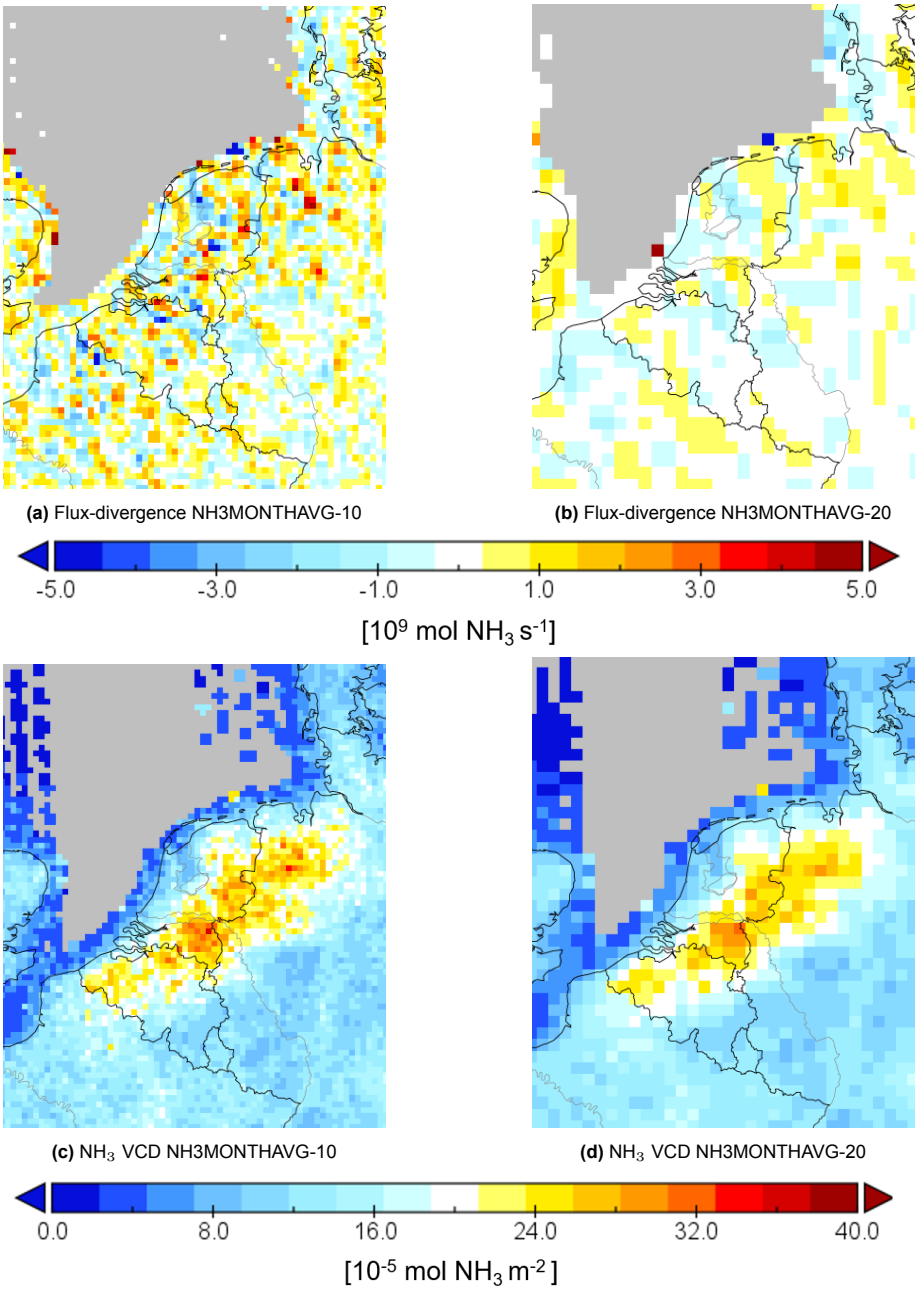

Figure A.14: Results of NH3MONTHAVG experiments.

A.11. Ammonia - NH3YEARAVG

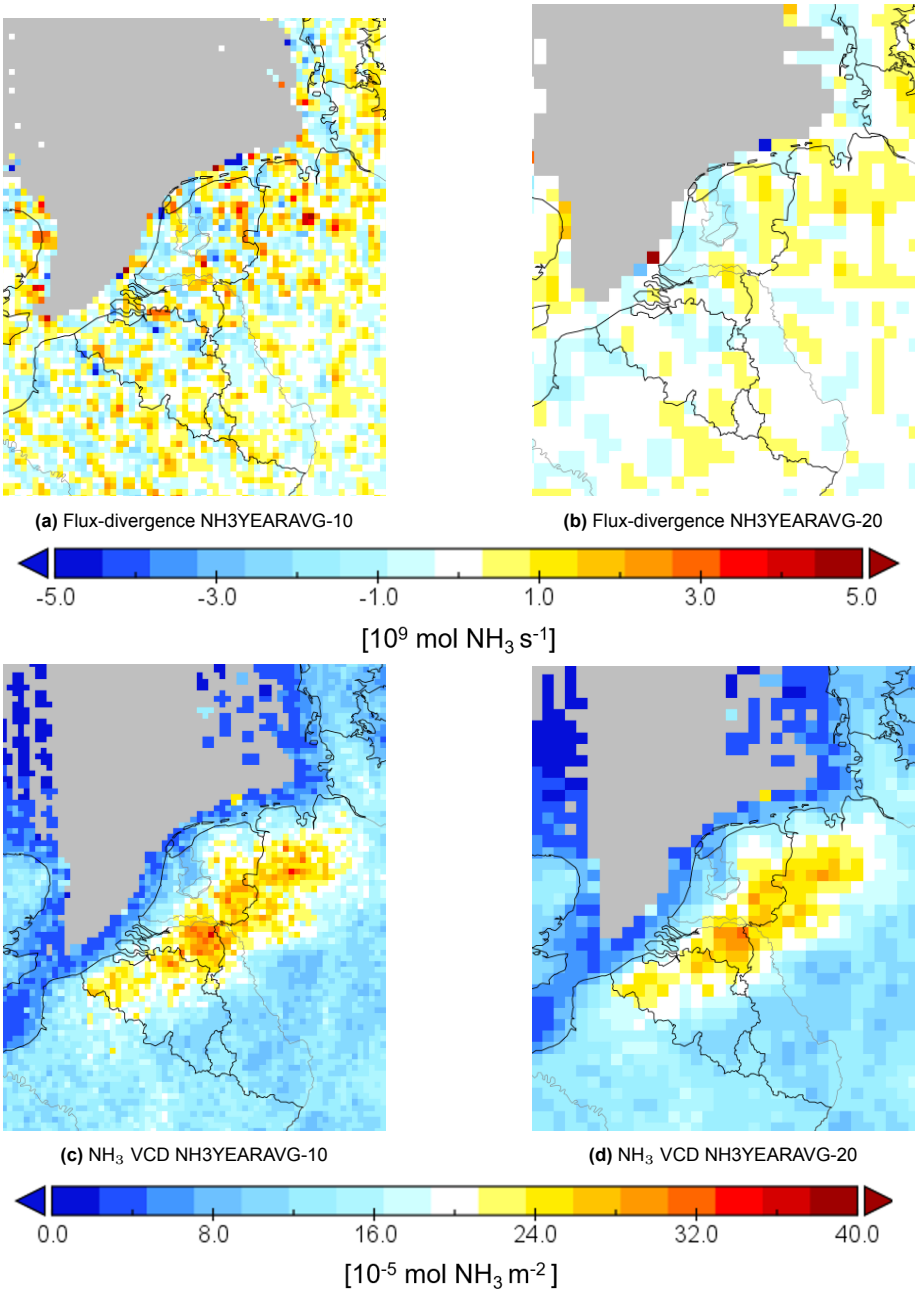

(a) Flux-divergence NH3YEARAVG-10 **(b)** Flux-divergence NH3YEARAVG-20

(c) NH_3 VCD NH3YEARAVG-10 **(d)** NH_3 VCD NH3YEARAVG-20

Figure A.15: Results of NH3YEARAVG experiments.

B

Tables

Projection 1	**Projection 2**	τ	σ	ρ
Original Quadrant: 1, Diagonal Quadrant: 1				
$P_{pUpV} = \|\mathbf{u}\| \cdot \cos\alpha$	$P_{mUpV} = \|\mathbf{u}\| \cdot \cos\beta$	$\arctan(\frac{P_V(\mathbf{u})}{P_U(\mathbf{u})})$	$\arctan(\frac{pV}{pU})$	$\arctan(\frac{pV}{mU})$
Original Quadrant: 2, Diagonal Quadrant: 1				
$P_{pUpV} = \|\mathbf{u}\| \cdot \cos\beta$	$P_{mUpV} = \|\mathbf{u}\| \cdot \cos\alpha$	$\arctan(\frac{P_V(\mathbf{u})}{P_U(\mathbf{u})})$	$\arctan(\frac{pV}{mU})$	$\arctan(\frac{pV}{pU})$
Original Quadrant: 2, Diagonal Quadrant: 2				
$P_{mUmV} = -\|\mathbf{u}\| \cdot \cos\beta$	$P_{mUpV} = \|\mathbf{u}\| \cdot \cos\alpha$	$\arctan(\frac{P_U(\mathbf{u})}{P_V(\mathbf{u})})$	$\arctan(\frac{mU}{pV})$	$\arctan(\frac{mU}{mV})$
Original Quadrant: 3, Diagonal Quadrant: 2				
$P_{mUmV} = -\|\mathbf{u}\| \cdot \cos\alpha$	$P_{mUpV} = \|\mathbf{u}\| \cdot \cos\beta$	$\arctan(\frac{P_U(\mathbf{u})}{P_V(\mathbf{u})})$	$\arctan(\frac{mU}{mV})$	$\arctan(\frac{mU}{pV})$
Original Quadrant: 3, Diagonal Quadrant: 3				
$P_{mUmV} = -\|\mathbf{u}\| \cdot \cos\alpha$	$P_{pUmV} = -\|\mathbf{u}\| \cdot \cos\beta$	$\arctan(\frac{P_V(\mathbf{u})}{P_U(\mathbf{u})})$	$\arctan(\frac{mV}{mU})$	$\arctan(\frac{mV}{pU})$
Original Quadrant: 4, Diagonal Quadrant: 3				
$P_{mUmV} = -\|\mathbf{u}\| \cdot \cos\beta$	$P_{pUmV} = -\|\mathbf{u}\| \cdot \cos\alpha$	$\arctan(\frac{P_V(\mathbf{u})}{P_U(\mathbf{u})})$	$\arctan(\frac{mV}{pU})$	$\arctan(\frac{mV}{mU})$
Original Quadrant: 4, Diagonal Quadrant: 4				
$P_{pUpV} = \|\mathbf{u}\| \cdot \cos\beta$	$P_{pUmV} = -\|\mathbf{u}\| \cdot \cos\alpha$	$\arctan(\frac{P_U(\mathbf{u})}{P_V(\mathbf{u})})$	$\arctan(\frac{pU}{mV})$	$\arctan(\frac{pU}{pV})$
Original Quadrant: 1, Diagonal Quadrant: 4				
$P_{pUpV} = \|\mathbf{u}\| \cdot \cos\alpha$	$P_{pUmV} = -\|\mathbf{u}\| \cdot \cos\beta$	$\arctan(\frac{P_U(\mathbf{u})}{P_V(\mathbf{u})})$	$\arctan(\frac{pU}{pV})$	$\arctan(\frac{pU}{mV})$

Table B.1: Overview of the formulas needed to compute the diagonal wind projections in order to use TROPOMI grid cells to compute divergence. This is an addition to the computations described in Section 3.6

.

C

Used Notation and Abbreviations

Used Notation	Meaning
$h\nu$	Photon energy
N_s	Slant column density (also SCD)
N_s^{trop}	Tropospheric slant column density
N_s^{strat}	Stratospheric slant column density
N_v	Vertical column density
N_v^{trop}	Tropospheric vertical column density
N_v^{strat}	Stratospheric vertical column density
M	Air mass factor
M^{trop}	Tropospheric air mass factor (or VCD)
M^{strat}	Stratospheric air mass factor
A	Averaging kernel
$\mathbf{x}$	True vertical column density
$\hat{\mathbf{x}}$	Measured vertical column density
$Q_{c,2}(h)$	Formula for second order central finite difference
$Q_{c,4}(h)$	Formula for fourth order central finite difference
$R_{c,2}(h)$	Truncation error for second order central finite difference
$R_{c,4}(h)$	Truncation error for fourth order central finite difference
$S_{c,2}(h)$	Measurement and rounding error for second order central finite difference
$S_{c,4}(h)$	Measurement and rounding error for fourth order central finite difference
$E_{c,2}(h)$	Total error for second order central finite difference
$E_{c,4}(h)$	Total error for fourth order central finite difference
C^3	Set of three times continuously differentiable continuous functions
R	Set of real numbers
$\mathcal{O}$	Order of magnitude
P	An atmospheric trace gas
$\mathbf{f}$	The 2-dimensional flux of P
V_P	Vertical column density of trace gas P
$\mathbf{w}$	2-dimensional flow of the wind
f^x/w^x	Component of **f**/**w** in x-direction
u	East-West direction
v	North-South direction
U	Across-track direction
V	Along-track direction
$pUpV$	$U+V$ direction
$pUmV$	$U-V$ direction
$mUpV$	$V-U$ direction
$mUmV$	$-U-V$ direction
E	Emissions/sources of P
S	Sinks/loss term of P
Δx/Δy	Distance between pixels regular grid
Δxr/Δxl/Δy/Δdr/Δdl	Distance between pixels TROPOMI grid
lon_{min}/lon_{max}	Minimal and maximal longitude of research area
lat_{min}/lat_{max}	Minimal and maximal latitude of research area
d_lon	Grid size in longitudinal direction
d_lat	Grid size in latitudinal direction
n_lon	Number of grid cells in longitudinal direction
n_lat	Number of grid cells in latitudinal direction
∇	The divergence term
$\nabla_{2,c}$	Divergence computed using second order central divergence (Both diagonal and nearest neighbors)
$\nabla_{4,c}$	Divergence computed using fourth order central divergence
$\nabla_{2,n}$	Divergence computed using second order central divergence (nearest neighbors only)
$\nabla_{2,d}$	Divergence computed using second order central divergence (diagonal neighbors only)
m	Mixing ratio NO_x/NO_2
τ	Lifetime

Table C.1: Used notation in this thesis.

Used Abbreviation	Meaning
BASE	See Table 3.2
CAMS	Copernicus Atmosphere Monitoring Service
CAMS-REG	Copernicus Atmosphere Modelling Service REGional inventory
CrIS	Cross-track Infrared Sounder
DAP	See Table 3.2
DECSO	Daily Emissions estimations Constrained by Satellite Observations
DIVSON/DIVFON	See Table 3.2
DOFS	Degrees of Freedom
EMISO/EMISB/EMISD	See Table 3.3
ECMWF	European Centre for Medium-Range Weather Forecasts
EOS	Earth Observing System
ERA5	ECMWF Reanalysis v5
ERS	European Remote-sensing Satellite
ESA	European Space Agency
EU	European Union
GAINS	Greenhouse gas Air pollution Interaction and Synergies model
GOME	Global Ozone Monitoring Experiment
IASI	Infrared Atmospheric Sounder Interferometer
INTEX-B	Intercontinental Chemical Transport Experiment-B
IR	Infrared
JPSS	Joint Polar Satellite System
KDW	Kritische Depositiewaarde *Critical Deposition Values*
KNMI	Koninklijk Nederlands Meteorologisch Instituut *Royal Netherlands Meteorological Institute*
METOP	Meteorological Operational satellite
NASA	National Aeronautics and Space Administration
NECA	Nitrogen Emission Control Area
NH3TIME	See Table 3.4
NH3MONTHAVG	See Table 3.4
NH3YEARAVG	See Table 3.4
NIR	Near Infrared
NOAA	National Oceanic and Atmospheric Administration
NPP	National Polar-orbiting Partnership
OMI	Ozone Monitoring Instrument
PAS	Programmatische Aanpak Stikstof *Programmatic Approach Nitrogen*
PBL	Planetary Boundary Layer
PCC	Pearson's Correlation Coefficient
RIVM	Rijksinstituut voor Volksgezondheid en Milieu *National Institute for Public Health and the Environment*
RSS	Regression Slope for Small flux-divergence values
RSL	Regression Slope for Large flux-divergence values
SAA	South Atlantic Anomaly
SAVG	See Table 3.2
SCD	Slant Column Density
SCIAMACHY	SCanning Imaging Absorption spectroMeter for Atmospheric CHartographY
SDN	Standard Deviation for Low-emission region
STEAM	Ship Traffic Emissions Assessment Model
SWIR	Short-wave Infrared
SZA	Solar Zenith Angle
S5P	Sentinel 5-Precursor
TE	Total Emission
TES	Tropospheric Emission Spectrometer
TROPDN/TROPN/TROPD	See Table 3.2

TROPOMI	Tropospheric Monitoring Instrument
UV	Ultravoilet
VCD	Vertical column Density
VIS	Visible Spectrum
WINDDIV/WINDMEAN	See Table 3.2
WMO	World Meteorological Organization

Table C.2: Used abbreviations in this thesis.